



HAL
open science

Inelastic x-ray scattering from polycrystalline materials.

Irmengard Fischer

► **To cite this version:**

Irmengard Fischer. Inelastic x-ray scattering from polycrystalline materials.. Condensed Matter [cond-mat]. Université Joseph-Fourier - Grenoble I, 2008. English. NNT: . tel-00349859

HAL Id: tel-00349859

<https://theses.hal.science/tel-00349859v1>

Submitted on 5 Jan 2009

HAL is a multi-disciplinary open access archive for the deposit and dissemination of scientific research documents, whether they are published or not. The documents may come from teaching and research institutions in France or abroad, or from public or private research centers.

L'archive ouverte pluridisciplinaire **HAL**, est destinée au dépôt et à la diffusion de documents scientifiques de niveau recherche, publiés ou non, émanant des établissements d'enseignement et de recherche français ou étrangers, des laboratoires publics ou privés.

Université de Grenoble I
SCIENCES, TECHNOLOGIE, MÉDECINE

THÈSE

présentée à l'Université Joseph Fourier - Grenoble I

Pour le titre de
Docteur de l'UNIVERSITÉ GRENOBLE I

Doctorat: Physique de la Matière Condensée et du Rayonnement
Ecole Doctorale: Physique

Inelastic x - ray scattering from polycrystalline materials

par

Irmengard FISCHER

soutenue le 30 septembre devant le jury composé de:

J.R. REGNARD

G. BENEDEK, R. CURRAT, I. LOA

D. A. KEEN

M. KRISCH, A. BOSAK

Président du Jury

Rapporteurs

Examineur

Directeurs de thèse

Thèse préparée au sein du laboratoire:
European Synchrotron Radiation Facility (ESRF), Grenoble

Inelastic x - ray scattering from polycrystalline materials

Sicher ist, dass nichts sicher ist. Selbst das nicht.

Joachim Ringelnatz

Contents

Introduction	5
Introduction (franaise)	9
1 Lattice dynamics and elasticity in crystalline materials	15
1.1 Single crystals	15
1.1.1 Inelastic x-ray scattering	15
1.1.2 Elasticity theory	22
1.2 Polycrystalline Materials	26
1.2.1 Inelastic x-ray scattering	26
1.2.2 Elasticity theory	34
1.3 Inelastic x - ray scattering and inelastic neutron scattering	36
2 Extraction of lattice dynamics from polycrystalline samples	41
2.1 Powder diffraction	41
2.2 Inelastic x-ray scattering	44
2.2.1 Principal Concepts	44
2.2.2 The Born - von Karman Model	45
2.2.3 IXS intensity from a polycrystalline sample	47
2.2.4 The Fitting procedure	49
3 Experimental techniques	53
3.0.5 The inelastic x - ray spectrometer	53
3.0.6 The diamond anvil cell	57
4 Experimental results	61
4.1 Cubic system	61
4.1.1 Magnesium oxide	62
4.1.2 Experiment	62
4.1.3 Results	62

CONTENTS

4.2	Monoatomic hexagonal system	66
4.2.1	Beryllium	66
4.2.2	Experiment	67
4.2.3	Experimental results	69
4.2.4	Comparison of different lattice dynamic models	84
4.3	Monoatomic hexagonal system with texture	88
4.3.1	Pyrolytic graphite	88
4.3.2	Experimental results	89
4.4	Diatomic tetragonal system	104
4.4.1	Stishovite	104
4.4.2	Experimental results	105
4.4.3	Comparison with theoretical model	107
4.4.4	Single crystal stishovite	110
5	Further developments	113
5.1	Complexity of the studied materials	113
5.2	Stability of the fitting routine	114
5.3	High pressure applications	115
5.3.1	Experiment: Iron under high pressure	115
5.3.2	Texture	115
5.3.3	Scattering Intensity	116
	Conclusion	121
	Conclusion (franaise)	125
	Appendix	129
	Bibliography	133
	Acknowledgements	141

Introduction

Many thermodynamical and elastic properties of a crystal can be understood by investigating the energy of phonons as a function of their momentum throughout the Brillouin zone (BZ). These include equilibrium properties such as thermal expansion, heat capacity and melting, but also transport properties, electron - phonon coupling and the transmission of sound, as well as elastic properties and interatomic forces. The experimental investigation of the phonon dispersion relation, correlating momentum \vec{Q} and energy E of lattice vibrations, has been traditionally the domain of neutron spectroscopy. Neutrons as probing particles are particularly suitable, since the energy of neutrons with wavelengths of the order of inter-particle distances is about 1 meV , and therefore are comparable to typical phonon energies (several meV). Furthermore, the momentum of the neutron allows one to probe the whole dispersion scheme, in contrast to inelastic light scattering techniques such as Brillouin and Raman scattering.

X-rays represent another probe which can in principle as well be used to determine the phonon dispersion throughout the Brillouin zone. However, in several textbooks it has been pointed out that this would represent a formidable experimental challenge, mainly due to the fact that an x-ray instrument would have to provide an extremely high energy resolution of about $\Delta E/E = 10^{-7}$. For example, the following statement can be found in the textbook *Solid State Physics* by Ashcroft and Mermin about the possibility to measure phonons with X-rays: *"In general the resolution of such minute photon frequency shifts is so difficult that one can only measure the total scattered radiation of all frequencies..."* [1]. Indeed, the first attempts for the extraction of lattice dynamics from x-ray experiments were made by analysing the diffuse scattering intensity between the diffraction spots. It was shown by Laval in 1939 [2] that the thermal movements of the atoms contributed to these intensities, which could therefore provide information on the lattice dynamics. One of the first experiments, measuring the diffuse scattering along high symmetry directions, was performed by Olmer (1948) [3] on fcc aluminium. His work was completed by Walker (1956) [4]. Furthermore, in combination with the lattice dynamics theory of Born, interatomic force constants could be derived by Curien [5] and Jacobsen [6] up to the third-nearest neighbour interaction for α -iron and copper, respectively.

Introduction

Another example is the investigation of the diffuse scattering of Benzil by Lonsdale and Smith in 1941 [?]. There was, however, no possibility at that time to measure such dispersion curves directly, due to the lack of scattered intensity. In the 1980's a spectrometer setup, using a rotating anode x-ray generator, yielded an instrumental energy resolution ΔE of 42 meV, but the photon flux was not sufficient to perform an inelastic x-ray scattering (IXS) experiment [7]. The advent of 2nd generation synchrotron radiation sources (parasitic use of high-energy storage rings with wiggler x-ray sources) catalysed the first pioneering IXS experiments. Great efforts were put in the development of the required backscattering monochromators for X-rays, and in 1986 an energy resolution of 11 meV at an energy $E = 13.8$ keV was achieved [8]. The first measurements of a phonon dispersion curve were performed by Dorner *et al.* [9] in summer 1986 on a bending magnet at HASYLAB, Hamburg at the spectrometer INELAX. The longitudinal acoustic and optic phonon branches along the [001] direction for beryllium were recorded with an energy resolution of $\Delta E = 55$ meV. The modest energy resolution and photon flux were significantly improved by further developments on the backscattering monochromator and the installation of the INELAX instrument on a wiggler source at HASYLAB, and an instrumental resolution of 9 meV could be achieved [10]. With the advent of third generation synchrotron radiation sources (dedicated storage rings for synchrotron radiation research with undulator (or wiggler) based x-ray sources) and important improvements in x-ray optics, experiments are nowadays routinely performed with an energy resolution of 1.5 meV. At present, there are worldwide five instruments dedicated to IXS from phonons: ID16 and ID28 at the European Synchrotron Radiation Facility (ESRF) in France, sector 3ID and 30ID at the Advanced Photon Source (APS) in USA, and BL35XU at the Super Photon Ring (SPring-8) in Japan.

Today, the use of photons complements the capabilities of inelastic neutron spectroscopy, in particular in cases where neutron techniques are difficult or impossible to apply. This concerns the study of disordered systems where well-defined sound-like excitations are only clearly visible in the small momentum transfer (Q) limit, typically below 10 nm⁻¹. In particular systems with a high speed of sound ($v_{sound} \sim E/Q$), the required energy transfer (E) and energy resolution can often not be attained simultaneously [11]. These kinematic restrictions are absent for X-rays. Another important advantage of inelastic x-ray scattering experiments lies in the possibility of using small sample volumes ($10^{-7} - 10^{-4}$ mm³), while INS experiments require sample volumes of typically several mm³. This opens up possibilities to study materials only available in very small quantities and/or their investigation in extreme thermodynamic conditions, such as very high pressure.

For both techniques, an appropriate selection of the scattering geometry allows the

determination of the complete phonon dispersion scheme in single crystalline materials. In polycrystalline materials the directional information of the momentum transfer \vec{Q} is lost due to the random orientation of the individual crystalline grains. The scattering intensity is integrated over the surface of a shell with a radius equal to the magnitude of \vec{Q} , and therefore only averaged properties can be extracted. On one hand the vibrational density-of-states (VDOS) can be obtained by coherent INS [12] or IXS [13] in the so - called “incoherent approximation”, or by incoherent INS. On the other hand the average longitudinal sound velocity can be investigated if the probing momentum transfer range is chosen to be inside the BZ around (0 0 0) [14]. Compared to single crystal work, the information content is therefore limited. This is an important constraint, since novel materials, or materials studied under extreme conditions, are often only available in polycrystalline form because of synthesis procedures or the presence of structural phase transitions. This has motivated researchers to circumvent the limited information content and explore methods to obtain detailed information on the lattice dynamics in polycrystalline materials.

Two different approaches have been undertaken, both using neutron powder diffraction. The method proposed by Dimitrov *et al.* [15] analyses the pair distribution function (PDF) obtained by a Fourier transformation of the integrated inelastic scattering intensity $S(Q)$. The parameters of a standard phonon model are then refined with respect to the experimental PDF and the phonon dispersion can be obtained with an accuracy of a few percent. This procedure can, however, only be applied to simple systems [16], [17], [18] and requires an appropriate model of the studied system. More recently, Goodwin *et al.* [19] proposed another method. They are analysing reverse Monte Carlo configurations refined to the neutron powder diffraction data. While the extracted phonon dispersion reproduces very well the low frequency modes, the high frequency modes cannot be determined precisely. This is due to the fact that optical branches have a small vibrational amplitude, and therefore give a small contribution to the diffuse scattering.

The intention of the present work is to overcome these limitations and to develop a methodology to extract the single crystal phonon dispersion from polycrystalline materials. The approach consists of recording IXS spectra over a large momentum transfer region (typically $2 - 80 \text{ nm}^{-1}$), and confront them with a Born - von Kármán model calculation which properly takes into account the polycrystalline state of the material and the IXS cross section. A least squares refinement of the model IXS spectra then provides the single crystal dispersion scheme. The development of the method and its application to the test cases of beryllium and textured graphite constitute the central part of this thesis work. Further studies were devoted to the cubic diatomic system MgO, for which the elastic constants can be extracted without a fit to the complete phonon dispersion, and

Introduction

tetragonal stishovite (SiO_2), where the IXS spectra are confronted without refinement to a theoretical calculation.

The thesis is structured as follows:

- Chapter 1 is dedicated to a brief review of the concepts of inelastic x-ray scattering from a single crystal, as well as single crystalline and aggregate elasticity. Furthermore, the formalism of inelastic scattering from a polycrystalline sample is presented, including a detailed discussion of the low momentum transfer limit and the density-of-states limit. At the end of the chapter the complementarities with inelastic neutron scattering are discussed.
- Chapter 2 is devoted to the principal concepts of extraction of single crystal dynamic properties from a polycrystalline sample. First, an overview of previous attempts is given. Then, the basic principles of the method, developed in the framework of this thesis are explained. Finally, the Born- von Kármán model, the computation of the IXS intensity in the case of scattering from a polycrystal, and the used least squares fitting routine are introduced.
- Chapter 3 provides a brief description of the IXS instrumentation and the utilised high-pressure equipment.
- Chapter 4 presents the experimental data and its analysis. It comprises studies on cubic MgO, hexagonal mono-atomic Be, textured hexagonal pyrolytic graphite and finally the diatomic tetragonal case stishovite.
- Chapter 5 discusses possible improvements of the developed method.

Introduction (française)

De nombreuses propriétés élastiques et/ou thermodynamiques peuvent être comprises en étudiant la dispersion des phonons. C'est par exemple le cas des propriétés à l'équilibre comme le coefficient d'expansion thermique, la capacité calorifique ou la température de fusion d'un matériau, mais aussi des propriétés de transport, du couplage électron-phonon, de la propagation d'ondes sonores ainsi que des constantes élastiques ou des forces interatomiques. L'étude expérimentale de la dispersion des phonons, qui consiste à déterminer l'énergie E d'un mode de vibration du réseau atomique en fonction de son moment \vec{Q} , est traditionnellement réalisée au moyen de spectroscopies neutroniques. Les neutrons sont en effet parfaitement adaptés à ce genre d'études puisque leur énergie caractéristique aux longueurs d'ondes correspondant aux distances interatomiques au sein de la matière est de l'ordre de 10 meV , et de fait comparable aux énergies typiques des phonons (quelques meV). De plus, le moment des neutrons permet de mesurer entièrement les dispersions, contrairement aux techniques de diffusion de la lumière (diffusion Brillouin ou Raman) qui ne sondent que les excitations de centre de zone.

Les rayons X constituent une autre sonde qui peut être en principe utilisée pour déterminer les relations de dispersion au travers de la zone de Brillouin. Cependant, dans de nombreux ouvrages classiques de physique de la matière condensée, les auteurs soulignent que cela représente un formidable défi au niveau expérimental, essentiellement parce qu'un instrument basé sur le rayonnement X destiné à de telles mesures devrait posséder une résolution énergétique extrêmement grande, de l'ordre de $\Delta E/E = 10^{-7}$. Ainsi, nous trouvons dans le *Solid State Physics* d'Ashcroft et Mermin, à propos de la possibilité de mesurer des phonons à l'aide de rayons X, le passage suivant: *In general the resolution of such minute photon frequency shifts is so difficult that one can only measure the total scattered radiation of all frequencies...* " [1]. Ainsi, les premières tentatives pour extraire la dynamique des réseaux d'expérience de rayons X ont été faites en analysant la diffusion diffuse autour des tâches de Bragg lors d'expériences de diffraction. Il a été montré par Laval dès 1939 [2] que l'agitation thermique des atomes contribuait de manière importante à cette diffusion diffuse, qui pouvait dès lors fournir des informations pertinentes concernant la dynamique du réseau atomique. L'une des premières expériences mesure-

ant la diffusion diffuse le long des directions de haute symétrie à été réalisée par Olmer en 1948 sur de l'aluminium fcc [3], travail complété par Walker en 1956 [4]. De surcroit, combinées avec la théorie de la dynamique des réseaux de Born, de telles mesures ont permis à Curien [5] et Jacobsen [6] de remonter aux constantes de forces interatomiques, et ce jusqu'aux interactions entre troisièmes plus proches voisins, dans le fer- α et le cuivre respectivement. Il n'était en revanche pas possible à cette époque de mesurer directement les courbes de dispersion du fait du manque d'intensité diffusée. Dans les années 80, un spectromètre utilisant un générateur à anode tournante et possédant une résolution énergétique ΔE de 42 meV a été mis au point, mais le flux de photons n'était alors toujours pas suffisant pour réaliser une expérience de diffusion inélastique des rayons X (IXS pour Inelastix X-ray Scattering). L'avènement de la seconde génération de sources à rayonnement synchrotron a permis les premières expériences d'IXS. De grands efforts dans le développement de monochromateurs à rétrodiffusion (backscattering) pour rayons X ont permis d'atteindre dès 1986 une résolution de 11 meV pour une énergie incidente de 13.8 keV [8]. La première mesure d'une courbe de dispersion de phonon a été réalisée par Dorner *et al.* [9] à l'été 1986 sur un aimant de courbure du HASYLAB, Hamburg, sur le spectromètre INELAX. Les branches longitudinales acoustiques et optiques selon la direction [001] du béryllium ont été mesurées avec une résolution de $\Delta E = 55 meV$. Cette modeste résolution énergétique ainsi que le flux de photons incidents furent par la suite significativement améliorés par des améliorations techniques du monochromateur et l'installation du spectromètre INELAX sur une source wiggler du HASYLAB. Une résolution expérimentale de 9 meV fut ainsi atteinte en 1991 [10]. C'est avec l'arrivée des sources de rayonnement synchrotron dites de 3ème génération (anneaux de stockage entièrement dédiés à la production de rayonnement synchrotron au moyen d'éléments d'insertion (wigglers ou d'onduleurs)) et aux grands progrès faits en parallèle en optique X, qu'il a été possible de réaliser de manière routinière des expériences avec une résolution énergétique de 1.5 meV .

Il ya à ce jours dans le monde cinq instruments dédiés à l'étude des phonons par IXS: les lignes ID16 et ID28 à l'European Synchrotron Radiation Facility (ESRF), en France, les secteurs 3ID et 30ID à l'Advanced Photon Source (APS), USA, ainsi que la ligne BL35XU du Super Photon Ring (SPring-8) au Japon. Aujourd'hui, l'utilisation des photons X est tout à fait complémentaire de celle des neutrons, en particulier parce qu'il existe un certain nombre de situations dans lesquelles les techniques à base de neutrons sont compliquées voire impossible à mettre en oeuvre. C'est en particulier le cas dans les systèmes désordonnés dans lesquels des excitations pseudo-acoustiques bien définies ne sont observables que dans la limite des faibles moment transférés (Q) (typiquement sous 10 nm^{-1}). De plus, dans les systèmes possédant une grande vitesse du son ($v_{sound} \sim E/Q$), il

n'est en général pas possible, aux énergies pertinentes, d'obtenir une résolution énergétique suffisante [11]. Ces restrictions cinématiques sont absentes dans le cas des rayons X. Un autre avantage non négligeable de l'utilisation des rayons X est la possibilité de mesurer des échantillons de faible volume ($10^{-7} - 10^{-4} \text{ mm}^3$), tandis que dans le cas des neutrons des volumes de l'ordre de plusieurs mm^3 sont nécessaires. Cela ouvre une variété de perspectives nouvelles dans l'étude des matériaux seulement disponibles en très faible quantité et/ou dans des conditions thermodynamiques extrêmes, comme les très hautes pressions.

Pour ces deux techniques (IXS et INS), un choix judicieux de la géométrie de diffusion permet la détermination complète de la dispersion des phonons dans un matériau monocristallin. Dans un matériau poly-cristallin, l'information contenue dans le moment \vec{Q} des excitations est perdue du fait de l'orientation aléatoire des cristallites. L'intensité diffusée est donc intégrée sur la surface d'une sphère de rayon $Q = |\vec{Q}|$, et seules des propriétés moyennées peuvent ainsi être extraites. D'une part, la densité d'états vibrationnels peut être obtenue par diffusion inélastique cohérente des neutrons [12] ou des rayons X [13] dans l'"approximation cohérente", ou par diffusion inélastique incohérente des neutrons. D'autre part, il devient possible d'accéder à la vitesse du son longitudinale moyenne lorsque le moment transféré à l'échantillon par la sonde (photon X ou neutron) est choisi de façon à se trouver dans la première zone de Brillouin [14]. En comparaison avec ce qui peut être obtenu sur un monocristal, les informations accessibles sur un poly-cristal sont ainsi plutôt limitées. Il s'agit là d'un élément assez contraignant vu que les nouveaux matériaux ou les matériaux étudiés dans des conditions extrêmes ne sont souvent disponibles que sous forme poly-cristalline du fait de problèmes de synthèse ou de présence de transitions de phases structurales. C'est ce qui a motivé les chercheurs à contourner ces limitations en développant des méthodes afin d'obtenir des informations détaillées sur la dynamique des réseaux dans les matériaux poly-cristallins.

Deux approches ont été tentées, utilisant toutes deux la diffraction de neutrons sur poudres. La méthode proposée par Dimitrov *et al.* [15] analyse la fonction de corrélation de paires obtenues par transformation de Fourier de l'intensité diffusée élastiquement $S(Q)$. Les paramètres d'un modèle standard de dynamique de réseau sont alors raffinés par rapport à la fonction de corrélation de paires obtenue expérimentalement, et les dispersions de phonons peuvent être obtenues avec une précision de quelques pourcents. Une telle procédure ne peut en revanche être appliquée qu'à des systèmes très simples [16], [17], [18] et nécessite *a priori* un modèle approprié pour le système étudié. Plus récemment, Goodwin *et al.* [19] ont proposé une méthode alternative: ils analysent des configurations obtenues par la méthode Reverse Monte Carlo, ajustées aux données de diffraction de neutrons sur poudres. Alors que les dispersions de phonons ainsi extraites reproduisent

très bien les modes de basse fréquence, les modes de plus haute fréquence ne peuvent pas être déterminées précisément. C'est principalement du au fait que les amplitudes de vibrations correspondant aux branches optiques sont en général relativement faibles, contribuant ainsi peu à la diffusion diffuse.

L'objectif du présent travail est d'outrepasser ces limitations et de développer une méthodologie pour extraire les dispersions de phonons du monocristal de données obtenues sur un matériau poly-cristallin. Notre approche consiste à enregistrer des spectres IXS sur une large gamme de moments transférés (typiquement $2 - 80 \text{ nm}^{-1}$), et de les confronter à un modèle de type Born - von Kármán qui prend correctement en compte l'aspect poly-cristallin du matériau ainsi que les sections efficaces de diffusion inélastique des rayons X. Un ajustement par la méthode des moindres carrés du spectre IXS ainsi modélisé fournit ainsi la dispersion des phonons dans le matériau monocristallin. Le développement de la méthode et son application aux cas d'écoles que sont le béryllium et le graphite texturé constituent l'artère principale de ce travail de thèse. Des études supplémentaires sur le système cubique diatomique MgO, pour lequel les constantes élastiques peuvent être extraites sans ajustement à la dispersion complète des phonons, ou encore à la stishovite (SiO_2 , maille tétragonale), pour laquelle les spectres IXS sont confrontés directement aux calculs théoriques, sont également présentées.

La thèse est organisée comme suit :

- Le chapitre 1 est dédié à une brève revue des concepts de diffusion inélastique des rayons X dans un monocristal, ainsi qu'à une introduction à l'élasticité dans les matériaux monocristallins et les agrégats. Nous présentons par ailleurs le formalisme attaché à la diffusion inélastique dans les matériaux poly-cristallins, ainsi qu'une discussion détaillée des limites densité d'états et à faibles moments transférés. A la fin de ce chapitre, les complémentarités des techniques de diffusion inélastique des neutrons et rayons X sont finalement discutées.
- Dans le second chapitre, nous présentons les principaux concepts nécessaires à l'extraction des propriétés d'un monocristal à partir d'un matériau poly-cristallin. En premier lieu, nous passons en revue les approches précédemment tentées. Puis, les principes de la méthode développée au cours de cette thèse sont introduits. Finalement, le modèle de Born-von Kármán, le calcul de l'intensité IXS dans le cas de la diffusion par un poly-cristal, ainsi que la méthode d'ajustement par les moindres carrés utilisée sont présentées.
- Dans le chapitre 3 nous décrivons le spectromètre IXS et les équipements utilisés pour les mesures haute pression.

-
- Le chapitre 4 présente les données expérimentales et leur analyse. Il comprend les études sur le composé cubique MgO, le béryllium hexagonal, le graphite pyrolytique texturé et finalement le cas diatomique de la stishovite.
 - Enfin, nous discutons dans le chapitre 5 les développements ultérieurement envisageables de la méthode.

Chapter 1

Lattice dynamics and elasticity in crystalline materials

The relevant theoretical concepts of lattice dynamics and elasticity theory are outlined in this first chapter. The first part discusses single crystal properties, while the second part is dedicated to polycrystalline materials. Finally, the characteristics of inelastic neutron scattering and inelastic x-ray scattering are compared.

1.1 Single crystals

1.1.1 Inelastic x-ray scattering

The basis of inelastic scattering from a single crystal is covered extensively in textbooks [10], [12], [20], [21], [22]. In this section only a brief introduction is given for the case of X-rays.

The scheme of a typical scattering experiment is illustrated in Fig. 1.1. The sample is illuminated by an incident wave with a well defined wave vector \vec{k}_i , energy E_i and polarisation $\hat{\varepsilon}_i$. After interaction with the sample, the wave is scattered into a state with wave vector \vec{k}_f , energy E_f and polarisation $\hat{\varepsilon}_f$. The momentum and energy conservation impose for the transferred momentum \vec{Q} and energy E :

$$\vec{Q} = \vec{k}_f - \vec{k}_i \quad (1.1)$$

$$E = E_f - E_i \quad (1.2)$$

$$\vec{Q}^2 = k_f^2 + k_i^2 - 2k_i k_f \cos(\theta) \quad (1.3)$$

where θ is the scattering angle between the incident and scattered photon. The incoming and scattered wave vector have approximately the same modulus, since $E \ll E_i$ and

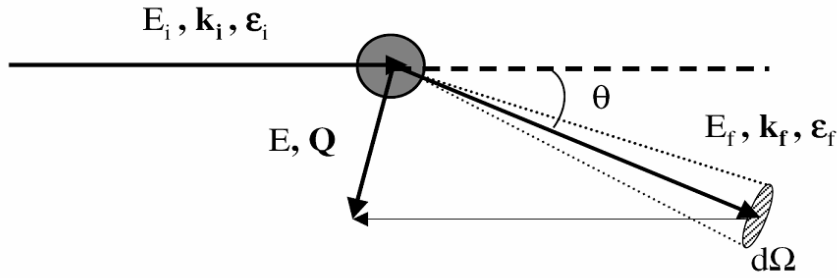


Figure 1.1: The scattering geometry

consequently the momentum transfer is simply connected to θ by (using the relation $\sin^2 x = \frac{1}{2}(1 - \cos 2x)$):

$$Q = 2k_i \sin \frac{\theta}{2} \quad (1.4)$$

The experimental observable is the double differential cross section:

$$\frac{d^2\sigma}{d\Omega dE_f} \quad (1.5)$$

It is proportional to the number of incident photons scattered into the solid angle element $d\Omega$ within the energy range E_f and $E_f + dE_f$. An expression for the cross section can be derived within linear response theory. The theory holds when the scattering of the probe requires only an understanding of the properties of the target, because the coupling between the probe and the system is weak and does not alter the intrinsic properties of the sample. The Hamiltonian, describing the electron-photon interaction in a scattering process, is composed, in the weak relativistic limit, of four terms [23]. Neglecting resonance phenomena close to x-ray absorption thresholds and the much weaker magnetic couplings, only the term arising from the Thomson interaction Hamiltonian has to be retained [24]:

$$H_{Th} = \frac{1}{2}r_0 \sum_p \vec{A}^2(\vec{r}_p, t) \quad (1.6)$$

where $r_0 = e^2/m_e c^2$ is the classical electron radius and $\vec{A}(\vec{r}_p, t)$ is the vector potential of the electromagnetic field in the \vec{r}_p coordinate of the p th electron. The sum extends over all electrons in the system.

The probability to transmit a plane-wave state $|\vec{k}_i\rangle$ defined by the wave vector \vec{k}_i to the plane wave state $|\vec{k}_f\rangle$ defined by \vec{k}_f is given in the framework of first order perturbation theory by Fermi's Golden Rule. Furthermore, the initial states of the sample are labeled by λ_i with the normalised eigenvectors $|\lambda_i\rangle$ and transit into final states $|\lambda_f\rangle$

due to inelastic scattering events. Equation 1.6 represents elastic and inelastic scattering and one obtains in the so - called first Born approximation for the cross section:

$$\frac{d^2\sigma}{d\Omega dE_f} = r_0^2 \left(\frac{k_f}{k_i} \right) (\hat{\varepsilon}_f \cdot \hat{\varepsilon}_i)^2 \sum_{\lambda_i \lambda_f} p_{\lambda_i} \left| \left\langle \lambda_f \left| \sum_p \exp(i\vec{Q} \cdot \vec{r}_p) \right| \lambda_i \right\rangle \right|^2 \delta(E + E_{\lambda_i} - E_{\lambda_f}) \quad (1.7)$$

Where \vec{r}_p is the position vector of the p th electron of the system and p_{λ_i} is the statistical weight of the initial states given by the equilibrium population. Since Fermi's Golden Rule is derived from perturbation theory, this expression for the cross section is as well only approximative. The differential cross section can be separated into two factors in a quite general way, states the validity of the adiabatic approximation, which assumes that the electrons follow the movements of the nuclei instantaneously. This allows separating the system quantum state $|\lambda\rangle$ into the product of an electronic and a nuclear part. This approximation is particularly good for exchanged energies that are small with respect to the electron excitation energies, as it is the case for phonons. The contribution to the total scattering coming from the valence electrons close to the Fermi level is small compared to the contribution coming from the core electrons. Consequently, the difference between the initial and final state is substantially due to excitations of the ion system. The double differential cross section can be expressed as:

$$\frac{d^2\sigma}{d\Omega dE_f} = r_0^2 \left(\frac{k_f}{k_i} \right) (\hat{\varepsilon}_f \cdot \hat{\varepsilon}_i)^2 \sum_{\lambda_{i,a}, \lambda_{f,a}} p_{\lambda_{i,a}} \left| \left\langle \lambda_{f,a} \left| \sum_n f_n(Q) \exp(i\vec{Q} \cdot \vec{r}_n) \right| \lambda_{i,a} \right\rangle \right|^2 \delta(E + E_{\lambda_i} - E_{\lambda_f}) \quad (1.8)$$

Here Q is the total momentum transfer. The scattering factor $f_n(\vec{Q})$ of the n th atom with position vector \vec{r}_n is the Fourier transform of the electron density. Due to the fact that the scattering occurs from the electronic cloud of the atom, $f(Q)$ is equal to the atomic number Z for $Q \rightarrow 0$ and decays almost exponentially with increasing momentum transfer. The sum n extends over all atoms of the system, while a refers to the nuclear states. Thus, the differential cross section can be separated into two factors in a quite general way as an immediate consequence of the use of momentum and energy transfers as independent variables [25].

$$\frac{d^2\sigma}{d\Omega dE_f} = \left(\frac{d\sigma}{d\Omega} \right)_{Th} \cdot S(\vec{Q}, E) \quad (1.9)$$

For given momentum and energy transfers the scattering function $S(\vec{Q}, E)$ is independent of the energy of the scattered photons as well as of the interaction potential. It describes the properties of the sample in the absence of the perturbing probe. $S(\vec{Q}, E)$ gives direct access to the dynamics of the system from an inelastic scattering experiment, whereas the

Thomson cross section

$$\left(\frac{d\sigma}{d\Omega}\right)_{Th} = r_0^2 (\hat{\varepsilon}_f \cdot \hat{\varepsilon}_i)^2 \left(\frac{k_f}{k_i}\right) \quad (1.10)$$

describes the coupling of the electromagnetic field of the photon to the electrons of the system. The factor $\left(\frac{k_f}{k_i}\right)$ is about equal to one in the case of IXS from phonons, because the transferred energy (10 – 100 meV) is much smaller than the energy of the incoming photons (14 – 25 keV), and incoming and scattered wave vector have approximately the same modulus.

Furthermore, the scattering factor $S(\vec{Q}, E)$ can be expressed as the Fourier transform of \vec{r} and t of the density-density correlation function. It contains information on the particle fluctuation in the target system in the different states at different times:

$$S(\vec{Q}, E) = \frac{1}{2\pi\hbar N} \int_{-\infty}^{\infty} dt \exp(-iEt/\hbar) \int d\vec{r} \exp(i\vec{Q} \cdot \vec{r}) \langle \rho(\vec{r}', t=0) \rho(\vec{r}' + \vec{r}, t) \rangle \quad (1.11)$$

with

$$\rho(\vec{r}, t) \equiv \sum_p \delta(\vec{r} - \vec{r}_p(t)) \quad (1.12)$$

N is the number of particles in the system and $\langle \rho(\vec{r}', t=0) \rho(\vec{r}' + \vec{r}, t) \rangle$ is the time dependent two-particle pair correlation function where the $\langle \dots \rangle$ denotes the ground-state expectation value of the density operator product. The summation p is over all target particles of the system. Thus in the classical limit, the pair correlation function gives the probability of finding a target particle at time t at $\vec{r}' + \vec{r}$, if there was any target particle at time $t = 0$ at \vec{r}' detected. The function $\rho(\vec{r}, t)$ can be specified in the case of phonon scattering in a crystalline sample and after insertion into 1.11 one obtains the scattering function:

$$S(\vec{Q}, E, T) = \sum_j \underbrace{\left| \sum_n f_n(Q) M_n^{-1/2} e^{-W_n} e^{i\vec{Q} \cdot \vec{b}_n} [\vec{Q} \cdot \hat{\sigma}_n(\vec{q}, j)] \right|^2}_{G(\vec{Q}, \vec{q}, j)} \underbrace{\frac{1}{1 - \exp\left(-\frac{E}{k_B T}\right)} \frac{1}{E_{\vec{q}, j}} \cdot [\delta(E - E_{\vec{q}, j}) - \delta(E + E_{\vec{q}, j})]}_{F(E, T, \vec{q}, j)} \quad (1.13)$$

$G(\vec{Q}, \vec{q}, j)$ is the dynamical structure factor with M as the mass of atom n at position \vec{b}_n in the unit cell. The summation n is over all atoms in the unit cell. The Debye-Waller factor e^{-W} is connected to the phonon frequency spectrum by:

$$2W = \left\langle \left(\vec{Q} \cdot \vec{u} \right)^2 \right\rangle \quad (1.14)$$

where \vec{u} is the displacement of the atoms. The thermal factor $F(E, T, \vec{q}, j)$ specifies the probability of creation or annihilation of a phonon. The normalised phonon eigenvectors $\hat{\sigma}(\vec{q}, j)$ describe the direction of the atomic vibrations of mode j with phonon

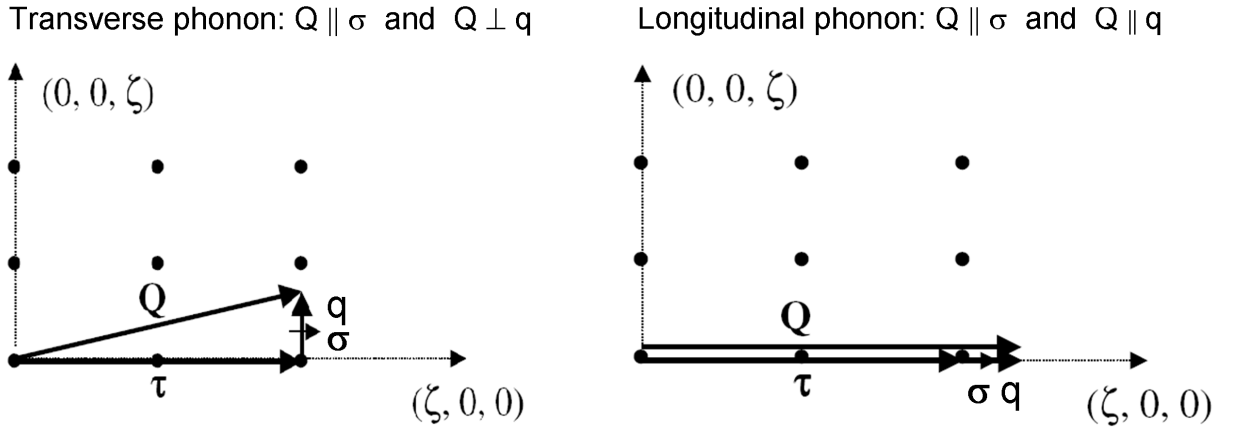


Figure 1.2: Scattering geometry in reciprocal space for the measurement of longitudinal and transverse phonons.

wave vector \vec{q} in a crystal lattice. Along the main symmetry directions of the crystal lattice in monoatomic systems the polarisation vectors $\hat{\sigma}(\vec{q}, j)$ of acoustic long wavelength excitations have a simple relation to \vec{q} . They are perpendicular or parallel to the propagation direction and hence the corresponding phonons are called transverse and longitudinal, respectively. In arbitrary directions, however, the relation between $\hat{\sigma}(\vec{q}, j)$ and the phonon wave vector is not simple and mixed vibrational modes are present. In the thermal factor denotes T the temperature, k_B the Boltzmann constant, and $E_{\vec{q}, j}$ the energy of the phonon. The "-" sign in the δ -function holds for creation and the "+" one for annihilation of a phonon.

The scalar product $\vec{Q} \cdot \hat{\sigma}_n(\vec{q}, j)$ in the dynamical structure factor imposes selection rules for detecting phonons. Only phonons with a component of the polarisation vector parallel to the scattering vector contribute to the scattering intensity. The scattering geometry for a measurement along a main symmetry direction is shown in Fig. 1.2. The scattering vector \vec{Q} can be expressed by:

$$\vec{Q} = \vec{k}_f - \vec{k}_i = \vec{\tau} + \vec{q} \quad (1.15)$$

where \vec{q} is the phonon wave vector, defined with respect to the nearest reciprocal lattice point $\vec{\tau}$. In order to detect longitudinal phonons, \vec{Q} has to be chosen along the symmetry direction of the crystal, whereas transverse phonons only can be detected for a momentum transfer, which is slightly off the main symmetry direction. In addition, the scattering process is subject of energy and momentum transfer conservation laws:

$$E_i = E_f + E_{\vec{q}, j} \quad (1.16)$$

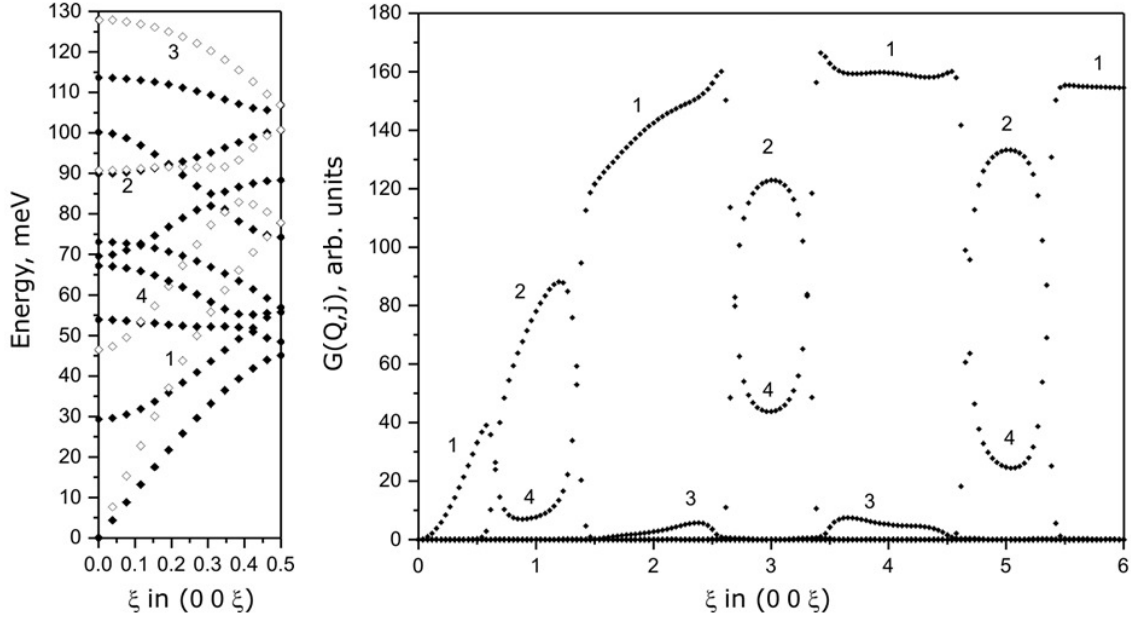


Figure 1.3: Phonon dispersion (left panel) and dynamical structure factor (right panel) for selected branches of stishovite along the (00 ξ) direction.

$$\vec{k}_f = \vec{k}_i + \vec{q} + \vec{\tau} \quad (1.17)$$

These conditions imply that for a given momentum transfer \vec{Q} only phonons of particular \vec{q} and $E_{\vec{q},j}$ give rise to a finite inelastic signal. To further illustrate this point we show in Fig. 1.3 the phonon dispersion of stishovite along the $\Gamma - Z$ direction (left panel) and the corresponding dynamical structure factor (right panel) for selected phonon branches. For example, the optical branch, labelled 2, is best determined for a momentum transfer around (001),(003) or (005), whereas phonons belonging to the longitudinal acoustic branch (labelled 1) have highest intensity around (002),(004) and (006). We furthermore note the general trend of increasing (decreasing) intensity with increasing momentum transfer (energy transfer).

A further important experimental aspect concerns the optimum scattering intensity. The flux of N scattered photons into the solid angle $\Delta\Omega$ and energy interval ΔE is given by:

$$N = N_0 \frac{\partial^2 \sigma}{\partial \Omega \partial E} \Delta \Omega \Delta E n L e^{-\mu L} \quad (1.18)$$

where N_0 is the incident photon flux, n the number of scattering units per unit volume, L is the sample thickness and μ the total absorption coefficient. The maximum IXS signal is achieved for $L = 1/\mu$. The dominating attenuation process is photoelectric absorption in almost all cases ($Z > 3$) for an x-ray energy above 10 keV. The photoelectric

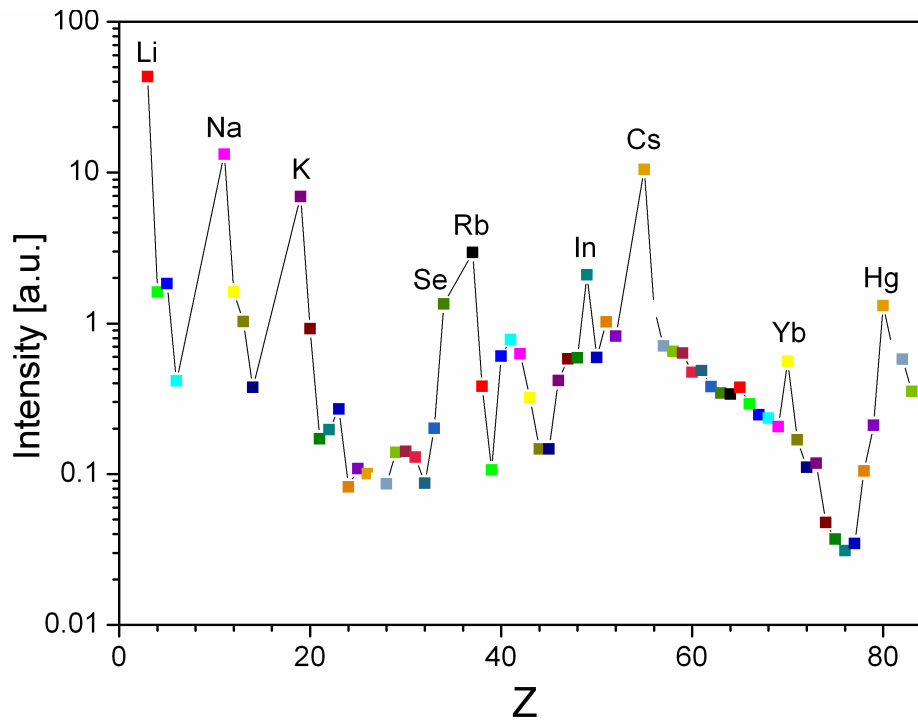


Figure 1.4: Efficiency of the IXS technique as a function of the atomic number Z in the small Q - limit and for the optimal sample thickness.

absorption process is roughly proportional to Z^4 , far away from electron absorption edges. Considering that the cross section for Thomson scattering σ_c is proportional to $|f(\vec{Q})|^2 \simeq Z^2$ (for small \vec{Q}), N is proportional to $1/Z^2$. With this assumptions, an estimate for the inelastic x-ray scattering intensity, I , can be obtained similar to the approach by [?].

$$I \propto \frac{L \exp(-L \cdot \mu) \rho Z^2}{\Theta_D^2 M^2} \quad (1.19)$$

where Θ_D and ρ are the Debye temperature and density, respectively. Figure 1.4 shows the the IXS signal I as a function of the atomic number Z for a monoatomic system with an optimal scattering length $L = 1/\mu$ and $f(Q) = Z$ for a x-ray energy of 17.794 keV . The alkali metals (Na, K, Rb, Cs) form an exception, since they are very soft (low Debye temperature) and have a low density. Furthermore, Se, In and Hg are soft materials, while Yb shows an exceptional high scattering intensity due to an anomaly in its density. The study of materials composed of heavy atoms is more difficult than the ones of low Z materials. On the other hand, in cases where the sample thickness is limited ($L \ll 1/\mu$) either due to its availability or constraints imposed by the sample environment (high pressure, high/low temperature, high magnetic field...) it is an advantage to study high Z materials. Further discussion, especially for the case of high pressure experiments,

using a diamond anvil cell (DAC), can be found in chapter 5.

1.1.2 Elasticity theory

Stress and strain Tensor

When the particles of a medium are displaced from their equilibrium positions, internal restoring forces arise which lead to oscillatory motions of the medium. The strain tensor ε describes the deformation due to such an acoustical excitation of a body. A method of exciting vibrations is to apply external forces at its surface. In this case the applied excitation does not act directly on particles within the body, but is transmitted to them by the means of stress σ acting between neighbouring particles. For small deformations it is an experimentally observed fact that the strain in a deformed body is linearly proportional to the applied stress. This is expressed in Hooke's law:

$$\sigma_{ij} = C_{ijkl}\varepsilon_{kl} \quad (1.20)$$

C is the elastic modulus or elastic tensor of rank 4 with $3^4 = 81$ components. The

strain and the stress tensors are symmetric matrices, thus $C_{ijkl} = C_{jikl} = C_{ijlk} = C_{jilk}$ which reduces the number of independent constants to 36. Furthermore, considering the definition of the strain energy

$$W = \sum_{ijkl} \frac{1}{2} C_{ijkl} \varepsilon_{ij} \varepsilon_{kl} \quad (1.21)$$

the following relation is obtained [26]:

$$C_{ijkl} = C_{klij} \quad (1.22)$$

This reduces the independent elastic constants to 21. This is the maximum number of elastic constants for any medium. If the crystal symmetry is considered, the number of independent values is normally further reduced. It ranges from 2 in an isotropic medium to 21 constants in the case of a triclinic system. Taking into account the symmetry of the tensors ε , σ and C each component can be specified by one subscript rather than two, following the Voigt notation:

$$\begin{aligned} (11) &\leftrightarrow 1 & (22) &\leftrightarrow 2 & (33) &\leftrightarrow 3 \\ (32) = (23) &\leftrightarrow 4 & (13) = (31) &\leftrightarrow 5 & (12) = (21) &\leftrightarrow 6 \end{aligned}$$

Hooke's law can then be written for the general case as:

$$\begin{pmatrix} \sigma_1 \\ \sigma_2 \\ \sigma_3 \\ \sigma_4 \\ \sigma_5 \\ \sigma_6 \end{pmatrix} = \begin{bmatrix} C_{11} & C_{12} & C_{13} & C_{14} & C_{15} & C_{16} \\ & C_{22} & C_{23} & C_{24} & C_{25} & C_{26} \\ & & C_{33} & C_{34} & C_{35} & C_{36} \\ & & & C_{44} & C_{45} & C_{46} \\ & & & & C_{55} & C_{56} \\ & & & & & C_{66} \end{bmatrix} \begin{pmatrix} \varepsilon_1 \\ \varepsilon_2 \\ \varepsilon_3 \\ \varepsilon_4 \\ \varepsilon_5 \\ \varepsilon_6 \end{pmatrix} \quad (1.23)$$

In the framework of this work cubic and hexagonal systems play a central role, and the explicit expression for the elasticity tensor is therefore listed below.

- **Cubic system** (three independent moduli C_{11}, C_{12}, C_{44})

$$C = \begin{bmatrix} C_{11} & C_{12} & C_{12} & & & \\ C_{12} & C_{11} & C_{12} & & & \\ C_{12} & C_{12} & C_{11} & & & \\ & & & C_{44} & & \\ & & & & C_{44} & \\ & & & & & C_{44} \end{bmatrix} \quad (1.24)$$

- **Hexagonal system** (five independent moduli $C_{11}, C_{33}, C_{44}, C_{12}, C_{13}$)

$$C = \begin{bmatrix} C_{11} & C_{12} & C_{13} & & & \\ C_{12} & C_{11} & C_{13} & & & \\ C_{13} & C_{13} & C_{33} & & & \\ & & & C_{44} & & \\ & & & & C_{44} & \\ & & & & & \frac{1}{2}(C_{11} - C_{12}) \end{bmatrix} \quad (1.25)$$

Sound velocity

The wave propagation in a medium can be described by the strain tensor ε and the equation of motion. As aforementioned, the strain tensor ε describes the distortion of the continuum system, when the particles of the medium are displaced from their equilibrium positions. The strain tensor is related to the particle displacement field u_{ij} through the following equation:

$$\varepsilon_{ij} = \frac{1}{2} \left(\frac{\partial u_i}{\partial r_j} + \frac{\partial u_j}{\partial r_i} \right) \quad (1.26)$$

where \vec{r} is the equilibrium position of the particle, \vec{u} the displacement field and $\frac{\partial u_i}{\partial r_j}$ is

the first partial derivative of the displacement along the i^{th} axis with respect to the j^{th} axis of the Cartesian coordinate system. Furthermore, the stress tensor σ represents the surface forces acting upon a unit cube and exciting vibrations in the body. The equation of motion of these vibrations is:

$$\sigma_{ij,j} = \rho \ddot{u}_i \quad (1.27)$$

where \ddot{u}_i is the second partial derivative of the displacement with respect to time and ρ is the density of the material. Substituting these two relations into Hooke's law (equation 1.20), we obtain:

$$C_{ijkl}u_{k,jl} = \rho \ddot{u}_i \quad (1.28)$$

where $u_{k,jl}$ is the second partial derivative of displacement with respect to j and l . As ansatz a plane wave $\vec{u}(\vec{r}, t) = A \vec{p} \exp(i(\vec{k} \cdot \vec{r} - \omega t))$ is used, where A is the displacement amplitude, \vec{p} is the polarisation vector, \vec{k} the wave vector, and ω the frequency. Thus the so - called Christoffel equation is obtained:

$$(C_{ijkl}n_j n_l - \delta_{ik} \rho \omega^2) p_k = 0 \quad (1.29)$$

δ_{ik} is the Kronecker delta and $n_j = \frac{k_j}{|\vec{k}|}$ is a unit vector in the direction of wave propagation. The Christoffel matrix is defined as

$$\Gamma = C_{ijkl} n_j n_l \quad (1.30)$$

It is only a function of the plane wave propagation along direction \vec{n} and the elastic constants. Since the (3×3) matrix is symmetric ($\Gamma_{lk} = \Gamma_{kl}$), it has at the most 6 independent components. Furthermore its eigenvalues are real and the eigenvectors are mutually orthogonal. The eigenvalue corresponds to the phase velocity of the acoustic wave and the associated eigenvector describes the polarisation of the wave. Focusing again on cubic and hexagonal systems, the corresponding Christoffel matrices are given by:

- **Cubic system**

$$\Gamma = \begin{bmatrix} C_{11}n_x^2 + c_{44}(n_y^2 + n_z^2) & (C_{12} + C_{44})n_x n_y & (C_{12} + C_{44})n_x n_z \\ (C_{12} + C_{44})n_x n_y & C_{11}n_y^2 + C_{44}(n_x^2 + n_z^2) & (C_{12} + C_{44})n_y n_z \\ (C_{12} + C_{44})n_x n_z & (C_{12} + C_{44})n_y n_z & C_{11}n_z^2 + C_{44}(n_x^2 + n_y^2) \end{bmatrix} \quad (1.31)$$

- **Hexagonal systems**

$$\Gamma = \begin{bmatrix} C_{11}n_x^2 + C_{66}n_y^2 + C_{44}n_z^2 & (C_{11} - C_{66})n_x n_y & (C_{13} + C_{44})n_x n_z \\ & C_{66}n_x^2 + C_{11}n_y^2 + C_{44}n_z^2 & (C_{13} + C_{44})n_y n_z \\ & sym. & C_{44}(n_x^2 + n_y^2) + C_{33}n_z^2 \end{bmatrix} \quad (1.32)$$

In the framework of the Christoffel equation it can be shown that in a crystal lattice the following relation is valid for the acoustic branches if $|\vec{k}| \ll \pi/a$, where a is the lattice parameter:

$$\omega_i(\vec{k}) = v_i n_i k \quad (1.33)$$

Here the frequency ω is linear in k , thus the group velocity is the same as the phase velocity v_i and both are independent of frequency. This relation can as well be found in the case of light waves and sound wave propagation. Thus, in the long wavelength limit ($\vec{k} \ll \pi/a$) the normal modes of the discrete crystal correspond to the sound waves of the elastic continuum. From this follows that determining the initial slope of the acoustic branches, and therefore the sound velocity of the solid, one can extract information about the elastic constants and vice versa. The set of crystallographic directions and the associated obtained elastic constants for cubic and hexagonal systems are given in table 1.1 and 1.2, respectively.

• **Cubic system**

$v_{LA[100]}^2$	= C_{11}/ρ
$v_{TA[100]}^2$	= C_{44}/ρ
$v_{LA[110]}^2$	= $(C_{11} + C_{12} + 2C_{44})/2\rho$
$v_{TA[110]<1\bar{1}0>}^2$	= $(C_{11} - C_{12})/2\rho$
$v_{TA[110]<001>}^2$	= C_{44}/ρ
$v_{LA[111]}^2$	= $(C_{11} + 2C_{12} + 4C_{44})/3\rho$
$v_{TA[111]}^2$	= $(C_{11} - C_{12} + C_{44})/3\rho$

Table 1.1: Longitudinal (LA) and transverse (TA) acoustic phonon branches for the extraction of the elastic constants in a cubic system.

• **Hexagonal system**

Furthermore the fifth unknown C_{13} can be obtained, and thus the complete stiffness tensor, once the other elastic moduli are known according to the relation:

$$QLA\{\alpha\} \rightarrow v = \left(\frac{A - \sqrt{B^2(C_{13} + C_{44})^2 \sin^2(2\alpha)}}{2\rho} \right)^2 \quad (1.34)$$

where QLA means a quasi longitudinal direction and

$$A = C_{11} \sin^2 \alpha + C_{33} \cos^2 \alpha + C_{44} \quad (1.35)$$

$$B = (C_{11} - C_{44}) \sin^2 \alpha + (C_{44} - C_{33}) \cos^2 \alpha \quad (1.36)$$

where α is the angle between the $[001]$ direction and \vec{k} and $C_{66} = 1/2(C_{11} - C_{12})$.

$v_{LA[100]}^2$	$= C_{11}/\rho$
$v_{TA[100]<1\bar{2}0>}^2$	$= (C_{11} - C_{12})/2\rho$
$v_{TA[100]<001>}^2$	$= C_{44}/\rho$
$v_{LA[110]}^2$	$= C_{11}/\rho$
$v_{TA[110]<1\bar{1}0>}^2$	$= (C_{11} - C_{12})/2\rho$
$v_{TA[110]<001>}^2$	$= C_{44}/\rho$
$v_{LA[001]}^2$	$= C_{33}/\rho$
$v_{TA[001]}^2$	$= C_{44}/\rho$

Table 1.2: Longitudinal (LA) and transverse (TA) acoustic phonon branches for the extraction of the elastic constants in a hexagonal system.

1.2 Polycrystalline Materials

This section develops the formalism for IXS from polycrystalline materials. Besides general aspects, the established cases of IXS at low momentum transfer and the extraction of the density-of-states from measurements at high momentum transfer are presented. Furthermore, the elastic properties of polycrystalline materials are discussed.

1.2.1 Inelastic x-ray scattering

In contrast to studies on single crystals, in polycrystalline materials it is not possible to determine the phonon dispersion along specific crystallographic directions, as only the magnitude of the momentum transfer \vec{Q} is defined. The scattering process takes place on a spherical shell with radius Q in reciprocal space and not on a point (as in the case of single crystals), and the scattering intensity is integrated over the surface of this shell. If the Debye-Waller factors are assumed to be the same for all types of atoms (\widetilde{W}) we obtain for this average intensity [14]:

$$S(Q, E, T) = g(Q, E')F(E, E', T) \quad (1.37)$$

with

$$g(Q, E') = \left\langle \left| \sum_n f_n(Q) e^{-W_n(Q)} M_n^{-1/2} \left[\vec{Q} \cdot \hat{\sigma}_n(\vec{q}, j) \right] \right|^2 \delta(E \mp E_{\vec{q},j}) \right\rangle \quad (1.38)$$

where the $\langle \dots \rangle$ means averaging over the sphere of radius Q and the phonon modes j . The thermal factor is given by:

$$F(E, E', T) = [1 - \exp(-E/k_B T)]^{-1} E'^{-1} [\delta(E - E') - \delta(E + E')] \quad (1.39)$$

For a given momentum transfer, contributions from various longitudinal and transverse phonon modes are in general present. The information content which can be extracted in the inelastic scattering experiment is therefore limited. Nevertheless, the average sound velocity can be investigated if the probing momentum transfer range is chosen to be inside the first BZ, where predominantly longitudinal contributions are detected. For momentum transfers beyond the first BZ, longitudinal and transverse acoustic (optic) phonons are contributing to the signal, and in the limit of very large momentum transfers the phonon density-of-states can be determined (see further below).

IXS at low momentum transfer

Within the first BZ, the reciprocal lattice vector τ is equal to zero, which leads to $\vec{Q} = \vec{q}$ and the scalar product in equation 1.38 becomes:

$$|\vec{q} \cdot \hat{\sigma}_n(\vec{q}, j)|^2 \quad (1.40)$$

This imposes the constraint that only components of the polarisation vector parallel to the propagation contribute to the dynamical structure factor within the first BZ. For pure longitudinal acoustic (LA) phonons, propagation and eigenvector are parallel to each other, and they dominate the inelastic scattering intensity. Contrary, pure transverse acoustic (TA) phonons do not contribute. On the other hand, low Q-scattering from quasitransverse acoustic (qTA) phonons can occur, because their eigenvector has a finite component along Q, and their contribution to the IXS spectrum can become non-negligible. A more detailed discussion can be found in [14].

In the long wavelength limit the displacements of different atom species become collinear and parallel to the eigenvectors of the corresponding elastic waves $\hat{\sigma}(\vec{n}, j)$, with $\vec{n} = \frac{\vec{Q}}{|\vec{Q}|}$. In this case the scattering from a polycrystalline material is completely defined by the macroscopic elasticity of the crystal:

$$g(Q, E) \rightarrow A \left\langle \left| \vec{Q} \cdot \hat{\sigma}(\vec{n}, j) \right|^2 \delta \left(E - v_{\vec{n},j} |\vec{Q}| \right) \right\rangle \quad (1.41)$$

where A is a scaling factor and $v_{\vec{n},j}$ the sound velocity, obtained from the Christoffel's equation (see section 1.1.2, equation 1.29).

Generally, the acoustic dispersion can be fitted by a sine function within the framework of the Born - von Kármán lattice dynamics theory and considering only next neighbour interactions [27]:

$$E = \frac{2\hbar}{\pi} v_L Q_{MAX} \sin \left(\frac{\pi Q}{2 Q_{MAX}} \right) \quad (1.42)$$

The resulting sound velocity v_L depends critically on the value of Q_{MAX} . In a single crystalline system it is equal to half the distance to the nearest reciprocal lattice point

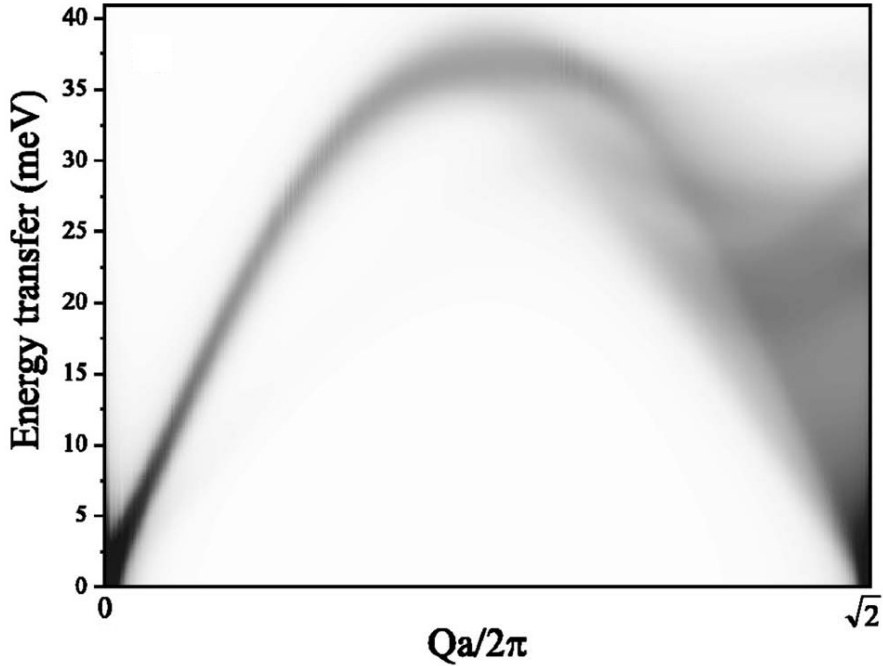


Figure 1.5: Theoretical $S(Q,E)/Q$ for polycrystalline bcc iron, represented as grayscale image. Figure taken from Bosak *et al.* [14].

in the direction of \vec{Q} , whereas the value of Q_{MAX} in a polycrystalline sample is not unambiguous, and a correct averaging scheme including preferred orientation of the grains has to be employed. Two different approaches are typically undertaken. In the first case the value of Q_{MAX} is left free, in the second case Q_{MAX} is fixed and corresponds to the radius of a sphere with the same volume as the first Brillouin zone. The advantage of the first case is that effects of texture are naturally taken into account while in the second case the number of free parameter is reduced. The validity and the limitations of these approaches are examined using the example of bcc iron [14].

The theoretical IXS spectra for the polycrystalline iron sample are calculated using a Born - von Kármán lattice dynamics model including force constants up to the 5th shell. The constant Q - spectra are convoluted with a typical resolution function of 3 meV FWHM, and the thermal factors are considered for 298 K. The resulting scattering intensity $S(Q, E)/Q$ as a function of energy transfer and reduced momentum transfer $Qa/2\pi$, where a is the lattice parameter, is shown in Fig. 1.5. At very low momentum transfer, up to about $Qa/2\pi = 1/\sqrt{2}$ the LA mode is very well defined. The scattering intensity shows only a small energy spread in this region. Above this value, the dispersion is increasingly smeared out and a phonon position can no longer be defined. The theoretical spectra were fitted using coupled pseudo - Voigt functions in order to reproduce typical

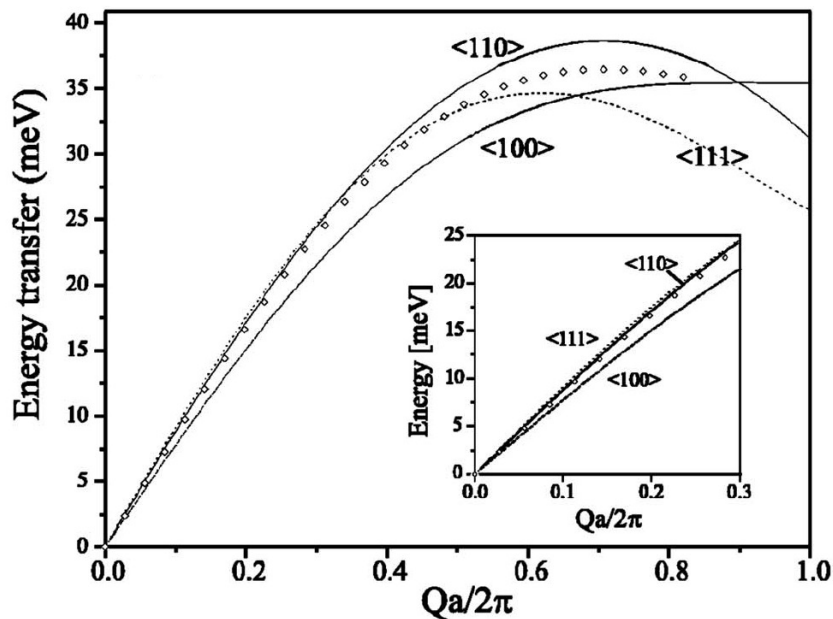


Figure 1.6: Simulated LA polycrystalline dispersion for bcc iron (open diamonds) compared to the single-crystal dispersion along main symmetry directions. Figure taken from Bosak *et al.* [14].

data analysis procedures. The open diamonds in Fig. 1.6 shows the obtained averaged LA dispersion in the polycrystal. Furthermore the LA branches along the main symmetry directions $\langle 100 \rangle$, $\langle 110 \rangle$ and $\langle 111 \rangle$ of the single crystal are represented as well. The inset shows the very low momentum transfer region, where the polycrystalline LA dispersion is very close to the single-crystal dispersion along the $\langle 110 \rangle$ and $\langle 111 \rangle$ directions.

If the sine fit is performed in the range up to the maximum of the dispersion, the resulting sound velocity is rather sensitive to the choice of Q_{MAX} (see Fig. 1.7). Considering the first case where Q_{MAX} remains free, the resulting value for Q_{MAX} is significantly lower than in the second case, where $Q_{MAX} = const$ and set equal to the theoretical value for the spherical approximation of the BZ. As a result, the sound velocities derived in these two ways differ significantly (see table 1.3). In addition, the obtained sound velocity value is sensitive to the dispersion fitting procedure. In the absence of very low Q -data, well within the linear $E(Q)$ regime, the choice of Q_{MAX} becomes crucial and attention must be paid to the data treatment.

Furthermore, the effect of texture on the sound velocity has to be considered. This is illustrated in Fig. 1.8, where axial pressure is applied to hexagonal cobalt. Due to the crystal symmetry, the c -axis is preferentially orientated along the pressure axis. As

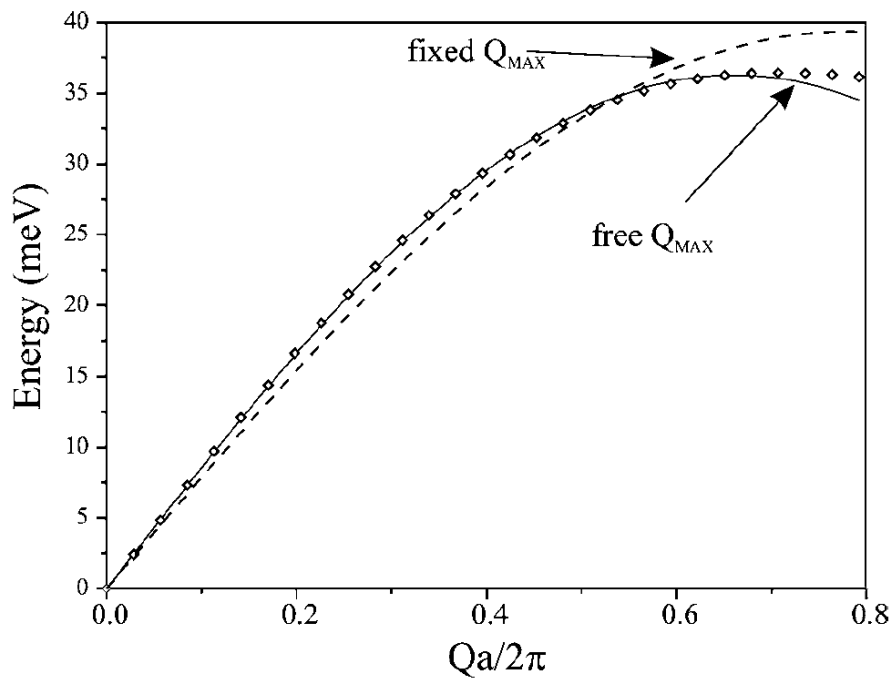


Figure 1.7: Sinusoidal fits to the simulated polycrystalline LA dispersion in bcc iron with Q_{MAX} fixed and free. Figure taken from Bosak *et al.* [14].

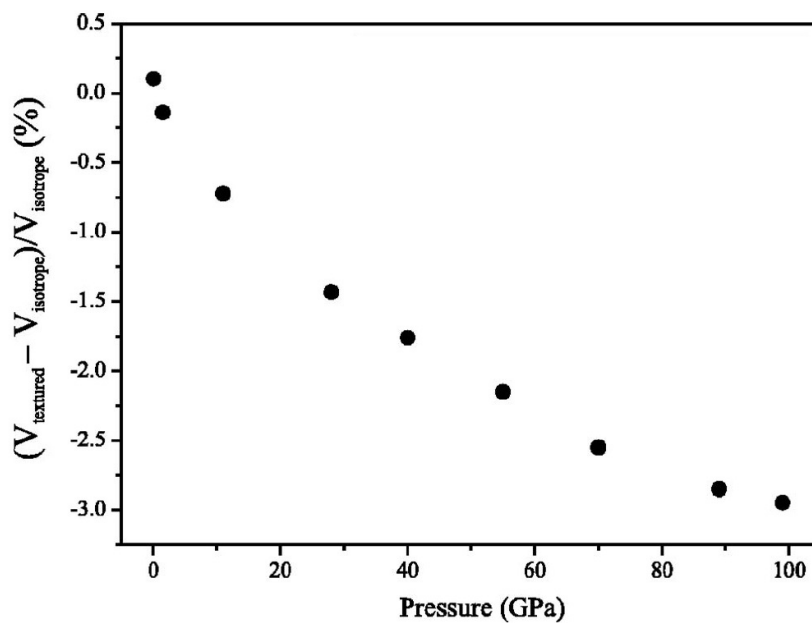


Figure 1.8: Deviation of the sound velocity in textured hcp cobalt from the true orientation average as a function of pressure. Figure taken from Bosak *et al.* [14].

velocity definition	Sound velocity [km/s]
<100> direction	5.414
<110> direction	6.148
<111> direction	6.357
Aggregate average (Hill)	5.912
Fit (Q_{MAX} fixed)	5.516
Fit (Q_{MAX} free)	6.009

Table 1.3: Comparison of LA sound velocities.

a consequence, the IXS experiment probes almost exclusively the sound velocity in the isotropic basal plane. The obtained sound velocity from the textured material deviates up to 3 % from the true orientation average. This shows that the effect of texture is not negligible and must be taken into account for the interpretation of the experimental data.

IXS in the density-of-states limit

The vibrational density-of-states (VDOS) gives the energy distribution $g(E)$ of the phonons, which can be measured using either INS or IXS. In monoatomic polycrystalline samples $g(E)$ can be determined directly, while in systems with different atomic species, only the generalised density-of-states can be obtained. There, the individual contributions of the different constituent atoms are weighted by their corresponding scattering length or atomic form factor.

In the case of INS from incoherent scatterers, the inelastic scattering spectra are directly proportional to $g(E)$ after proper correction for the Debye Waller factor and multiphonon contributions. As IXS is essentially a coherent scattering process, the "incoherent approximation", as developed for coherent INS [12], [28] needs to be applied [13]. This approximation is based on the assumption that for large momentum transfers the normalised $g(Q,E)$ should approach the generalised DOS:

$$g(Q, E) \longrightarrow A Q^2 \cdot \sum_n \frac{G_n(E)}{M_n} \cdot f_n^2(Q) \quad (1.43)$$

where $G_n(E) = \sum_{\vec{q}, j} |\hat{\sigma}_n(\vec{q}, j)|^2 \delta(E - E_{\vec{q}, j})$ are the partial density-of-states and A is a scaling factor. Several aspects have to be considered in order to ensure a correct VDOS approximation. Intuitively, the larger the momentum transfer, the better the approximation. However, the radius of the largest Q sphere is given by the maximum scattering angle of the IXS spectrometer. Typical values are between $70 - 90 \text{ nm}^{-1}$, depending on the energy resolution (further specifications are given in table 3.1, chapter 3). Another aspect concerns the thickness of the integration shell. While for INS there exists

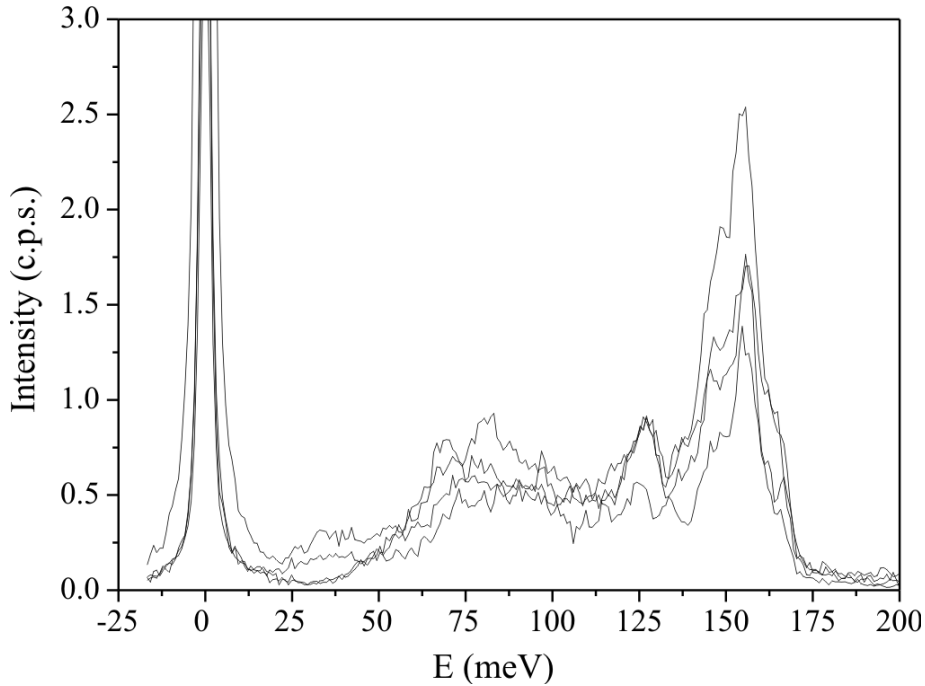


Figure 1.9: Raw IXS spectra of polycrystalline diamond at scattering angles of 45.5° , 47.0° , 48.5° , 50.0° . The instrumental energy resolution was 3.0 meV. Figure taken from Bosak *et al.* [13].

no constraints associated to this, since the neutron scattering length b is independent of Q , for IXS the atomic form factor $f(Q)$ decreases with Q . This leads to a distortion of the VDOS if the integration is performed over a large Q range. In general no recipe exists for the choice of the shell sampling, and the sampling procedure is empirical. Nevertheless in some special cases one can make semi-quantitative estimations for preferable settings [13].

In practice, the collection of typically 10 IXS spectra in the Q - range 50 to 70 nm^{-1} is sufficient to ensure a correct sampling. The VDOS is then determined after correction for the analyser efficiencies, as well as subtraction of the elastic line and multiphonon contribution, following a self - consistent deconvolution procedure [29].

We will show here the results of the application of this method to a monoatomic system, namely polycrystalline diamond [13]. The measurements were performed at beamline ID28 at the ESRF, with an energy resolution of 3.0 meV. In order to obtain the VDOS ten IXS spectra ($50 - 70 \text{ nm}^{-1}$ Q - range) were summed up. Figure 1.9 shows four representative IXS spectra. Note that there are distinct changes in the spectral shape. The obtained single-phonon VDOS agrees well with *ab initio* calculations [30], as can be appreciated in Fig. 1.10. The position of special points is nearly identical and furthermore

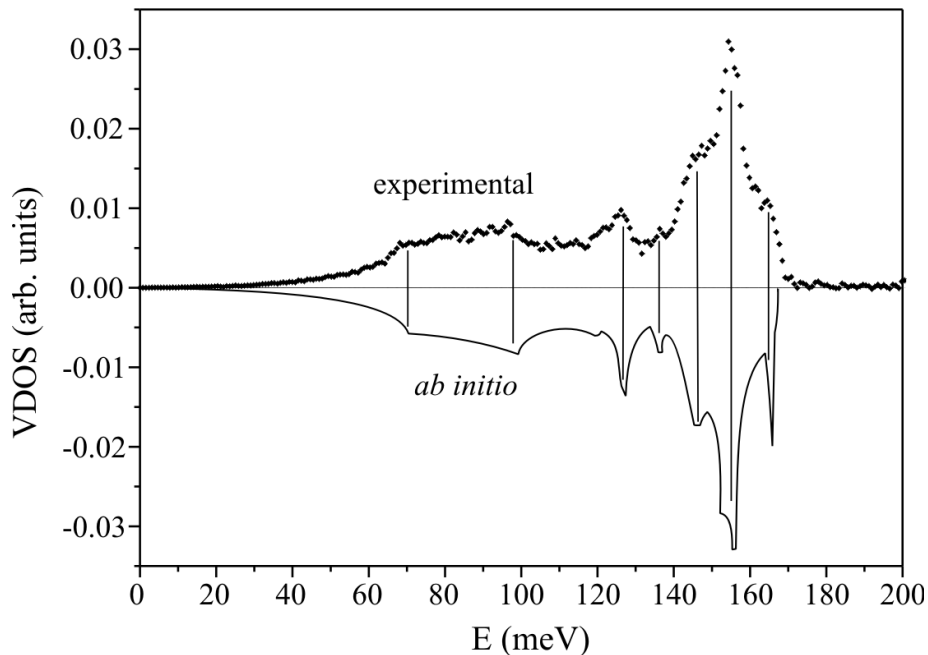


Figure 1.10: Reconstructed vibrational density-of-states of diamond versus calculated *ab initio* results [30]. The data are normalized to equal surfaces. Figure taken from Bosak *et al.* [13].

the high-energy peak, due to the overbending of the optical phonon branch, is clearly seen. The excellent quality of the experimental VDOS allows the determination of several macroscopic parameters such as Debye temperature and the average sound speed. The obtained values are in good agreement with other experimental data [13].

As already mentioned above, in the case of non-monoatomic crystals only a generalised VDOS can be obtained, nevertheless it can be shown [13] that the real VDOS can be recovered at least for the low-energy part. This allows the determination of material properties such as the low temperature limit of the Debye temperature θ_D and the effective sound speed even in systems with more than one atom species in the unit cell.

A parabolic fit to the low energy part of the VDOS yields the average sound speed v_D (Debye velocity):

$$g(\omega) = \frac{\omega^2}{\omega_D^3} \quad (1.44)$$

where

$$\omega_D^3 = 6\pi v_D^3 N/V \quad (1.45)$$

with N is the number of atoms in the unit cell and V is the unit cell volume. Finally one

can calculate the low-temperature limit of θ_D

$$\theta_D = v_D \frac{\hbar}{k_B} \left(\frac{6N_A \pi^2}{V_m} \right)^{1/3} \quad (1.46)$$

where k_B is the Boltzmann constant, N_A the Avogadro constant and V_m the molar mass. The Debye velocity v_D can be calculated via the following relation:

$$v_D = \left(\frac{1}{12\pi} \sum_{j=1}^3 \int \frac{1}{v_j^3} d\Omega \right)^{-1/3} \quad (1.47)$$

where v can be obtained from the Christoffel equation (see equation 1.29). The sum j extends over the three propagation polarisations. The integral over the solid angle $d\Omega$ can be limited to the sphere section, corresponding to the irreducible part of the Brillouin zone.

1.2.2 Elasticity theory

In a macroscopic non-textured polycrystalline material the elastic properties are generally considered to be isotropic. Nevertheless, the material is an aggregate of crystals whose properties are anisotropic. Different schemes are proposed to calculate the average elastic properties such as bulk modulus K , shear modulus G or aggregate compressional (longitudinal) and shear (transverse) sound velocities v_P and v_s in these materials. A simple solution is not possible, because the properties of the polycrystal depend not only on the elastic constants of the single crystal but also on the interaction between grains. A complete theoretical calculation has not yet been obtained and it is necessary to use an approximative average such as Voigt or Reuss. The two models utilise the anisotropic single-crystal elastic constants and give in the best case lower and upper bounds, respectively, for the aggregate properties. Here, general expressions for the bulk modulus K and the shear modulus G are given for both approximations.

In the Voigt approximation the field of distortion is uniform in the polycrystal, and therefore each grain experiences the same strain [31].

$$K_V = \frac{1}{9}(C_{11} + C_{22} + C_{33}) + \frac{2}{9}(C_{23} + C_{13} + C_{12}) \quad (1.48)$$

$$G_V = \frac{1}{15}(C_{11} + C_{22} + C_{33}) - \frac{1}{15}(C_{23} + C_{13} + C_{12}) + \frac{1}{5}(C_{44} + C_{55} + C_{66}) \quad (1.49)$$

In the Reuss average, the stress field in the material is considered to be uniform, and therefore each crystallite develops a strain that is proportional to the anisotropic modulus in a particular direction [32].

$$\frac{1}{K_R} = (S_{11} + S_{22} + S_{33}) + 2(S_{23} + S_{13} + S_{12}) \quad (1.50)$$

$$\frac{1}{G_R} = \frac{4}{15}(S_{11} + S_{22} + S_{33}) - \frac{4}{15}(S_{23} + S_{13} + S_{12}) + \frac{3}{15}(S_{44} + S_{55} + S_{66}) \quad (1.51)$$

where S_{ij} are components of the compliance tensor S , which is the inverse of the stiffness tensor C . In the Voigt-Reuss-Hill approximation the arithmetic average of the results of Voigt and Reuss is taken. This gives a more realistic value of the properties in the polycrystalline material.

In cubic and hexagonal symmetry the relations reduce to:

• **Cubic system**

$$G_V = \frac{C_{11} - C_{12} + 3C_{44}}{5} \quad (1.52)$$

and

$$G_R = \frac{5C_{44}(C_{11} - C_{12})}{4C_{44} + 3(C_{11} - C_{12})} \quad (1.53)$$

For the bulk modulus an unique expression can be obtained:

$$K = \frac{C_{11} + 2C_{12}}{3} \quad (1.54)$$

• **Hexagonal system**

$$K_V = \frac{1}{9}(2C_{11} + C_{33}) + \frac{2}{9}(2C_{13} + C_{12}) \quad (1.55)$$

$$G_V = \frac{1}{15}(2C_{11} + C_{33}) - \frac{1}{15}(2C_{13} + C_{12}) + \frac{1}{5}(2C_{44} + C_{66}) \quad (1.56)$$

and

$$K_R = \frac{C_{33}(C_{11} + C_{33}) - C_{13}^2}{C_{11} + C_{12} + 2C_{33} - 4C_{13}} \quad (1.57)$$

$$G_R = \frac{15}{4A(C_{11} + C_{12}) + 8AC_{13} + \frac{6}{C_{44}} + \frac{6}{C_{66}} + 2AC_{33}} \quad (1.58)$$

with

$$A = C_{33}(C_{11} + C_{12}) - 2C_{13}^2 \quad (1.59)$$

The aggregate compressional velocity v_p and aggregate shear velocity v_s in an elastically isotropic material without texture can be calculated for both cases from the bulk modulus K , the shear modulus G and the density ρ :

$$v_p^2 = \frac{1}{\rho} \left(K + \frac{4}{5} G_H \right) \quad (1.60)$$

$$v_s^2 = \frac{G_H}{\rho} \quad (1.61)$$

Here G_H is the shear modulus obtained by the Voigt - Reuss - Hill average. Within the same approximation scheme it is possible to express the Debye velocity using v_s and v_p by the following relation:

$$v_D = \left[\frac{1}{3} \left(\frac{2}{v_s^3} + \frac{1}{v_p^3} \right) \right]^{-1/3} \quad (1.62)$$

1.3 Inelastic x - ray scattering and inelastic neutron scattering

In the following the essential differences and complementarities of IXS and INS shall be highlighted with the aim to provide the interested reader with the necessary information to apply the developed formalism within this work to inelastic neutron scattering as well.

Neutrons couple directly to the nuclei through the Fermi pseudo - potential. The nucleus can be considered as a point mass, because the interaction range of neutron-nucleon interactions is much smaller than the wavelength of neutrons. The scattering is therefore isotropic and can be characterised by a single parameter; hence $f_n(Q)$ in equation 1.8 is replaced by b_n . The value of the scattering length b is not a systematic function of the atomic number; furthermore it is different for different isotopes and different total nuclear magnetic moments of the same atom species. This is in contrast to IXS, where $f(Q)$ varies only with the number of electrons Z . The double differential cross section for INS (to be compared with 1.8) is:

$$\frac{d^2\sigma}{d\Omega dE_f} = \left(\frac{k_f}{k_i} \right) \sum_{\lambda_i, \lambda_f} p_\lambda \left| \left\langle \lambda_f \left| \sum_n b_n \exp(i\vec{Q} \cdot \vec{r}_n) \right| \lambda_i \right\rangle \right|^2 \delta(E + E_{\lambda_i} - E_{\lambda_f}) \quad (1.63)$$

Only the average scattering potential - which varies because of different isotopes and the relative orientation of the nuclear spin to the neutron spin - gives rise to interference effects; and thus coherent scattering. It is proportional to the average of \bar{b} and hence the coherent scattering cross section is proportional to $|\bar{b}|^2$. The deviations from the average

1.3 Inelastic x - ray scattering and inelastic neutron scattering

potential are randomly distributed and therefore cannot give interference effects, they lead to incoherent scattering proportional to the mean-square deviation $|\overline{b - \bar{b}}|^2$. The total scattering cross section is therefore a sum of coherent and incoherent scattering:

$$\frac{d^2\sigma}{d\Omega dE_f} = \left(\frac{k_f}{k_i}\right) \left[|\bar{b}|^2 S_{coh}(Q, E) + \overline{|b - \bar{b}|^2} S_{inc}(Q, E) \right] \quad (1.64)$$

For the calculation of the scattering intensity of a polycrystalline material, one has to average over the coherent and incoherent part and $g(Q, E)$ becomes (see for comparison 1.38):

$$g(Q, E) = \left\langle \left\{ \left| \sum_n b_{coh} M_n^{-1/2} [\vec{Q} \cdot \hat{\sigma}_n(\vec{q}, j)] \right|^2 + \left| \sum_n b_{inc} M_n^{-1/2} [\vec{Q} \cdot \hat{\sigma}_n(\vec{q}, j)] \right|^2 \right\} \delta(E \mp E_{\vec{q}, j}) \right\rangle \quad (1.65)$$

An important advantage of neutrons is that the energy of incoming neutrons ranges from 0.1 *meV* up to values > 500 *meV*, thus covers the same range as the energy of phonons. A moderate ($\Delta E/E \sim 10^{-2}$) instrumental resolution in energy and momentum is therefore sufficient to determine the $S(Q, E)$ in the nm^{-1} and *meV* range. This is in contrast to X-rays where the energy of the incoming photons is in the *keV* range and orders of magnitude larger than the energy of the lattice vibrations. A much higher instrumental energy resolution ($\Delta E/E \leq 10^{-7}$) is therefore needed in order to resolve the same excitations. This implies a more sophisticated instrumentation (see chapter 3).

On the other hand, from the energy and momentum conservation law for particles with a mass

$$\hbar\omega = E_i - E_f = \frac{\hbar^2}{2m}(k_i^2 - k_f^2) \quad (1.66)$$

it is evident that for neutrons E and \vec{Q} are strongly coupled. The relation imposes kinematic constraints on the scattering experiments and not all (Q, E) -space is accessible in a neutron scattering experiment. While a large E - and Q range ($1 \mu eV < E < 1$ *eV* and $0.01 < Q (\text{\AA}^{-1}) < 30$) is accessible, there are constraints in the low momentum transfer region, typically within the first BZ where the reciprocal lattice vector $\tau = 0$ (see equation 1.17). Eliminating k_f from equation 1.66 we obtain:

$$\omega(\vec{q}) = \frac{\hbar}{m} \left\{ \frac{1}{2}(2\vec{k}_i \cdot \vec{q} - k_i^2) \right\} < \frac{\hbar}{m} \left\{ \vec{k}_i \cdot \vec{q} \right\} < \frac{\hbar}{m} k_i q \quad (1.67)$$

Applying now the linear relation between frequency and momentum transfer $\omega(\vec{q}) \simeq cq$ for small q , where c is the velocity of sound (see also section 1.1.2), it follows that there is only a solution of equation 1.66, if:

$$\frac{\hbar k_i}{m} > c \quad (1.68)$$

i.e. if the velocity of the incoming neutron is faster than the sound velocity in the material. Hence, if the incoming neutrons have such a low energy that their velocity is less than the velocity of sound in the crystal, the one-phonon coherent creation process has zero cross section. The velocity of thermal neutrons with an energy of 25 meV , for example, is about 3.0 km/s . This is slower than the sound velocity in hard materials, as for example in MgO (9.96 km/s). In the case of inelastic x-ray scattering energy and momentum transfer are very weakly correlated and all (Q, E) -space is accessible within the limits imposed by the energy resolution.

Within the context of the present work, the following aspects have to be considered if the proposed methodology is applied to inelastic neutron scattering:

- For materials with a sound velocity larger than the velocity of the incoming neutron, it is not possible to extract the orientation averaged longitudinal velocity from low Q data.
- Multiple scattering contribution emerge due to the weak absorption of neutrons in materials. Multiple scattering can cause distinct features in the inelastic scattering intensity and have to be taken into account in model calculations. For X - rays, the multiphonon contribution is generally weak, since for $Z > 3$ the cross section is dominated by photoelectric absorption. As a consequence, theoretical modeling for IXS spectra is less complex.
- A potential application of the proposed methodology is the study of materials in extreme conditions. One example concerns studies at very high pressures, for which typical sample volumes, compatible with diamond anvil techniques range between 10^{-4} to 10^{-7} mm^3 .

Further main differences between both methods are listed in table 1.4.

1.3 Inelastic x - ray scattering and inelastic neutron scattering

IXS	INS
flux $10^9 - 10^{11}$ <i>photons/s/200mA</i>	flux $10^7 - 10^8$ <i>neutrons/s/cm²</i>
no correlation between momentum and energy transfer	strong correlation between momentum and energy transfer
$\Delta E/E \approx 10^{-7} - 10^{-8}$	$\Delta E/E \approx 10^{-1} - 10^{-2}$
$\partial^2 \sigma / \partial \Omega \partial E f \sim r_0^2 Z^2$ (for small $ \vec{Q} $)	$\partial^2 \sigma / \partial \Omega \partial E f \sim b^2$ (b independent of $ \vec{Q} $)
$\partial^2 \sigma / \partial \Omega \partial E f$ dominated by photoelectric absorption	weak absorption \implies multiple scattering
no incoherent scattering	incoherent scattering contributions
no magnetic excitations	study of magnetic excitations
sample volume: $10^{-4} - 10^{-7}$ <i>mm³</i>	larger sample volume: $10 - 100$ <i>mm³</i>

Table 1.4: Overview of the main differences between IXS and INS.

Résumé du chapitre 1

Le premier chapitre passe en revue les éléments théoriques nécessaires à la compréhension de la diffusion inélastique des rayons X dans les monocristaux ainsi que dans les matériaux poly-cristallins. La section efficace différentielle de diffusion inélastique et ses liens au facteur de structure dynamique $S(\vec{Q}, E)$ sont dérivés. Les aspects expérimentaux tels que la géométrie de diffusion et l'intensité diffusée pour différentes espèces atomiques sont également discutés. Nous présentons également une revue des articles consacrés aux études dans les limites "densité d'états" et "à faibles moments transférés" dans le cas des matériaux poly-cristallins. Enfin, nous rappelons l'expression de la section efficace différentielle dans le cas de la diffusion inélastique des neutrons, et la comparons à celle des rayons X afin de souligner les apports spécifiques et la complémentarité de ces deux techniques. Les concepts théoriques de la théorie de l'élasticité sont également présentés. Nous donnons explicitement les relations entre le tenseur d'élasticité et la matrice de Christoffel dans le cas de systèmes monocristallins cubiques et hexagonaux. Pour les matériaux poly-cristallins, nous introduisons les modules de cisaillement et de compressibilité puis donnons une expression de la vitesse de Debye.

Chapter 2

Extraction of lattice dynamics from polycrystalline samples

In experiments where single crystals of sufficient size are unavailable, IXS and INS experiments can yield only limited information because the direction of the momentum transfer is no longer defined. In the first part of this chapter a recent approach to extract the phonon dispersion of a polycrystalline system using neutron powder diffraction (NPD) is presented. The second part describes the principal concepts, the model calculation and the fitting routine, which are utilised to extract single crystal dynamical information from polycrystalline IXS spectra.

2.1 Powder diffraction

The use of neutron powder diffraction (NPD) data to extract phonon dispersion curves is a particularly attractive approach, since it is a straightforward and time efficient experimental method compared to inelastic neutron or inelastic x-ray scattering experiments. The observed scattering function $S(Q)$ contains information both on the structure and on the dynamics of the material, though the quality of this information is degraded through the integration over dynamical and directional degrees of freedom performed in powder diffraction experiments. The scattering factor $S(Q)$ can be transformed by a simple Fourier transformation into the pair distribution function (PDF), which essentially represents the probability of finding pairs of atoms separated by various distances in the crystal lattice. It was realised already in the 1960's [33] that such distribution function might give information regarding dynamical properties.

In the following two different approaches are presented. The first one, proposed by Dimitrov *et al.* [15], makes use of a lattice dynamics model to compute the theoretical static structure factor $S(Q)$. Via a Fourier transformation to real space, the theoretical

PDF is obtained. Then, a reverse Monte Carlo procedure is applied to refine the peak widths of the theoretical PDF to the experimental PDF. This procedure was applied to two materials, a metal (fcc Ni) and an ionic crystal (CaF_2), for which the phonon dispersion was obtained with an accuracy of a few percent. Furthermore, in order to study the sensitivity of the PDF to the shape of the phonon dispersion curves a systematic investigation of some simple systems (fcc Ni, CaF_2 , fcc Rh and fcc Nb) were carried out by Reichardt and Pintschovius [16]. The PDF was computed for two different models, a very elaborate one, designed to describe the phonon dispersion curves published in literature with good accuracy and a second extremely simple one. The difference between the two resulting PDFs is very small, and consequently the authors conclude that very little can be learned about details of the phonon spectrum from such an analysis and only information contained in the thermal parameters can be extracted from NPD experiments.

A further study by Graf *et al.* [17] compared results obtained for simple fcc/bcc (Ni/Fe) and complex fcc/bcc (Pb/Nb) metallic systems. They generated synthetic PDF data from published tables for the force constants in a Born - von Kármán model, in order to avoid additional errors due to the corrections required for experimental NPD data. As initial point for the fitting routine, a Born - von Kármán lattice dynamic model was used. The model was then refined via a least squares fitting routine to this generated PDF. Several tests were made for each system with changing number of neighbours and varying values for the start parameter, viz. force constants. The thus obtained refined dispersions for the different starting models agree for Ni and Pb, but significant differences arise for the more complex systems Fe and Nb. The authors therefore concluded that one cannot obtain accurate phonon dispersions throughout the entire Brillouin zone from an inverse analysis of the pair distribution function, unless the lattice dynamics is very simple and fully described by a few phonon parameters as in the cases of fcc Ni and Pb. A semi-quantitative picture of the phonon dispersion, within a small fraction of the BZ center around the Γ point, may be obtained in simple and semi - complex metals, but not in metals with complex phonon dispersions. In summary one can say that the extraction of the dispersion from NPD data using this first approach is only feasible for systems with simple dispersion relations. Furthermore the method requires a good starting model, and consequently only a reasonable phonon model give reasonable fits to the diffraction pattern.

More recently Goodwin *et al.* [19] proposed a model free approach in order to overcome these limitations. They generate a large number of independent atomic configurations refined via the Reverse Monte Carlo (RMC) process to the experimental NPD data. Each of the such obtained configurations, consistent with the data, corresponds to a snapshot at a certain time of the set of atoms undergoing vibrational motions. In this

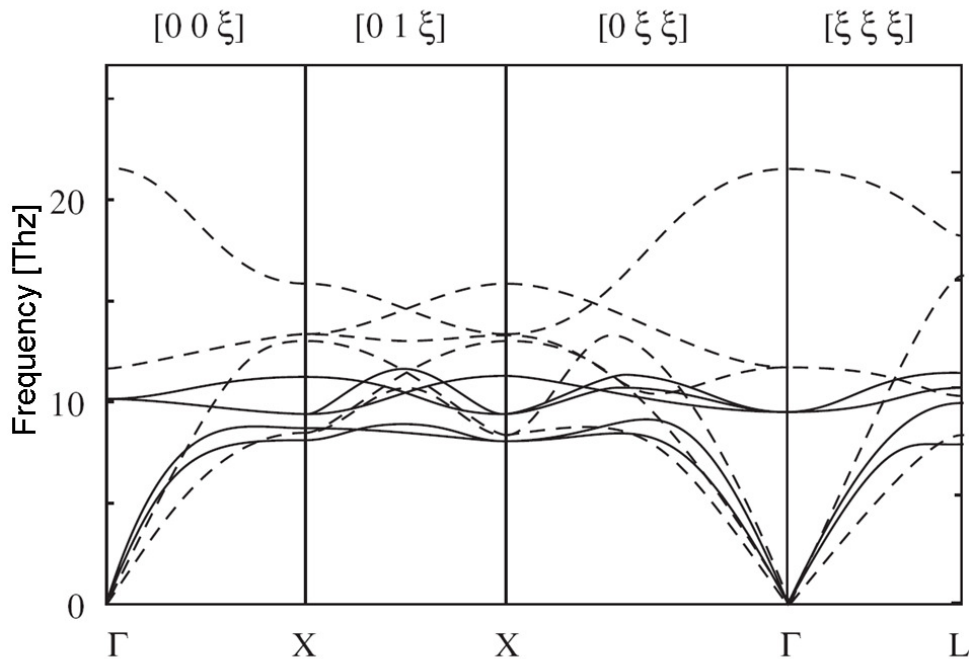


Figure 2.1: Phonon dispersion of MgO. The INS data (broken line) is compared to the dispersion extracted from neutron powder diffraction by Goodwin *et al.* (solid line). Figure taken from Goodwin *et al.* [34].

way the ensemble of configurations can be thought of a series of snapshots of the same system taken at different times, and a set of phonons across the Brillouin zone, e. g. the dispersion, can be derived. This approach was tested for two model systems, MgO and SrTiO₃ [35]. A qualitative agreement between the extracted dispersion and experimental single crystal dispersion can be observed. In the case of MgO (see Fig. 2.1) several features of the phonon dispersion are well reproduced, though a scaling problem for the phonon frequencies has to be noticed. The model fails, however, to reproduce the second TA branch along the [0ξξ] and the LO/TO splitting at the zone center, as well as some dispersion of optical branches. The latter is due to the fact that high frequency modes have a small vibrational amplitude and hence their effect on the diffuse scattering is small. As a consequence, significant parts of the optical phonon dispersions cannot be accurately determined. For SrTiO₃ the authors show that it is possible to observe a temperature-dependent mode softening utilising the proposed method. Concluding, certain aspects of the phonon dispersion can be extracted from the diffraction pattern, even if differences occur in the high-frequency part. Furthermore, one should keep in mind that the extracted dispersion is recovered from NPD data without imposing a phonon model.

The limitations of the two approaches discussed above explains the significant interest

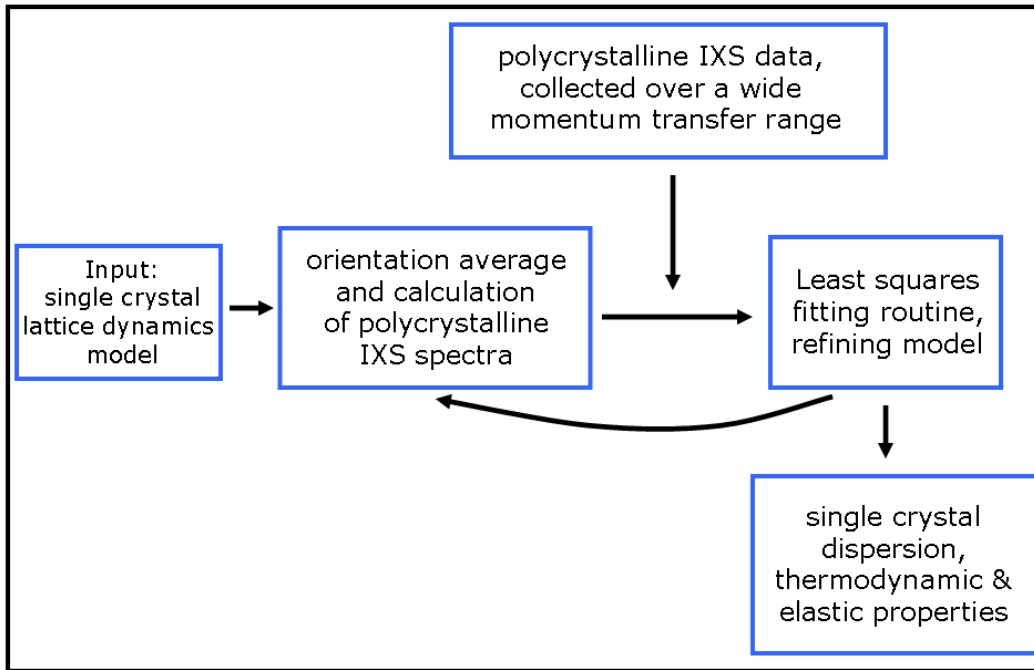


Figure 2.2: Schematic concept for the extraction of the single crystal phonon dispersion from polycrystalline IXS spectra.

in the development of alternative methods for obtaining detailed lattice dynamics information from polycrystalline samples, and provided the motivation for the development of the methodology laid out in the present work.

2.2 Inelastic x-ray scattering

This section is devoted to the methodology to extract single crystal properties from IXS spectra of polycrystalline samples recorded over a large momentum transfer range. The principal concepts are presented in the first part, before an insight into the model calculation, a brief explanation of the computation of the polycrystalline spectra, and a description of the least squares fitting routine is given.

2.2.1 Principal Concepts

The main concept of the method is illustrated in Fig. 2.2. On one side IXS data from the polycrystalline material are recorded over a large momentum transfer range. The energy scans at constant momentum transfer show not only distinct peaks at different energy but also different shape and intensity distributions. This is due to the development of the

spectra from the low Q limit within the first BZ, where primarily scattering from longitudinal phonons occurs due to selection rules, over the intermediate momentum transfer range where several phonons are excited at the same time, up to the high Q limit where the spectra approach the density-of-states limit. On the other side a theoretical model of the lattice dynamics in the single crystal is required. In the first test cases the Born - von Kármán model is utilised since it is easy to implement and is well documented in the literature. The force constants describing the interactions between neighbouring atoms are refined via a least squares fitting routine to the experimental polycrystalline IXS spectra. This process allows the confirmation and improvement of theoretical lattice dynamics models. The refined set of force constants is then utilised to calculate the single crystal phonon dispersion and to extract elastic and thermodynamic properties.

The starting parameters for the fitting routine are crucial for the success of the method. In order to prove the validity of the method and explore its limitations, a set of force constants derived from existing single crystal dispersions was taken for the first test cases. For real applications, this information is not available, but there are several possibilities to generate suitable starting parameters. One is to use force constants of a system with very similar properties, or the dynamical matrix can be obtained using empirical models such as rigid - ion or shell models. Furthermore, a set of Hellmann - Feynman forces can be computed with *ab initio* calculations.

2.2.2 The Born - von Kármán Model

We used the Born - von Kármán scheme, considering periodic boundary conditions, to model the lattice dynamics. The adiabatic approximation is used, treating the ion cores separately from the electrons. Thereby the motion of the ion cores is determined in a potential field generated by the average motion of the electrons. The model is largely described in the literature [1], [36], [37] and only a brief introduction will be given here.

The total potential energy of the crystal ν is a function of the position of all atoms. In general the shape of an interatomic potential is complicated even if, as in the present case, only two - body interactions are taken into account. ν can be expanded in a Taylor series in powers of a small displacement around its minimum at the equilibrium position $\vec{r}_{l\kappa}$ ($\vec{r}_{l\kappa} = \vec{r}_l + \vec{b}_\kappa$, where l labels the unit-cell position and b_κ the atom within each unit cell). The potential of a crystal with p atoms per unit cell, where the displacement of the b th atom in the l th unit cell is $\vec{u}(\vec{l}, \vec{b})$:

$$\begin{aligned} \nu &= \nu_0 + \sum_{lb\alpha} \frac{\partial \nu}{\partial u_\alpha(\vec{l}, \vec{b})} \Big|_0 u_\alpha(\vec{l}, \vec{b}) + \frac{1}{2} \sum_{\vec{l}, \vec{b}, \vec{l}', \vec{b}'} \Phi_{\alpha\beta}(\vec{l}, \vec{b}; \vec{l}', \vec{b}') u_\alpha(\vec{l}, \vec{b}) u_\beta(\vec{l}', \vec{b}') + \dots \\ &= \nu_0 + \nu_1 + \nu_2 + \dots \end{aligned} \tag{2.1}$$

$$\Phi_{\alpha\beta}(\vec{l}\vec{b}; \vec{l}'\vec{b}') = \sum_{\alpha,\beta} \frac{\partial^2 \nu}{\partial u_\alpha(\vec{l}\vec{b}) \partial u_\beta(\vec{l}'\vec{b}')} \Big|_0 \quad (2.2)$$

α and β are Cartesian coordinates. The first term ν_0 is a constant and is irrelevant in the present context. The second term is expressing a force and must vanish if the system is in equilibrium. The first nonvanishing term is therefore given by the quadratic term, which is the only term we consider here (harmonic approximation). In this picture an atom in a crystal can be described as a three dimensional harmonic oscillator. Moreover, in the Born - von Kármán model $\Phi_{\alpha\beta}(\vec{l}\vec{b}; \vec{l}'\vec{b}')$ represents the interatomic force constants between the atom b and b' . Generally the only restrictions to the components of the coupling constant matrix Φ are imposed due to the symmetry of the lattice, since the potential energy of the lattice ν_2 has to be invariant under rigid translation and rotation of the crystal, and to all symmetry operations belonging to the space group of the crystal. Thereby the number of force constants can be reduced.

It has to be considered that in a real solid the lattice vibrations are not harmonic and cannot rigorously be resolved into independent phonons, but for most materials the anharmonic term (mainly the third term in the Taylor series of the interaction potential) can be treated as a perturbation. The deviation of the interatomic potential from a parabolic form and its dependence on temperature and pressure, causes a shift of the phonon frequency and a broadening of its widths with temperature and pressure. In the quasiharmonic approximation a purely harmonic but temperature dependent coupling is used, in order to account for the phonon frequency shift.

The equation of motion of the b th atom with mass M_b in the adiabatic approximation is:

$$M_b \ddot{u}_\alpha(\vec{l}\vec{b}) = - \sum_{\vec{l}'\vec{b}'\beta} \Phi_{\alpha\beta}(\vec{l}\vec{b}; \vec{l}'\vec{b}') u_\beta(\vec{l}'\vec{b}') \quad (2.3)$$

To solve equation 2.3, a plane wave ansatz is made:

$$u_\alpha(\vec{l}\vec{b}) = \frac{1}{\sqrt{M_b}} \vec{\sigma}(\vec{b}, \vec{q}, j) \exp[i(\vec{q} \cdot \vec{r}_{l\kappa} - \omega t)] \quad (2.4)$$

where $\vec{r}_{l\kappa}$ is the equilibrium position vector of the l th unit cell and $\vec{\sigma}(\vec{b}, \vec{q}, j)$ is the polarisation vector, describing the direction in which the ions move. Substituting equation 2.4 into 2.3 an eigenvalue problem is obtained.

$$\omega^2(\vec{q}, j) \sigma(\vec{b}, \vec{q}, j) = \sum_{\vec{b}'\beta} D_{\alpha\beta}(\vec{b}\vec{b}'; \vec{q}) \sigma(\vec{b}', \vec{q}, j) \quad (2.5)$$

The eigenvalues $\omega^2(\vec{q}, j)$ and eigenvectors $\sigma(\vec{b}, \vec{q}, j)$ represent frequencies and polarisation vectors of the phonon mode j , respectively. Due to the hermitian character of

the dynamical matrix $D_{\alpha\beta}(\vec{b}, \vec{b}; \vec{q})$ the eigenvectors $\sigma(\vec{b}, \vec{q}, j)$ are orthonormal and the eigenvalues $\omega^2(\vec{q}, j)$ positive. In addition, for the crystal to be stable in the harmonic approximation, it is required that $\omega^2(\vec{q}, j) > 0$, and therefore $\omega(\vec{q}, j)$ has to be real. The term $D_{\alpha\beta}(\vec{b}, \vec{b}; \vec{q})$ is defined as:

$$D_{\alpha\beta}(\vec{b}, \vec{b}; \vec{q}) = \frac{1}{\sqrt{M_b M_b}} \sum_{\vec{l}} \Phi_{\alpha\beta}(\vec{l}, \vec{b}; \vec{l}, \vec{b}) \exp[i\vec{q} \cdot (\vec{x}(\vec{l}) - \vec{x}(\vec{l}))] \quad (2.6)$$

We used the program OpenPhonon [38] to diagonalise the dynamical matrix in order to obtain eigenvectors and eigenvalues for the single crystalline system. A few points have to be considered, when a Born-von Kármán model is chosen to describe the system:

- symmetry-related constraints on the elastic moduli are not automatically satisfied.
- an insufficient number of force constants can smoothen out the dispersion features.
- an excessive number of force constants makes the solution (fitting procedure) unstable and/or unphysical.

2.2.3 IXS intensity from a polycrystalline sample

The intensity scattered from a polycrystalline sample, which is composed of randomly orientated crystallites, is the sum of the contributions from these crystallites. So the directional information of the momentum transfer \vec{Q} is lost, only the magnitude $|\vec{Q}| = Q_{mag}$ is assigned. In order to compute the inelastic scattering intensity, one has to integrate over the surface of a sphere with radius Q_{mag} as illustrated in Fig. 2.3 for a system with hexagonal symmetry. The integration is performed in summing up discrete contributions on the sphere section, corresponding to the irreducible section of the Brillouin zone. The size of the section is given by the symmetry of the material. A proper sampling over this surface with a uniform mesh of points without gap or overlap is necessary. Since no analytical solution for a uniform grid on a shell surface exists, we have chosen a mesh with a constant step size ($\Delta\varphi = \Delta\theta = const.$) in the Euler angles φ and θ and $N_{\Delta\varphi}$ and $N_{\Delta\theta}$ nodes, respectively (see Fig. 2.4). The sampled \vec{Q} -points are situated in the center of the thus created sections of the sphere (red dots). It can be shown that the area of a single section $S_{point}(\theta)$ is given by:

$$S_{point}(\theta) = 2\pi Q_{mag}^2 (\cos(\theta) - \cos(\theta - \Delta\theta)) / N_{\Delta\theta} \quad (2.7)$$

$$= 2\pi Q_{mag}^2 \Delta\theta \sin(\theta) / N_{\Delta\theta} \quad (2.8)$$

This shows directly that each node has to be weighted by $\sin(\theta)$. Moreover, attention was paid so that none of the \vec{Q} -points coincides with high symmetry directions in order to

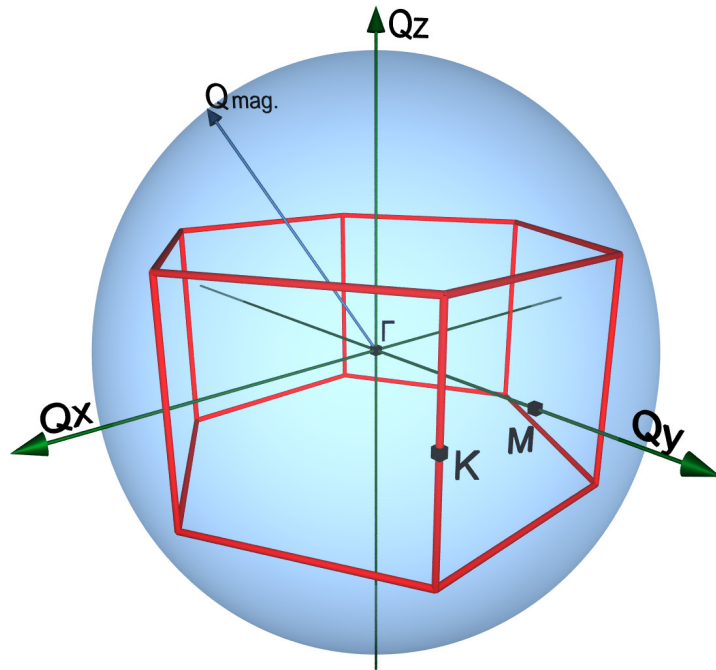


Figure 2.3: First Brillouin zone for hexagonal crystal symmetry and corresponding orientation average in the case of a polycrystal at a momentum vector Q_{mag} (blue sphere with $R = Q_{mag}$).

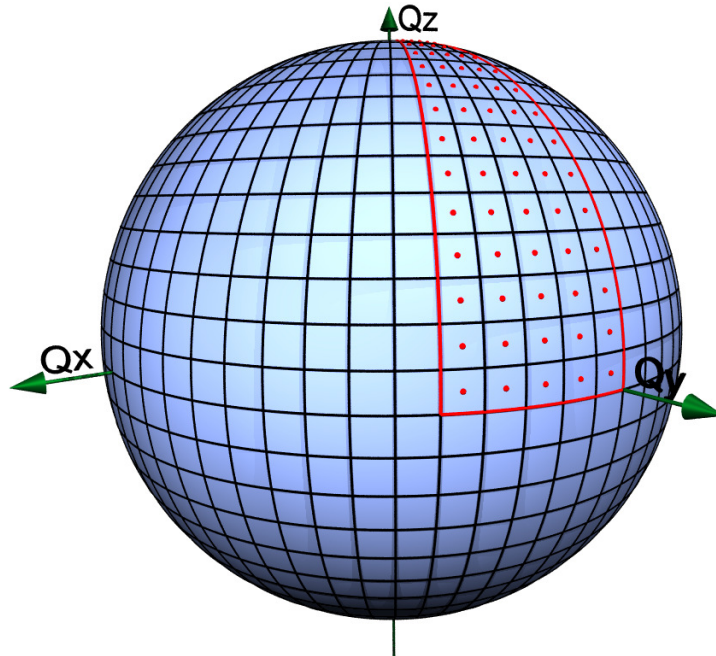


Figure 2.4: Schematic segmentation of the sphere in Fig. 2.3 and selection of the Q_{mag} points within the irreducible section of the sphere for hexagonal symmetry.

avoid singularities in the computed intensity distribution [39]. Convergence tests for the case of beryllium lead to a necessary sampling of 43200 points. The dynamical matrix was diagonalised for each \vec{Q} point and the obtained frequencies and polarisation vectors are used to compute the scattered intensity. Finally, the IXS intensities of all sampled \vec{Q} values are summed up, considering the weighting factor $\sin(\theta)$, and the obtained intensity distribution was convoluted with the experimental resolution function.

2.2.4 The Fitting procedure

The model calculations were refined to the experimental IXS spectra via a least squares fitting routine. The fitting parameters were the force constants a , the elements of the dynamical matrix. The maximum likelihood estimate of the model parameters is obtained by minimising the merit function χ^2 :

$$\chi^2 = \sum_{i=1}^N \left(\frac{y_{\text{exp}}(x_i) - y_{\text{mod}}(a, x_i)}{\sigma_i} \right)^2 \quad (2.9)$$

where y_{exp} is the experimental intensity and y_{mod} is the modeled intensity for the energy transfer x_i . We used the Levenberg - Marquardt algorithm [40], [41], which is an effective way to solve non - linear least squares problems [42], and is relatively rapidly converging. This method varies the parameters smoothly between the steepest descent method (far from the minimum) and the inverse-Hessian method (close to the minimum), switching continuously between the two, thus approaching the minimum. Far from the minimum the parameter a is changed by stepping down the gradient of the merit function χ^2 (steepest descent method):

$$\vec{a}_{\text{next}} = \vec{a}_{\text{current}} - c \times \nabla \chi^2(\vec{a}_{\text{current}}) \quad (2.10)$$

where c is a constant. Sufficiently close to the minimum the assumption is made that χ^2 is well approximated by a quadratic function. Within this assumption one can go directly from the current trial parameter a_{current} to the minimum parameter a_{minimum} (inverse-Hessian method):

$$\vec{a}_{\text{minimum}} = \vec{a}_{\text{current}} + \mathbf{D}^{-1} \cdot [-\nabla \chi^2(\vec{a}_{\text{current}})] \quad (2.11)$$

where \mathbf{D} is a constant matrix.

A flowchart of the procedure is shown in Fig. 2.5. The required input data to the program are the normalised experimental spectra and a starting set of force constants. Besides the main program - the least squares fitting routine - a second program, computing the model is needed. In this program, the IXS spectra are calculated, by diagonalising the dynamical matrix [38] and summing up the thus obtained intensities at Q-points on the

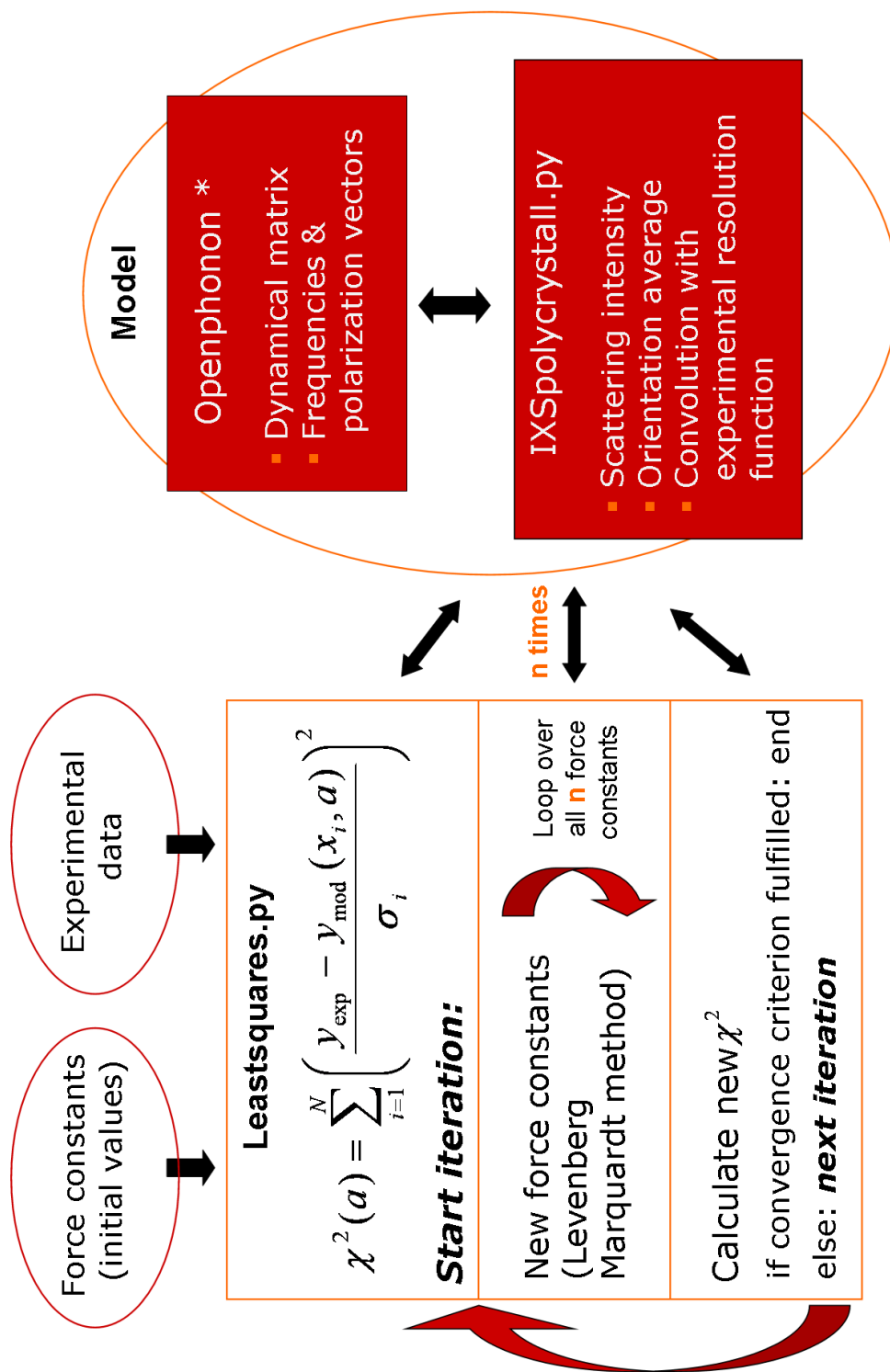


Figure 2.5: Scheme of the least - square fitting routine.

surface of a shell (see section 2.2.3). The program IXSpolycrystal.py was developed in the framework of this thesis. During the least squares fitting procedure the model parameters a are refined to the experimental data with the Levenberg - Marquardt method, until the following convergence criterion is met: $(\chi_{old}^2 - \chi_{new}^2) / \chi_{old}^2 = 0.0001$. Depending on the number of force constants, one iteration took between 4 h (17 parameters, graphite) and 6 h (29 parameters, beryllium) using a HP Proliant dual core computer (2.6 GHz, 8 GB RAM). Considering that one needs about 15 iterations for convergence, one fitting procedure took between 60 h and 90 h . In order to optimise the computing time, the program was parallelised, whereby the computing time can be reduced at the best by a factor corresponding to the number of force constants.

Extensive test runs revealed small fluctuations in the resulting set of force constants. They were noticed when changing the starting parameters or the number of mesh points used to compute the IXS intensity for the polycrystalline material. This is not surprising considering a n dimensional space of complicated topology, where n is the number of parameters. This problem is inherent to least squares routines near the minimum. If two different sets of parameters happen to fit the data about equally well, then the uncertainties of the parameters become ill-defined. Therefore, a convergence criterion is usually introduced in the fitting routine. Further discussions can be found in chapter 5.

Résumé du chapitre 2

Le chapitre deux est consacré aux méthodes numériques nécessaires à l'extraction des paramètres de dynamique de réseau des poly-cristaux. Dans la première partie de ce chapitre, nous présentons les approches modernes pour extraire la dispersion des phonons à partir de données de diffraction de neutrons sur poudres. La seconde partie décrit les principaux concepts de la méthode développée au cours de ce travail. L'idée maitresse est d'enregistrer des spectres IXS sur une large gamme de moments transférés, depuis la limite des faibles moments transférés jusqu'à celle de la densité d'états vibrationnelle. Les variations des énergies des pics et de leurs intensités relatives dans ces spectres sont alors utilisées pour ajuster un modèle théorique aux données expérimentales. Les intensités de diffusion inélastique dans le poly-cristal sont ici calculées via un modèle de Born - von Kármán, les constantes de force étant utilisées comme des paramètres ajustables. Ce chapitre introduit ainsi les modèles numériques ainsi que les procédures de moindres carrés utilisées lors des ajustement.

Chapter 3

Experimental techniques

In this chapter concepts and characteristics of the IXS beamline ID28 at the European Synchrotron Radiation Facility (ESRF) are presented. The principle of a diamond anvil cell, utilised for the high - pressure work on hcp iron, is described in the second part of this chapter.

3.0.5 The inelastic x - ray spectrometer

The experiments were carried out at ID28, one of the two inelastic x-ray scattering beamlines at the ESRF. The optical layout is based on a triple axis spectrometer. The first axis is the very high energy resolution monochromator selecting the energy of the incoming beam. The second axis controls the sample goniometry and the scattering angle, and therefore determines the momentum transfer \vec{Q} . Finally, the third axis is the crystal analyser, which analyses the photon energy. Figure 3.1 shows a schematic overview of the optics.

The experimental station is situated on a straight high- β undulator section of the electron storage ring. The energy of the x-ray beam depends on the opening of the undulator with $17.6 \text{ mm} / 32 \text{ mm}$ magnetic period and the used harmonics. Here the 1^{st} or 3^{rd} harmonics are utilised, respectively. The further characteristics of the emitted beam are a $40 \times 20 \text{ } \mu\text{Rad}$ angular divergence (horizontal \times vertical), a bandwidth $\Delta E/E = 10^{-2}$, and an integrated power within this divergence in the order of 200 W .

The emitted beam from the undulator is monochromatised by the high heat load pre-monochromator, a Si (1 1 1) channel-cut crystal. The x-ray beam then impinges on the main monochromator, a silicon ($h h h$) crystal with an asymmetry cut $\alpha = 75^\circ$ perpendicular to the vertical scattering plane, and operating at a Bragg angle of 89.98° . High order Bragg reflections and perfect crystals are required to obtain the necessary energy resolution of $\Delta E/E = 10^{-7} \div 10^{-8}$ [43]. The characteristics of the different reflections

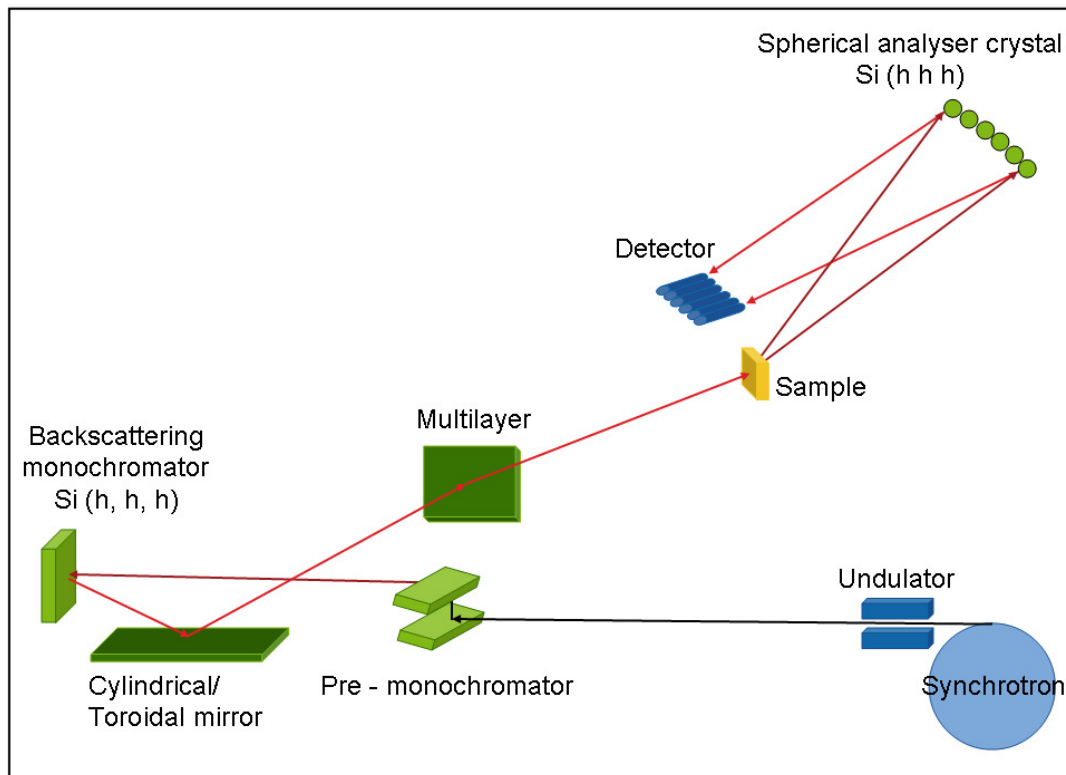


Figure 3.1: The layout of the inelastic scattering beamline ID28 at the ESRF.

h	Energy	ΔE	Q_{\max}	Q_{\min}	Flux
	[keV]	[meV]	[nm^{-1}]	[nm^{-1}]	[photons/s/200mA]
7	13.840	7.6 ± 0.2	64	1	$1.5 \cdot 10^{11}$
8	15.817	6.0 ± 0.2	74	1	$9.0 \cdot 10^{10}$
9	17.794	3.0 ± 0.2	83	1	$2.7 \cdot 10^{10}$
11	21.747	1.8 ± 0.1	101	1	$6.6 \cdot 10^9$
12	23.725	1.3 ± 0.1	111	1	$5.9 \cdot 10^9$
13	25.704	1.0 ± 0.1	120	1	$1.5 \cdot 10^9$

Table 3.1: Main characteristics of the ID 28 spectrometer for different $Si(h h h)$ reflections. Energy indicates the incident photon energy, ΔE is the total energy resolution; Q_{\max} and Q_{\min} indicate the accessible momentum transfers. The photon flux is measured at the sample goniometer with following experimental conditions: three 1.6 m U32 undulators, ring current 200 mA; primary slits aperture: 1.6 mm x 0.6 mm (horizontal x vertical); secondary slits aperture: 2.4 mm x 1.0 mm (horizontal x vertical).

$h = 7 - 13$ are given in table 3.1. For the present work we used the (9 9 9) configuration with an overall energy resolution of about 3 meV. The focusing optics is adaptable to the required spot size at the sample position. In the experiments within this work, two different setups were used. For powder samples at ambient conditions the beam was focused by the toroidal part of the platinum coated mirror giving a spot size of $260 \times 60 \mu\text{m}^2$ FWHM, horizontal \times vertical, respectively. For the high pressure experiments, we used a diamond anvil cell and a smaller spot size was needed. In this case the focusing was accomplished by the cylindrical part of the platinum coated mirror in the vertical plane (focal size about 60 μm) and a laterally graded multilayer in the horizontal plane (focal size about 30 μm). Due to the use of polycrystalline samples no further sample orientation was needed. After interacting with the sample the energy of the scattered photon is analysed by a silicon crystal. The angular acceptance of the analyser crystal depends on the desired momentum resolution. The ideal analyser crystal is therefore a spherical perfect single crystal with the ability to collect the scattered X-rays over a solid angle while conserving the intrinsic energy resolution. The solution to this challenging task consists of arranging approximately 12000 single crystal cubes with a size of $0.6 \times 0.6 \times 3 \text{ mm}^3$ onto a spherical substrate with radius R . The crystal analyser is placed at a distance from the sample $p = R$, thus fulfilling the Rowland circle condition. This configuration ensures that (i) a large solid angle of scattered X - rays can be collected without angular contribution to the energy resolution, and (ii) the intrinsic energy resolution is preserved thanks to the independent, unstressed single crystal array [44], [45].

Experimental techniques

The analysed photons are detected by a silicon diode detector with an active area of $2 \times 12 \text{ mm}^2$, which is inclined at 20° with respect to the backscattered x-ray beam from the analysers to maximise photoelectric absorption within its active thickness of 1.5 mm . The detector has a very low dark count of about 1 count in 30 min .

The ID28 beamline is equipped with nine such analysers arranged in the horizontal plane with a fixed angular offset. They are mounted on a 7 m long arm, which can be rotated between 0° and 55° around a vertical axis passing through the sample position. Thus nine IXS spectra at nine momentum transfers can be recorded simultaneously.

During experiments a fixed momentum transfer is chosen via the scattering angle 2θ between incident and scattered beam. The energy (wavelength) is scanned by changing the temperature T of the monochromator while keeping the energy (wavelength) of the analyser fixed. The following simple relation holds:

$$\Delta d/d = \alpha(T)\Delta T \quad (3.1)$$

where d is the lattice parameter. According to Bragg's law

$$n\lambda = 2d \sin \theta \quad (3.2)$$

a relative variation Δd corresponds to a variation of the diffracted energy $\Delta E/E = -\Delta d/d$. The required energy resolution of $10^{-7} \div 10^{-8}$ implies an accuracy of the temperature change of the backscattering monochromator in the mK range, considering the thermal expansion coefficient $\alpha \sim 2.58 \cdot 10^{-6} K$ for silicon. A carefully designed temperature bath, controlled by an active feedback system assures a temperature control with a precision of 0.2 mK in the temperature region around 295 K [43]. The temperature - energy conservation is accomplished utilising the recently published data on the thermal expansion coefficient $\alpha(T)$, determined by x-ray interferometry [46]:

$$\alpha(T) = \alpha_0 + \beta\Delta T \quad (3.3)$$

with $\alpha_0 = 2.581 \pm 0.002 \cdot 10^{-6} K^{-1}$, $\beta = 0.016 \pm 0.004 \cdot 10^{-6} K^{-2}$, $\Delta T = T - T_0$, and $T_0 = 22.5^\circ C$. Inserting this relation into 3.1 it follows:

$$\Delta d/d = -\Delta E/E = \int_{T_0}^T \alpha_0 + \beta(T' - T_0) dT' = (\alpha_0 - \beta T_0)\Delta T + \frac{1}{2}\beta(T^2 - T_0^2) \quad (3.4)$$

This expression allows the conversion from a temperature into an energy (wavelength) change.

Figure 3.2 shows the instrumental response function of one of the nine analysers corresponding to an energy resolution of 3 meV at the Si(9 9 9) reflection. It has been recorded by measuring the scattering from a cooled ($10K$) disordered sample (Plexiglas) at a momentum transfer corresponding to the first maximum of its static structure factor at $Q = 10 \text{ nm}^{-1}$, where the elastic contribution to the scattering is maximised.

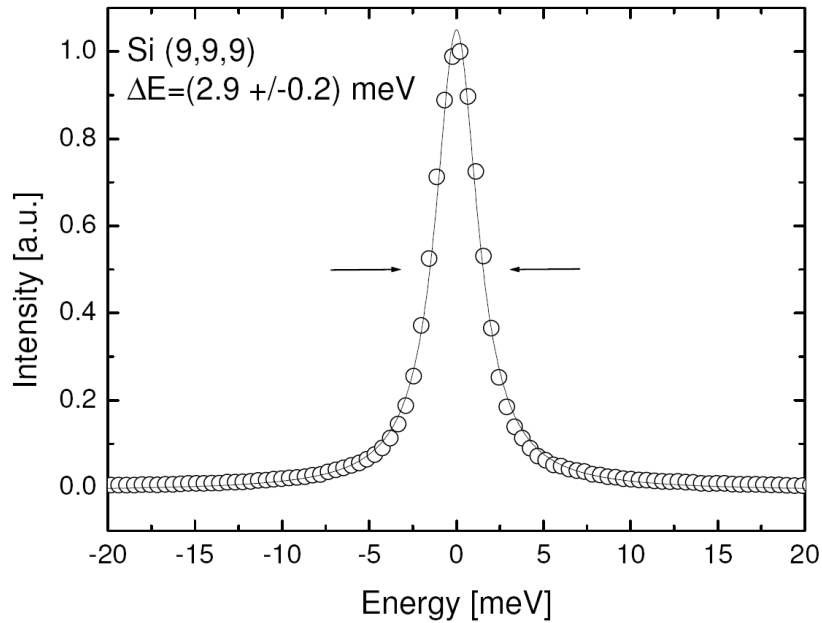


Figure 3.2: Instrumental response function measured at 17.794 KeV from the scattering of a Plexiglas sample at a momentum transfer corresponding to the first maximum of $S(Q)$.

3.0.6 The diamond anvil cell

The diamond anvil cell (DAC), developed in 1959 [47], is at the moment the device with which the highest pressures (well above 1 *Mbar*) are achieved. The importance of DAC's is not only due to their mechanical characteristics, but also to their optical properties. The diamonds are transparent to electromagnetic radiation from the far-infrared to γ -rays (except for the interval [3.5, 8000] *eV*, due to high photoelectric absorption). Thus many spectroscopic techniques and scattering techniques can be used to investigate materials at high pressure.

The main constituting elements of the DAC are:

- the body of the cell, essentially made out of a guided piston and a cylinder, which are able to slide one into the other.
- the pressurising system
- the diamonds supported by seats, in which a large variety of openings can be realised.

A schematic drawing of a DAC is shown in Fig. 3.3. Two diamonds of about 0.2–0.5¹ carats with a brilliant-like shape (Drukker cut), mounted with opposed tips, press a

¹1 carat = 0.2 grams.

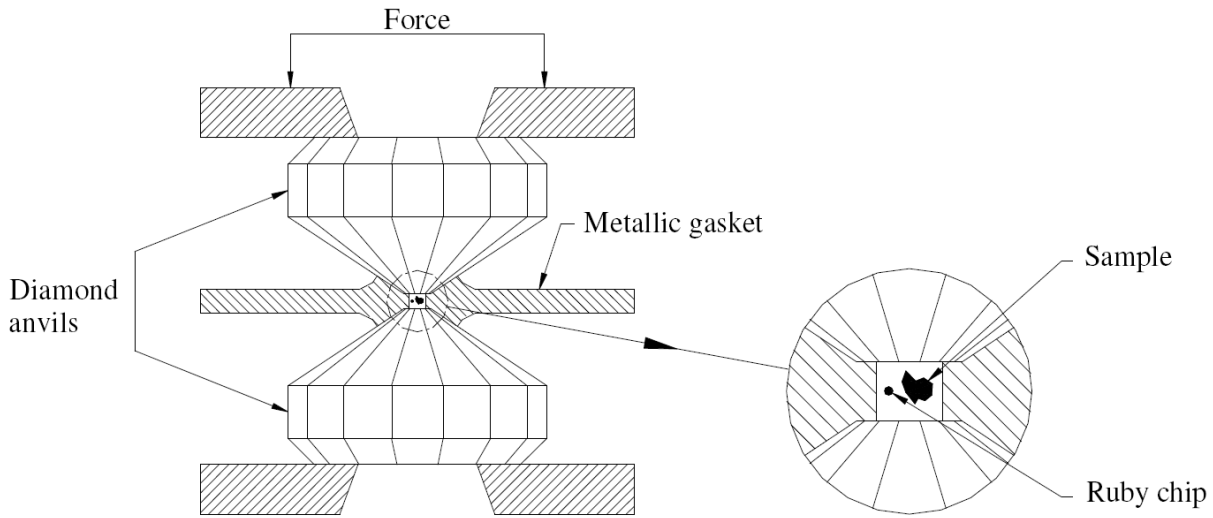


Figure 3.3: Schematic drawing of a diamond anvil cell and zoom of the sample chamber.

metallic thin sheet (gasket). A hole, drilled into the gasket, and centred with respect to the diamonds, constitutes the sample chamber. The sample and a pressure gauge (most commonly a small ruby chip) is placed inside this chamber, and the volume is filled with a pressure transmitting medium. The capability of generating pressures exceeding the megabar arises from the hardness of the diamond (10 on the comparative Mohs scale) and from the possibility to cut the stones with a surface ratio between the upper face and the culet of above 10^3 . As a consequence, a relatively small pressure applied on the cell will produce a much higher pressure on the sample ($P_{sample} > 10^3 P_{cell}$). In this context, the introduction of the gasket was a major improvement, since its plastic deformation under compression, and in particular the shrinking of the hole, allowed having a radial component in the strain and to achieve higher static pressures. Moreover, commonly the transformation of the induced uniaxial compression into isotropic (hydrostatic) pressure is desired. In the experiments carried out in this work we used helium, a very soft pressure transmitting medium, which provides excellent quasi-hydrostatic conditions at the used pressure of 20 *GPa*.

There are two different variants of DACs distinguished by the way the pressure is generated: the mechanical and membrane cells. Here we used a membrane DAC. This was first proposed around 1980 by William Daniels and the first DAC was constructed 1988 by Le Toullec and collaborators [48]. In such kind of cells the force is transmitted to the piston via gas pressure. Changing the pressure in the deformable metallic membrane allows a precise pressure control inside the sample chamber.

The pressure is determined by a small ruby crystal doped with Cr^{3+} placed inside the

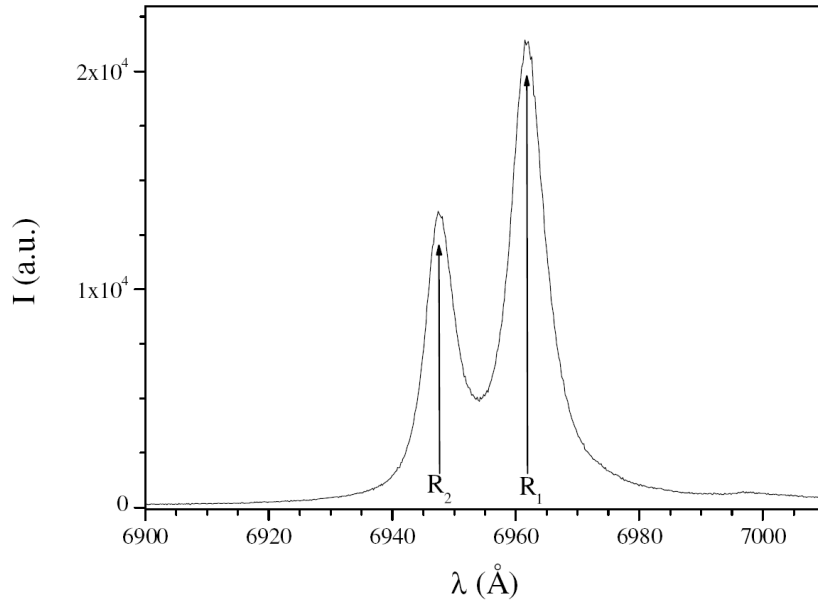


Figure 3.4: The ruby luminescence spectrum recorded at 5.4 GPa.

sample chamber. The ruby shows two intense luminescence peaks R_1 and R_2 (see Fig. 3.4). At ambient conditions they are at 6942 \AA and 6927 \AA , respectively. The pressure evolution of the frequency of the ruby luminescence lines has been calibrated several times [49], [50], [51], [52]. The shift of R_1 with pressure P is linear up to $\sim 20 \text{ GPa}$. For higher pressures it can be calculated from the expression proposed by Mao [53]:

$$P = \frac{0.274 * \lambda_{R_1}(0)}{B} \left[\left(\frac{\lambda_{R_1}(P)}{\lambda_{R_1}(0)} \right)^B - 1 \right] \quad (3.5)$$

where $\lambda_{R_1}(P)$ and $\lambda_{R_1}(0)$ are respectively the wavelengths at pressure P and at ambient conditions and the parameter B is related to the degree of hydrostatic pressure on the sample: $B = 5$ for non - hydrostatic conditions and $B = 7.665$ for conditions close to hydrostaticity [54].

Résumé du chapitre 3

Nous présentons dans le chapitre 3 la ligne de diffusion inélastique des rayons X ID28 de l'ESRF, Grenoble (France). Nous faisons un tour d'horizon du dispositif expérimental, des aspects techniques ainsi que des caractéristiques du spectromètre 3 axes utilisé au cours de ce travail. Nous introduisons enfin dans une seconde partie de ce chapitre le principe des cellules à enclume de diamant utilisées pour les mesures hautes pressions sur le fer hcp.

Chapter 4

Experimental results

In this chapter the performed experiments, the data analysis strategy and the obtained results are discussed. The main characteristics of the present study is its systematic nature. First, for the polycrystalline cubic system MgO the elastic constants are derived, continuing the work accomplished on the monoatomic system diamond [?]. This study is followed by hexagonal Be, for which the complete dispersion is extracted. Then the effect of a simple texture in the case of hexagonal graphite is treated. Finally, our methodology is applied to the tetragonal system SiO₂ (stishovite), establishing the possibility to support theoretical calculations.

4.1 Cubic system

In the case of cubic systems the number of independent elastic constants is limited due to symmetry to C_{11} , C_{12} and C_{44} . Thereby, three quantities a_j , which can be expressed as a function of the elastic constants, are sufficient to reconstruct the elastic tensor:

$$a_j = f(C_{11}, C_{12}, C_{44}) \quad (4.1)$$

In polycrystalline materials a can be chosen to be the bulk modulus K , the Debye velocity v_D , and the average longitudinal sound velocity v_P . Together with the density ρ of the material, these quantities are experimentally accessible. The bulk modulus K can be obtained by x-ray diffraction experiments on the polycrystalline material [55]. The Debye velocity v_D can be extracted from the low energy parabolic part of the vibrational density-of-states (VDOS), determined by inelastic x-ray scattering [13], and v_P can be derived from an inelastic scattering experiment at low momentum transfer.

Experimental results

4.1.1 Magnesium oxide

Magnesium oxide has been the subject of extensive theoretical and experimental investigations [56], [57], [58], [59], [60], [61], [52], which have revealed the fundamental bonding properties of the NaCl - type crystal structure. In high pressure and high temperature experiments, MgO is used as a pressure calibration standard. Moreover, MgO is a major component in the Earth's lower mantle, and knowledge of its high-pressure behavior is crucial for understanding deep Earth geophysics. Thus, it is often used as a benchmark for new theories and new experiments. Here, we use MgO to illustrate the extraction of the elastic tensor for cubic systems from a polycrystalline material.

4.1.2 Experiment

The average longitudinal sound velocity v_P was experimentally determined by inelastic x-ray scattering at low momentum transfer. MgO powder, obtained by grinding a single crystal, was placed in an aluminium holder between 8 μm thick Kapton foils. The sample thickness of 1.5 mm corresponded closely to the optimum thickness $t_{opt} = 1/\mu$, where μ is the photoelectric absorption coefficient. The sample quality was investigated by measuring a diffraction pattern. The obtained uniform intensity around the Debye - Scherrer rings signified a polycrystalline sample without texture.

The inelastic scattering experiment was performed utilising the silicon (9 9 9) setup, with a total energy resolution of 3 meV . The highly monochromatised X-rays were focused into a spot size of $250 \times 100 \mu m$ (horizontal \times vertical, full-width-half-maximum). To avoid background contributions due to scattering from air at low momentum transfer, the sample was placed into a vacuum chamber. Six spectra at low momentum transfer were recorded (2.0 nm^{-1} , 3.2 nm^{-1} , 4.4 nm^{-1} , 5.6 nm^{-1} , 7.8 nm^{-1} and 9.2 nm^{-1}), with a momentum resolution of 0.24 nm^{-1} and 0.7 nm^{-1} in the horizontal and vertical direction, respectively. The total acquisition time for each point was 240 s (200 mA storage ring operation mode).

4.1.3 Results

Figure 4.1 shows the six low Q IXS spectra. These are characterised by an elastic peak at zero energy transfer, and an inelastic peak corresponding to the superposition of LA phonons over the spherical surface of a given Q . The energy position of the inelastic feature was fitted by a pseudo-Voigt function after proper centering of the elastic line at $E = 0$. A sine fit to the average longitudinal dispersion as described in section 1.2.1, yields $v_P = 9.96 \text{ km/s}$ (see Fig. 4.2). Here Q_{MAX} was left free, as experimental data in the linear region ($Q \propto E$) are available.

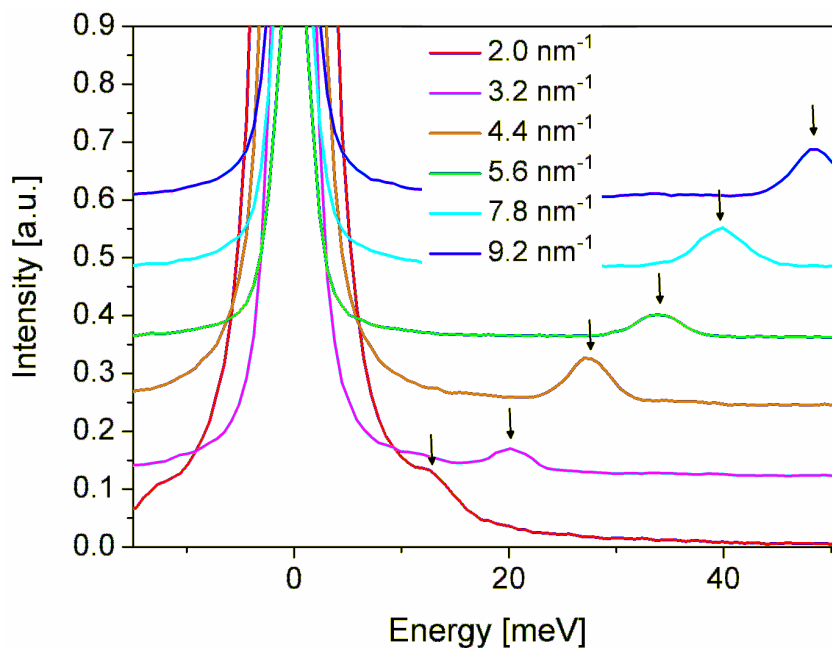


Figure 4.1: IXS spectra of MgO at different momentum transfers. The inelastic features due to longitudinal excitations are marked with arrows.

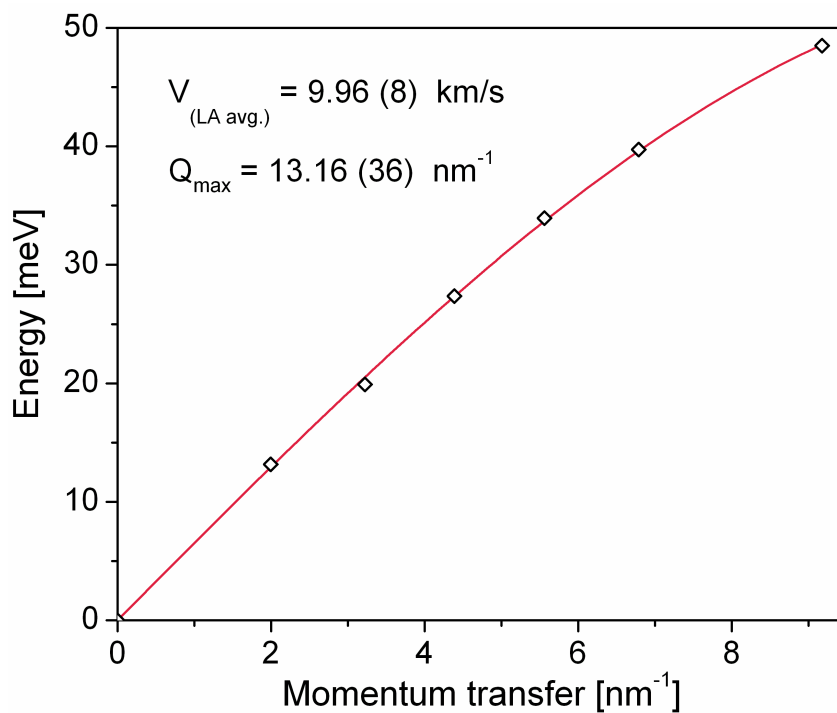


Figure 4.2: Sinusoidal fit (red line) to the IXS measurements on polycrystalline MgO at low momentum transfer (diamonds) and obtained average longitudinal sound velocity.

Experimental results

A summary of the three quantities K , v_D and v_P , required to extract the elastic tensor, is given below:

$$K = 162.5 \text{ GPa [55]}, \quad v_D = 6.63 \text{ (13) km/s [13]} \quad v_P = 9.96 \text{ (8) km/s}$$

Two different approaches were made to extract C_{11} , C_{12} and C_{44} : an approximative analytical and an accurate numerical approach. In the first procedure, the microscopic average longitudinal sound velocity v_P , measured in the experiment is approximated by the sound velocity along the [110] direction. This can be explained following the van Hove scheme, where special points in the velocity distribution lead to specific features in the scattering factor $g(Q, E)$ in the low momentum transfer region [39]. In cubic crystals at low Q , these special points are located on main symmetry direction with extrema along [100] and [111], and a saddle point along the [110] direction. The minima and the maxima induce vertical cut-offs on both sides of the frequency distribution function, while the saddle point causes a logarithmic peak [14]. The extracted average sound velocity corresponds therefore closely to the velocity along the [110] direction and v_P is given directly solving the Christoffel equation for the [110] direction ($\rho = 3.585 \text{ g/cm}^3$):

$$v_P = \sqrt{\frac{C_{11} + C_{12} + 2C_{44}}{2\rho}} \quad (4.2)$$

The relation between the bulk modulus K and the three elastic constants in an cubic system is given by equation 1.54. Furthermore, an analytic approximative formula of the Debye velocity is given by equation 1.62. The latter relation can be expressed as a function of C_{44} , K and v_P :

$$v_D = \left\{ \frac{1}{3} \left[\frac{1}{\left(\frac{1}{\rho} \left(K + \frac{4}{5} \cdot \alpha\right)\right)^{3/2}} + \frac{2}{\left(\frac{3}{5\rho} \cdot \alpha\right)^{3/2}} \right] \right\}^{-1/3} \quad (4.3)$$

where

$$\alpha = \frac{-9C_{44}^2 + C_{44}(\rho \cdot v_P^2 - K) + 9(\rho \cdot v_P^2 - K)^2}{9(\rho \cdot v_P^2 - K) - 7C_{44}}$$

For the accurate numerical approach, v_P is computed as the average of the longitudinal contribution of v_j in equation 1.47, while the Debye velocity v_D is formally obtained by averaging v_j in equation 1.47 over all directions. In order to compute the integral over the solid angle $d\Omega$, in the case of v_D the velocities v_j are calculated at 30×15 equidistant mesh points on 1/16 of the sphere surface. Furthermore, as before, K is expressed by equation 1.54.

The resulting values of the approximate analytical approach are compared to experimental values in table 4.1. The agreement with ultrasonic data [62] and Brillouin scattering [52] results is very good. The largest difference is 5.3% for C_{12} . The resulting values

	C_{11}	C_{12}	C_{44}
approximate analytical approach	286.5 (329)	100.5 (164)	162.1 (139)
accurate numerical approach	299.3	94.0	159.6
Ref. [52]	297.0 (1)	95.2 (7)	154.4 (5)
Ref. [62]	296.8 (2)	95.3 (2)	155.8 (2)

Table 4.1: Elastic constants for obtained from a polycrystalline sample compared to experimental data from a single crystal. The estimated errors for the accurate numerical approach are about 3 %.

for the accurate approach are presented in table 4.1 as well. One can remark a slight improvement in comparison to the experimental data obtained by Brillouin scattering [52]. The maximum deviation is 3.3% for C_{44} . Nevertheless, the difference between the two approaches is small enough that the simpler approach, using the approximate equations, is a valid method to reconstruct the elastic tensor for monoatomic and diatomic cubic systems.

4.2 Monoatomic hexagonal system

In the case of polycrystalline MgO only the elastic properties were considered. In order to obtain a complete picture of the lattice dynamics, beryllium was chosen as an initial test case to establish a method for the extraction of single crystal phonon dispersion from experimental data over a large momentum transfer range. The theoretical background of this methodology is described in chapter 2. The essential concept is to record IXS spectra over a large momentum transfer range, from the low momentum transfer to the vibrational density-of-states limit. The variation of peak positions and relative intensities in these spectra is then used to refine a model to the experimental data and thus to extract the single crystal dispersion.

4.2.1 Beryllium

Beryllium has been the subject of great interest in solid state physics because of its simple atomic configuration and remarkable bulk properties.

- Among the solid elements, it has the smallest unit cell volume, except for boron and carbon.
- Measured by the Young modulus, it is among the stiffest elements and about 50 % stiffer than iron.
- Among metals Be has the highest electron density.
- Due to the particular position of Be in the periodic table of elements, second row and second column, it has only two valence electrons per atom, and represents the simplest hcp metal.
- The high Debye temperature (1440 K) and a very small Poisson ratio of 0.05 suggest that the behavior of the valence electrons deviates substantially from that of nearly free electrons [63].

Under ambient conditions beryllium has a hexagonal closed packed hcp structure with two atoms per unit cell. Considering that the electronic configuration of the valence shell is closed ($2s^2$), the crystal of N atoms should have a completely filled valence band with N levels populated by $2N$ electrons and accordingly be an insulator. Be is, however, a conductor, indicating bonding via hybridisation, i. e. a mixing of the s and p orbitals in the crystal. Furthermore, Be has unusual bonding characteristics, since the partially occupied atomic hybrids are different according to the direction in the hexagonal cell. The atoms in one plane bond with sp^2 hybrids while two sp hybrids account for the bonding

along the c -axis. The sp hybrids bond stronger than the sp^2 orbitals [64], which gives on one hand rise to the smaller c/a ratio ($c/a = 1.568$) than the value of 1.633 for the ideal hexagonal closed packed structure, and on the other hand leads to a strong directional nature of the bonding.

The bonding between atoms in a solid determines the dispersion of vibrational modes. In beryllium, the anisotropic electronic screening (due to anisotropic hybridisation) of the ion motion results in noncentral forces and the system becomes non trivial. For example the shear elastic constants C_{44} and C_{66} exceed the bulk modulus K . This fails to occur in any other hexagonal element, for which on average, the shear modulus is about 40% of K .

Due to numerous studies of the beryllium lattice dynamics, the system is well understood. The dispersion along all main symmetry directions was determined by inelastic neutron scattering on a single crystal [65]. In addition Be has a very good inelastic x-ray scattering intensity and a quite simple unit cell. This system was therefore chosen to establish the method of extraction of the single crystal dispersion from polycrystalline materials.

4.2.2 Experiment

The sample was a compressed pellet of beryllium grains, of 15 mm diameter, corresponding roughly to one absorption length. Due to the large grain size it was necessary to rotate the sample with a frequency of about 10 Hz . The absence of texture was verified measuring the relative intensities of the three Bragg peaks (100), (002), (101) and comparing them to the powder spectrum. The IXS experiment was performed utilising the Si (9 9 9) backscattering configuration with an energy resolution of 3.0 meV . The X-rays were focused by a toroidal mirror into a spot size of to $250 \times 60 \mu m^2$ (horizontal x vertical, full-width-half-maximum). A total of 90 IXS spectra were recorded, spanning a momentum transfer region from 1.9 nm^{-1} to 79.5 nm^{-1} . We chose the exact angular positions to uniformly cover the achievable momentum transfer range and to avoid Bragg peaks. The resolution functions were experimentally determined from a poly(methylmethacrylate) (PMMA) sample, kept at 10 K and at $Q = 10 nm^{-1}$. Furthermore, relative efficiencies of the analysers were determined using the elastic scattering from a PMMA sample at the same angular position of the spectrometer as the ones used for the ensemble of IXS spectra.

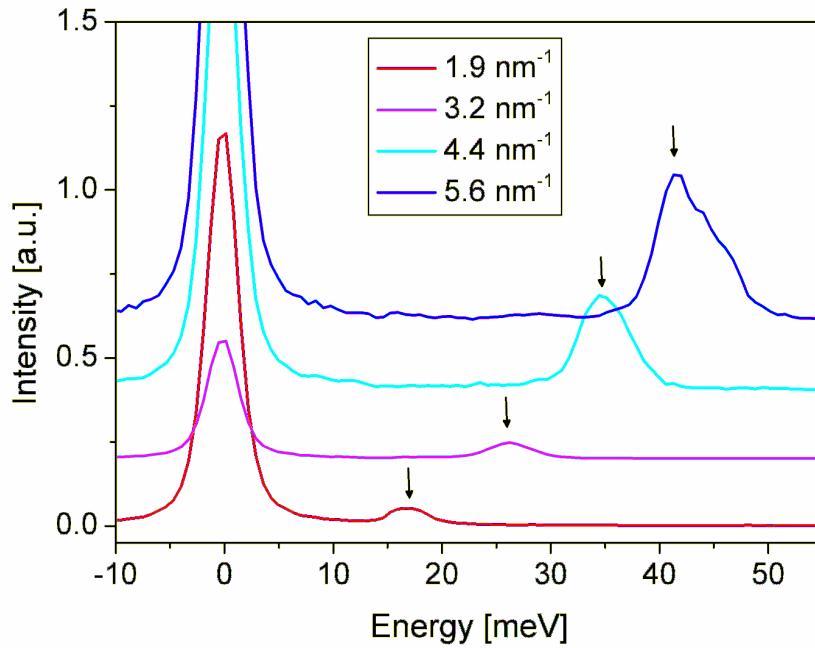


Figure 4.3: Stokes side of the IXS spectra of Be at different momentum transfers. The inelastic features due to longitudinal excitations are marked by arrows.

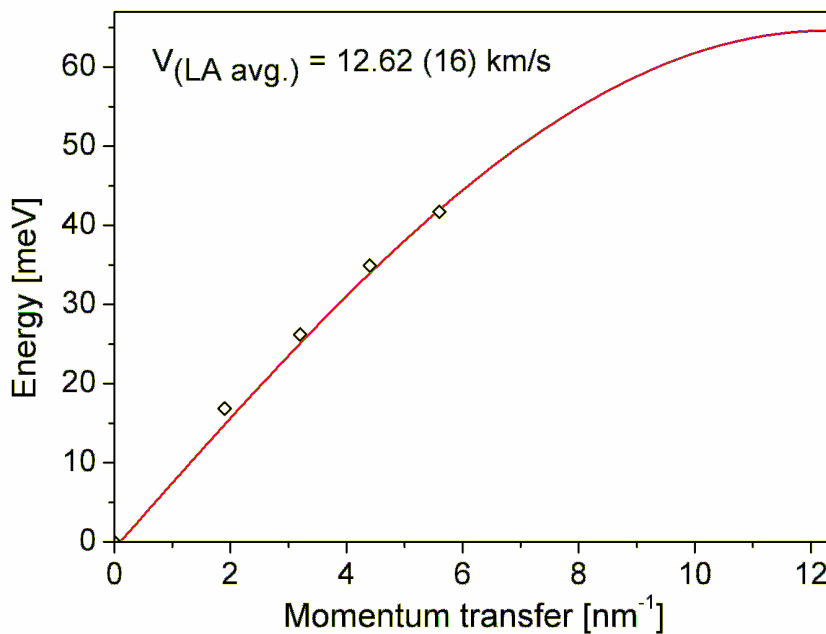


Figure 4.4: Low-Q LA phonon dispersion of polycrystalline Be (diamonds). The red line represents the best sinusoidal fit to the experimental data.

	sound velocity [km/s]
aggregate average (Hill) [66]	12.90
Fit (Q_{MAX} fix)	12.62 (16)

Table 4.2: Comparison of the obtained longitudinal acoustic sound velocity with resonant-ultrasound measurements. Errors are given as far as available.

4.2.3 Experimental results

The low momentum transfer limit

In the low momentum transfer region inelastic scattering from longitudinal phonons is dominant, and allows the extraction of the longitudinal sound velocity. The first four recorded spectra up to 5.6 nm^{-1} (Fig. 4.3) show only one inelastic peak. Though the next spectra up to about 12 nm^{-1} are still within the first Brillouin zone, a second inelastic peak appears. This is due to the anisotropy of hexagonal Be. The peak at lower energy transfer corresponds to longitudinal vibrations in the basal plane, while the peak at higher energy is due to longitudinal phonons along the c -direction. Thus, only the first four peak positions correctly represent the average longitudinal dispersion, and those were taken to determine the average longitudinal sound velocity v_L . The experimental dispersion is reported in Fig. 4.4, together with the result of the sine fit (see equation 1.42). The resulting sound speed depends on the choice of the value of Q_{MAX} . Here, we consider only data at very small momentum transfer, far away from the first BZ edge. Q_{MAX} was therefore fixed to a value, corresponding to the radius of a sphere with the same volume as the first Brillouin zone ($Q_{MAX} = 12.22 \text{ nm}^{-1}$). We note that the determined sound velocity is in excellent agreement with resonant-ultrasound spectroscopy measurements [66]. Both values are presented in table 4.2 and they agree within 2%.

The density-of-states limit

At high momentum transfer, in the range between 50 nm^{-1} and 80 nm^{-1} the summation of selected spectra (69.6 nm^{-1} , 70.9 nm^{-1} , 71.9 nm^{-1} , 72.9 nm^{-1} , 74.1 nm^{-1} , 75.2 nm^{-1} , 76.3 nm^{-1} , 77.4 nm^{-1} , 78.7 nm^{-1} , 79.5 nm^{-1}) allows the extraction of the vibrational density-of-states (VDOS) following the procedure described in section 1.2.1. The obtained experimental VDOS is compared to the theoretical VDOS in Fig. 4.5, which was convoluted with the experimental energy resolution of 3 meV . Two main peaks at 53 meV and 80 meV characterise the VDOS. The best agreement between experiment and theory is obtained for first principle calculations using density functional perturbation theory (Lazzeri *et al.* [67]). The calculation by Robert and Sollier [68], using pseudopotential calculations, overestimates slightly the energies of the highest optical peak. The VDOS

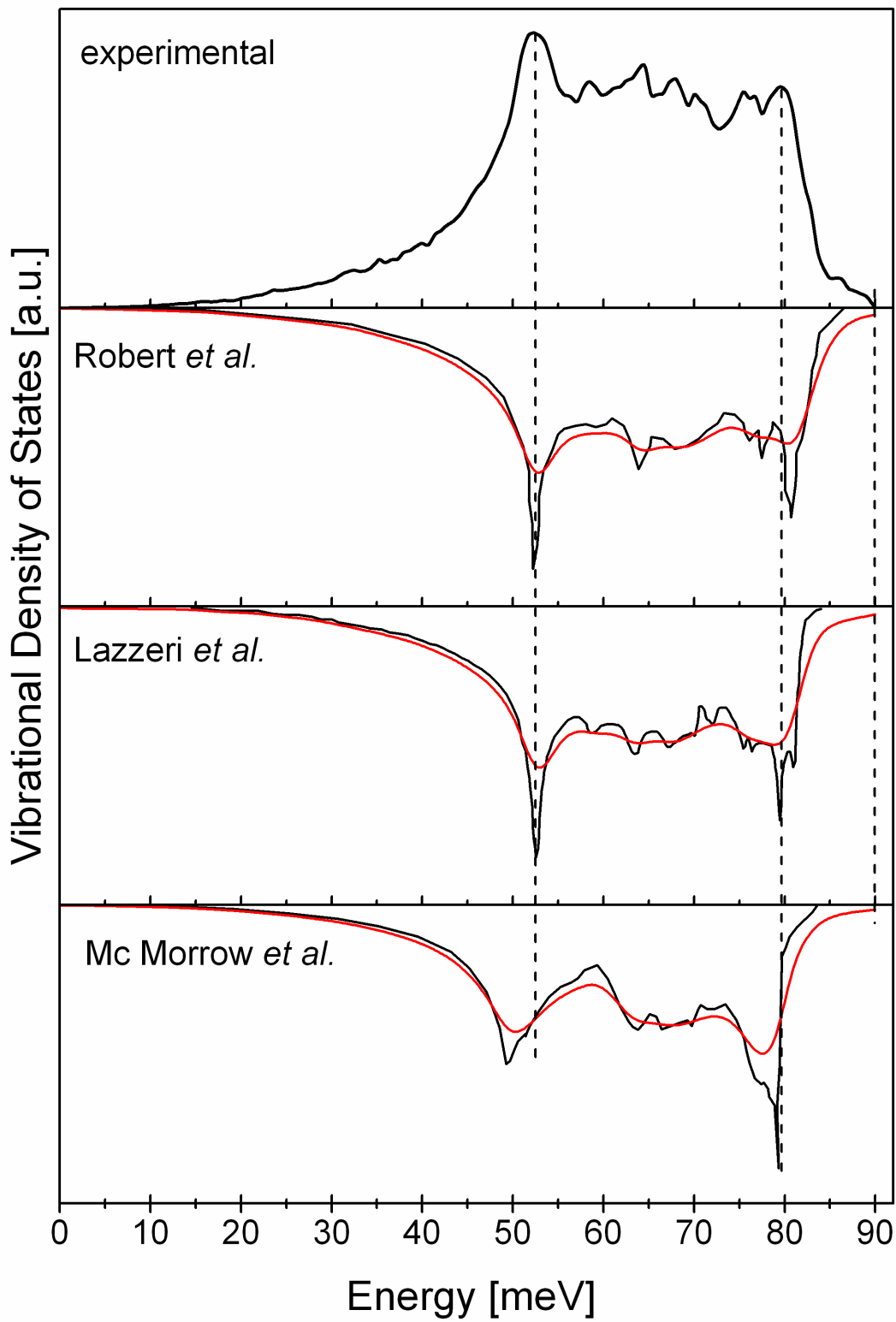


Figure 4.5: Experimental vibrational density of states for Be compared to theoretical calculations (black line) and convoluted with the experimental energy resolution (red line).

experimental Θ_D [K]	literature values Θ_D
1600 K	1475 K [68], 1466 K [70], 1485 (5) K [71]

Table 4.3: Debye temperature derived from X-VDOS, compared to literature values. Errors are indicated if available.

by Mc Morrow *et al.* [69], obtained via a Born - von Kármán fit to the experimental dispersion obtained by inelastic neutron scattering, shows the largest energy difference for the first peak in the VDOS and underestimates the energy of the highest optical branches. In addition, the intensity distribution shows differences. In contrast, all non - convoluted theoretical calculations underestimate the high energy cut-off. In the experimental VDOS the cut-off is located at around 90 *meV*, while the theoretical calculations show the cut-off at 85 *meV*. This is due to energy resolution effects (cut-off energy improves after convolution).

The knowledge of the DOS allows the evaluation of the Debye temperature Θ_D . The extracted value, derived from a parabolic fit to the low energy part of the VDOS is 1600 *K*. This value is compared in table 4.3 to Θ_D obtained from *ab initio* calculations [68], [70], and heat capacity measurements [71]. The agreement is within an error of 8.4 %.

The intermediate momentum transfer range

The complete experimental momentum transfer - energy intensity map is shown in Fig. 4.6. The experimental data are normalised to the incoming x-ray intensity, the polarisation of the beam, the analyser efficiencies and the atomic form factor. Furthermore, the elastic line was carefully subtracted using a Pseudo - Voigt fit. In the low Q - limit the dispersion of the averaged longitudinal dynamics is observable, while in the high Q - limit the VDOS is approached. In the intermediate momentum transfer range and lower energy region acoustic phonons form the arc structure. Optical vibrations compose the band in the higher energy range. The refined spectra are marked by a white line pointing out the fairly homogeneous distribution of the selected spectra over the entire momentum transfer range. As already mentioned earlier, the information content obtained in the high and low Q limit is not sufficient to fully determine the single crystal phonon dispersion. We use the variation in peak positions and relative intensities of the IXS spectra in the intermediate momentum transfer range to complete the picture of the dynamics of the system following the method developed in chapter 2.

The number of spectra used to the fitting procedure is limited by the computing time. Preliminary tests revealed that about one spectrum for three parameters should be fitted. Thus ten experimental spectra (for $Q = 3.2 \text{ nm}^{-1}$, 8.0 nm^{-1} , 14.4 nm^{-1} , 19.3 nm^{-1} , 22.9 nm^{-1} , 42.8 nm^{-1} , 52.2 nm^{-1} , 62.6 nm^{-1} , 69.4 nm^{-1} , 78.5 nm^{-1}) were selected for the

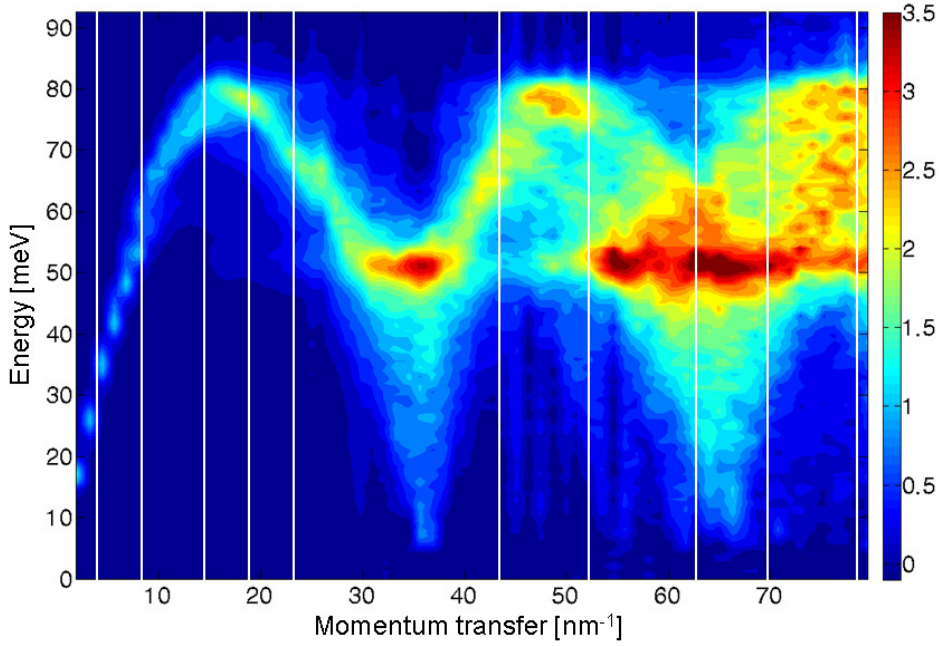


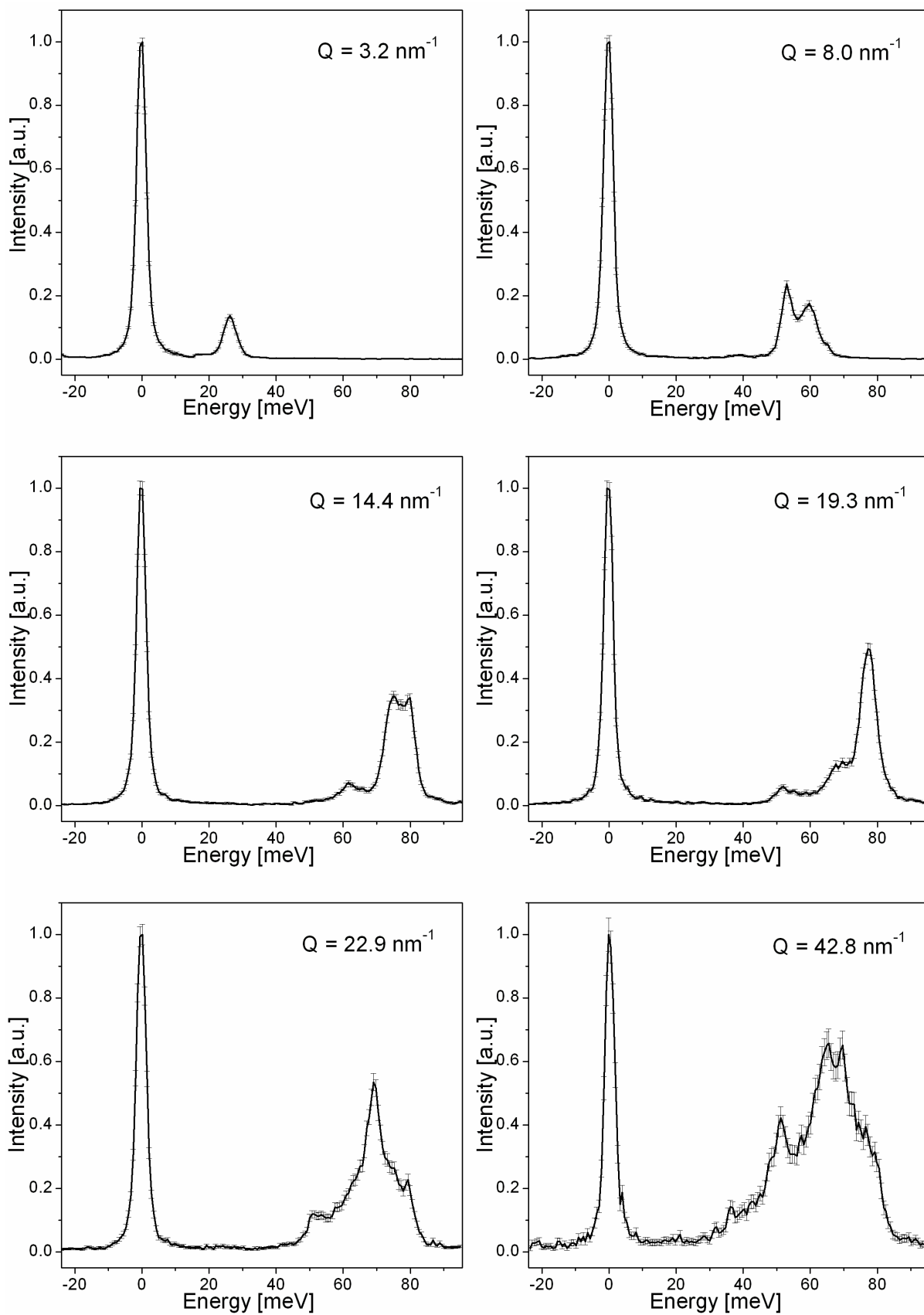
Figure 4.6: Experimental IXS intensity map of Be, composed of constant momentum transfer scans. The spectra are normalised and the elastic line is subtracted. The white lines indicate the ten selected spectra for the fitting routine.

refinement procedure. The spectra show a development of their overall shape and distinct peak positions as can be appreciated in Fig. 4.7. In this illustration the spectra are normalised to the maximum intensity and to the incoming intensity. The experimental error bars are given as well. At zero energy transfer the elastically scattered intensity is visible. The development of the inelastic features from low momentum transfer to high momentum transfer is clearly observable.

A Born - von Kármán lattice dynamics model was refined to the ten spectra, using the beryllium hexagonal unit cell with $a = 2.2858 \text{ \AA}$, and $c = 3.5843 \text{ \AA}$ and two atoms at $(0, 0, 0)$ and $(1/3, 2/3, 0.5)$ (see Fig. 4.8). The definition of the coordinate system and the force constant matrices for an atom at a given position are shown in table 4.4. In the Born - von Kármán model we have to include up to the 7th nearest neighbours (NN) due to the non-central forces in beryllium. As a consequence 29 parameters need to be refined. We use as starting parameter the set of force constants published in [72] (see table 4.6), which were obtained from a least squares fit of a Born - von Kármán model to the experimental INS dispersion [65].

For the computation of the polycrystalline IXS cross section we only need to average over $1/24$ of the spherical shell surface, thanks to the hexagonal symmetry. The scattering

4.2 Monoatomic hexagonal system



Experimental results

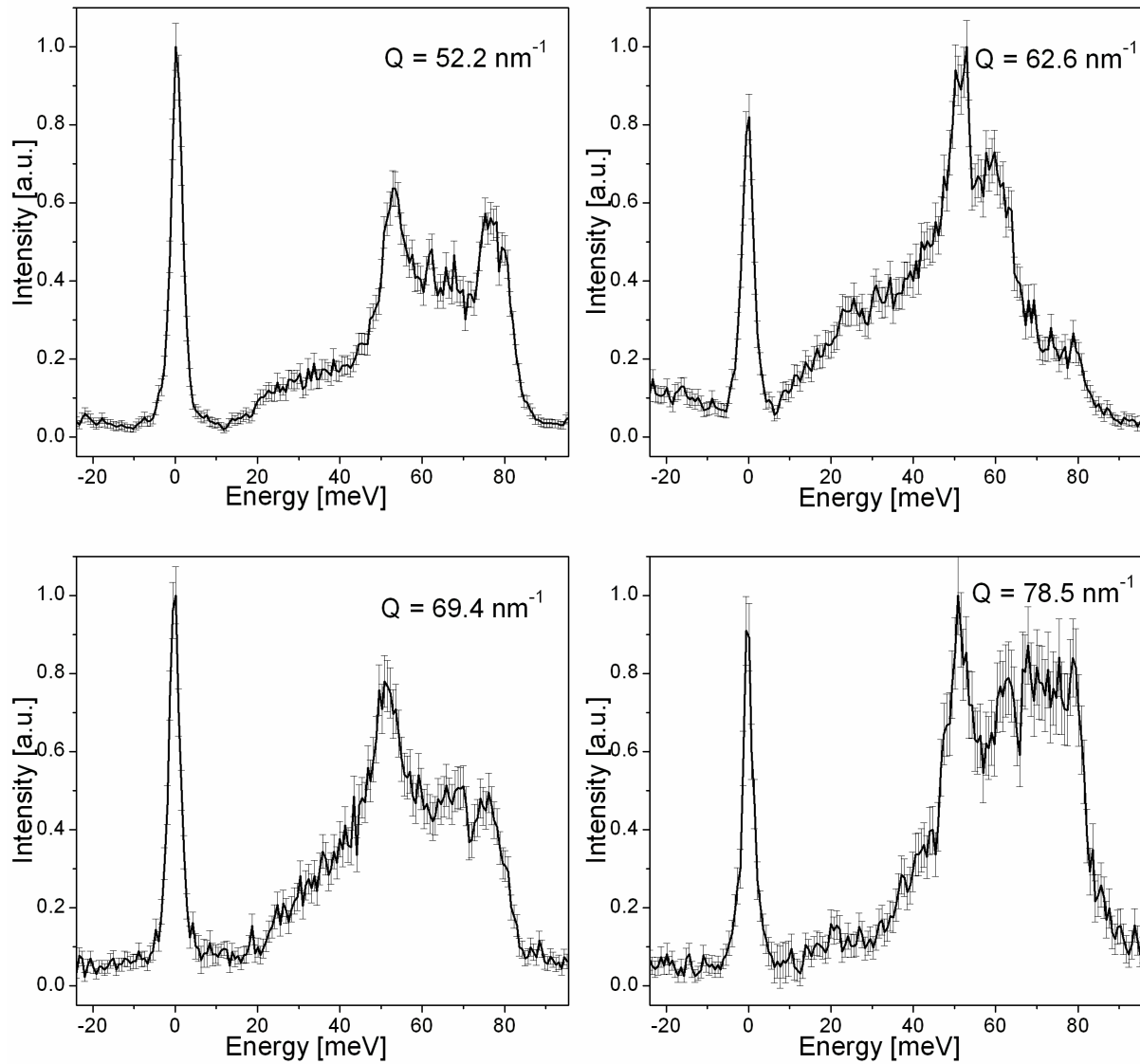


Figure 4.7: Experimental IXS spectra selected for the fit. The intensity is normalised and the experimental error bars are shown.

4.2 Monoatomic hexagonal system

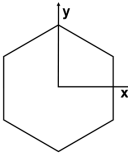
Nearest neighbour (NN)	Cartesian coordinates of NN	Interaction matrix
	$\hat{r}_{n,m} = (x, y, z)$	$\Phi(n, m) = \begin{bmatrix} n_x m_x & n_x m_y & n_x m_z \\ n_y m_x & n_y m_y & n_y m_z \\ n_z m_x & n_z m_y & n_z m_z \end{bmatrix}$
1 NN	$(a/\sqrt{3}, 0, -c/2)$	$\begin{bmatrix} \alpha_1 & \delta_1 \\ & \beta_1 \\ \delta_1 & \gamma_1 \end{bmatrix}$
2 NN	$(0, a, 0)$	$\begin{bmatrix} \alpha_2 & \delta_2 \\ -\delta_2 & \beta_2 \\ & \gamma_2 \end{bmatrix}$
3 NN	$(-2/\sqrt{3} \cdot a, 0, -c/2)$	$\begin{bmatrix} \alpha_3 & \delta_3 \\ & \beta_3 \\ \delta_3 & \gamma_3 \end{bmatrix}$
4 NN	$(0, 0, -c)$	$\begin{bmatrix} \alpha_4 & & \\ & \alpha_4 & \\ & & \beta_4 \end{bmatrix}$
5 NN	$(-2/\sqrt{3} \cdot a, a, c/2)$	$\begin{bmatrix} \alpha_5 & \varepsilon_5 & \delta_5 \\ \varepsilon_5 & \beta_5 & \lambda_5 \\ \delta_5 & \lambda_5 & \gamma_5 \end{bmatrix}$
6 NN	$(\sqrt{3} \cdot a, 0, 0)$	$\begin{bmatrix} \alpha_6 & & \\ & \beta_6 & \\ & & \gamma_6 \end{bmatrix}$
7 NN	$(0, a, c)$	$\begin{bmatrix} \alpha_7 & -\varepsilon_7 & -\delta_7 \\ \varepsilon_7 & \beta_7 & \lambda_7 \\ \delta_7 & \lambda_7 & \gamma_7 \end{bmatrix}$

Table 4.4: Definition of the coordinate system, with the z-axis parallel to the c axis of the hcp crystal structure, perpendicular to the drawing plane.

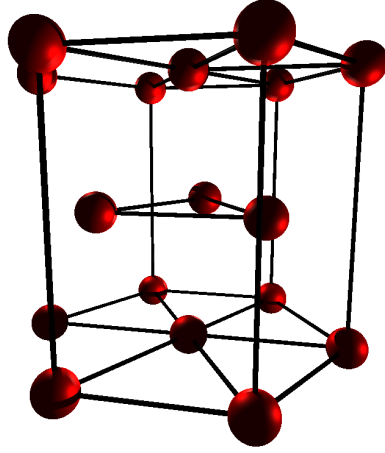


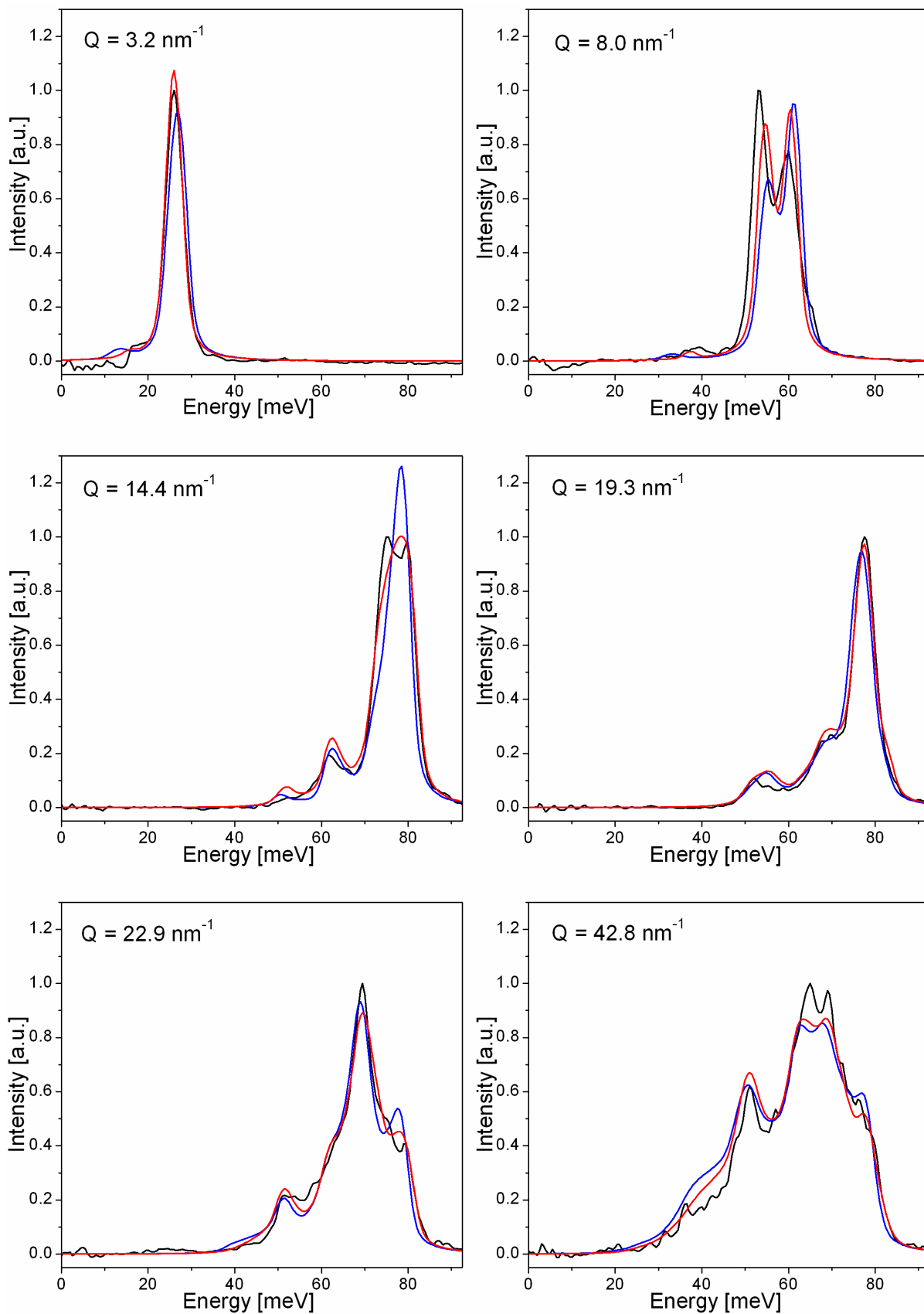
Figure 4.8: Hexagonal crystal lattice of beryllium.

intensity is calculated for a mesh of 43200 points on this surface. These are chosen not to be on high symmetry directions, in order to avoid eventual instabilities in the calculation of the phonon eigenvectors. A weighting of the obtained intensities with a sine function is carried out as described in section 2.2.3.

The merit function, measuring the agreement between experimental data and model calculations during the fitting routine, decreased by 2.4 from $\chi_{start}^2 = 3.73$ to $\chi_{end}^2 = 1.55$, during 12 iterations (duration of one iteration about 6 hours). The refined force constants are given in table 4.6. In Figure 4.9 the ten refined spectra (red lines) are compared to the experimental data (black lines). The experimental spectra were prepared by fitting the elastic line with a Pseudo-Voigt function and subtracting it carefully. They are also normalised as aforementioned by considering the incoming x-ray intensity, the polarisation of the beam, the analyser efficiencies and the atomic form factor. Furthermore the spectra, calculated with the starting parameters are given (blue lines), which show already a very good agreement with the experimental data. At low momentum transfer (3.2 nm^{-1} , 8.0 nm^{-1}) the peak positions are improved. In the intermediate Q region (19.3 nm^{-1} - 42.8 nm^{-1}) the fitted spectra show an excellent agreement with the experimental spectra. The positions of the cut-offs at low energy transfer for high momentum transfer are improved. While all important peaks and peak positions are present, differences in the relative intensities can be observed. Nevertheless the overall agreement improved compared to the starting model, and can be considered as very good.

The momentum transfer-energy intensity map computed with the refined set of force constants, is displayed in Fig. 4.10 for the same E and Q range as the experimental data (Fig. 4.6). Furthermore, in order to simplify the comparison of the experimental result and the calculation, the difference between these two maps is computed: the experimental

4.2 Monoatomic hexagonal system



Experimental results

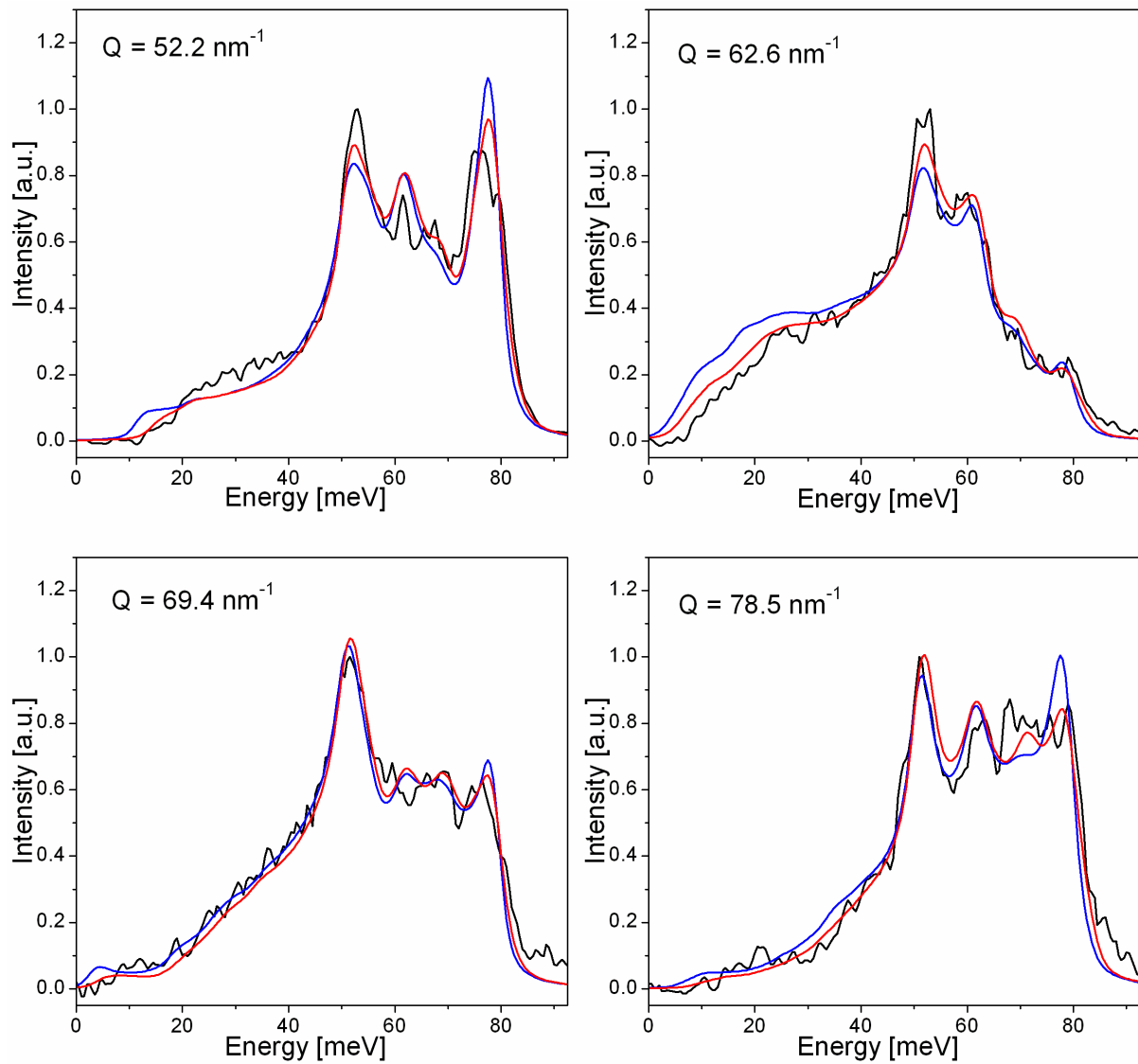


Figure 4.9: Polycrystalline IXS spectra: experiment (black lines), starting model spectra (blue lines), and refined model spectra (red lines).

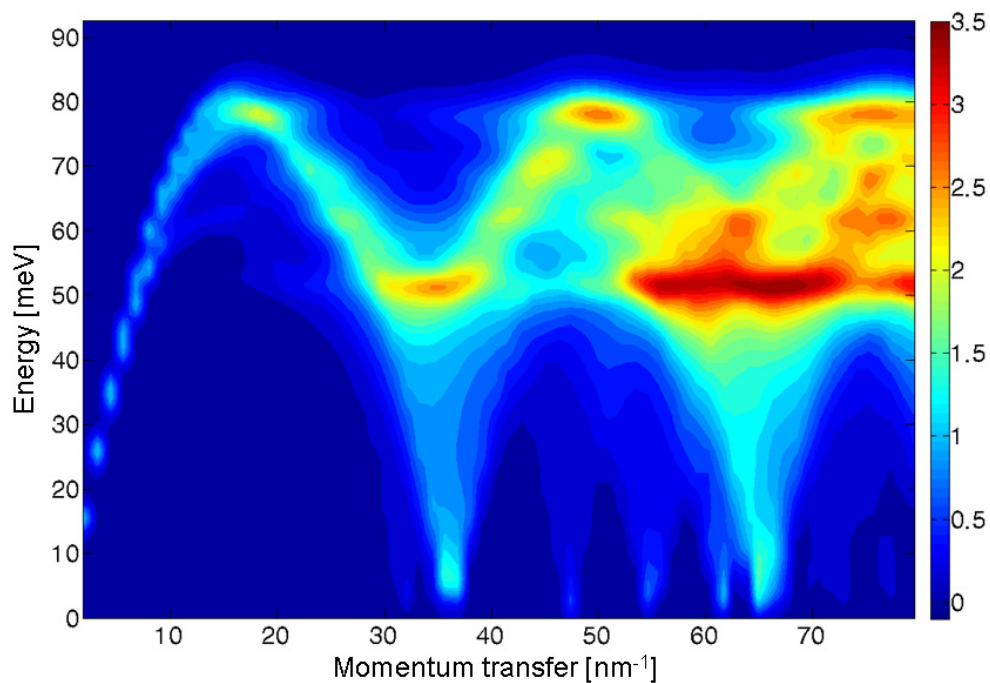


Figure 4.10: Momentum transfer - energy transfer map of the refined model calculation for beryllium.

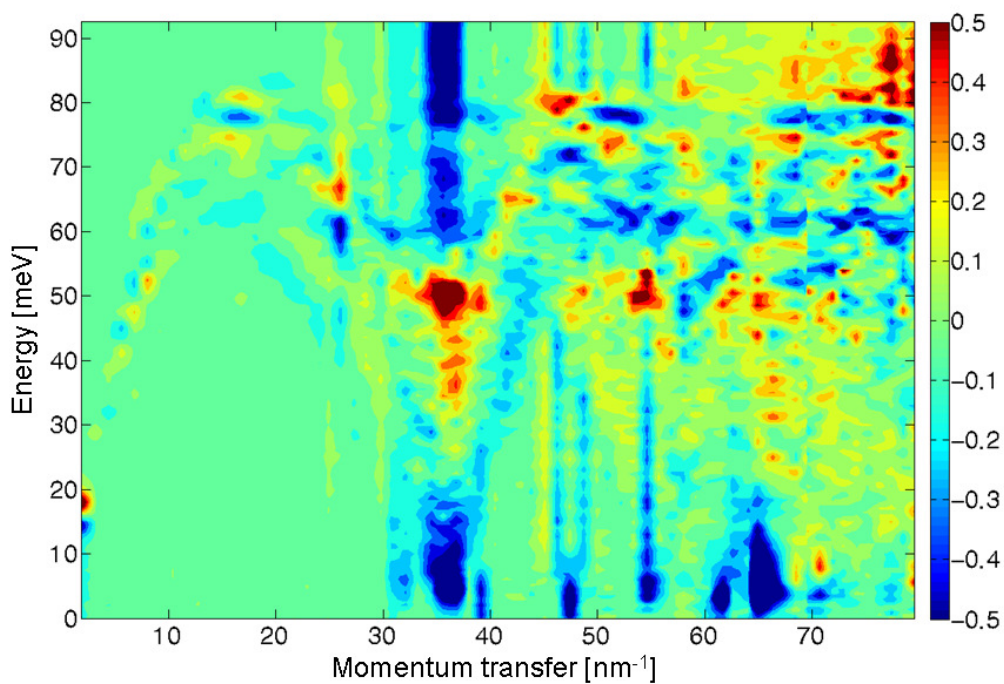


Figure 4.11: Difference map between the experimental data and the refined model for Be.

Experimental results

spectra are scaled to the calculated spectra and then the calculated map is subtracted from the experimental map (see Fig. 4.11). Altogether, the calculated and the experimental map show an excellent agreement. To note is the very good analogy of the pattern and the intensity distribution in the acoustic part. The main differences occur at around 35 nm^{-1} momentum transfer. This can be explained by the neighbourhood of a strong Bragg peak, which gives rise to a strong elastic line, thus rendering the correct extraction of inelastic contributions at low energy transfer difficult. Furthermore, differences in the intensities can be observed in the higher energy region. This is due to the fact that the shape of the optic part in the IXS spectra is more sensitive to the choice of the number of neighbours and the set of force constants, illustrating the limitation of the Born – von Kármán model in this very anisotropic system.

The dispersion relation

Up to now the model calculations were refined to the experimental data obtained from a polycrystalline sample. As a cross - check of the validity of the process the refined model needs to be compared to the single crystal dispersion, determined by inelastic neutron scattering at a temperature of 80 K [65]. Figure 4.12 confronts the dispersion calculated from the refined force constants (red line) with the experimental one (black dots) and the starting model (blue line). The excellent overall agreement confirms the results obtained for the polycrystalline system. Differences can be observed in the optical branches. This was already discussed above in the comparison of the experimental and calculated energy - momentum transfer map (see Fig. 4.11) for the polycrystalline system. The dispersions, obtained with the starting model and the refined model do not show striking differences. Nevertheless, one has to stress, that the refined dispersion has been obtained from a fit to the polycrystalline IXS spectra, therefore including all crystallographic directions and not only high symmetry ones.

Elastic properties

The elasticity tensor of beryllium has five independent components C_{11} , C_{33} , C_{44} , C_{66} , and C_{13} . Section.1.1.2 describes how these elastic constants can be deduced from the slope of acoustic branches close to the Γ - point for hexagonal symmetry via the Christoffel equation, providing a relation between the phase velocity, the elastic moduli and the density.

Extracting the elastic constants from the refined model calculation yield values which are quite different from reported literature values [74], [73], especially for C_{66} and C_{13} (see table 4.5). This discrepancy arises due to the highly anisotropic forces in beryllium and the consequent difficulty to obtain a good Born - von Kármán fit. In order to improve

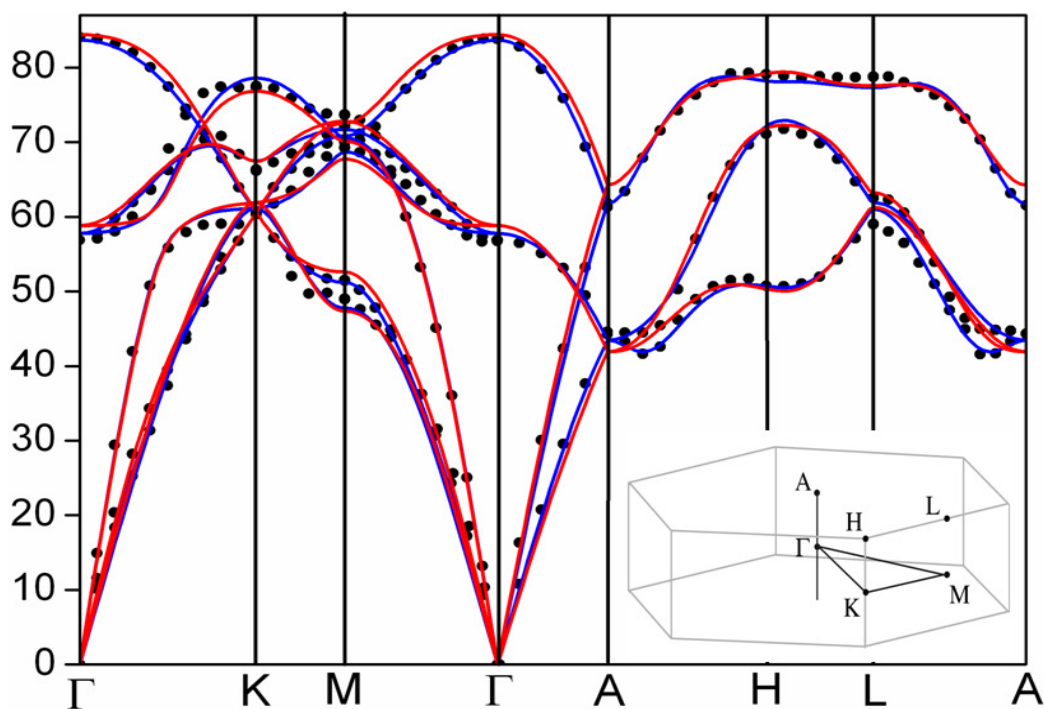


Figure 4.12: Dispersion relation for beryllium: experimental INS data (black dots) [65], starting model (blue line), and refined model calculation (red line).

	C_{11}	C_{33}	C_{44}	C_{66}	C_{13}
refined disp.	268.8	321.5	122.3	96.7	96.7
refined disp. (with K and C_{44})	255.9	343.5	156.1	93.7	3.57
model dispersion [72]	273.1	282.5	144.5	86.2	141.3
Robert and Sollier [68], theory	305.9	329	159.3	143.6	10.4
Migliori <i>et al.</i> [66], exp.	293.6 (18)	356.7 (21)	162.2 (3)	133.4 (16)	14.0 (11)
Rowland and White [73], exp.	288.8 (25)	354.2 (25)	154.9 (25)	134.4 (30)	4.7 (5)
Smith and Arbogast [74], exp.	292.3	336.4	162.5	132.8	14.0

Table 4.5: Elastic constants of beryllium in GPa at 300 K. Errors are given as far as available.

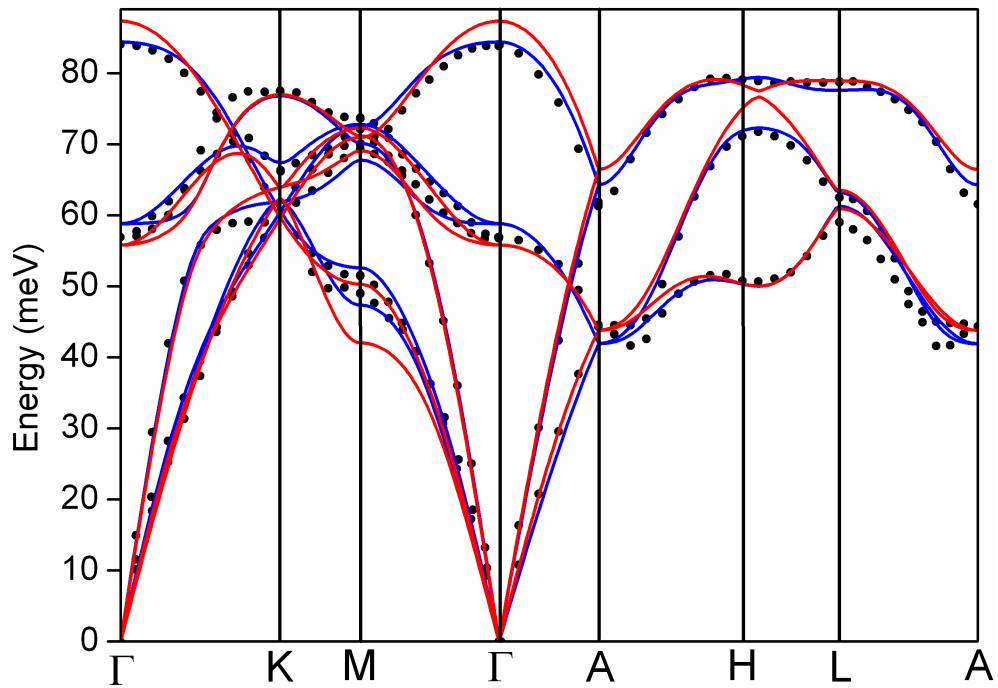


Figure 4.13: Dispersion relation for beryllium: experimental INS data (black dots), refined model without constraints (blue line), and constrained refined model calculation (red line).

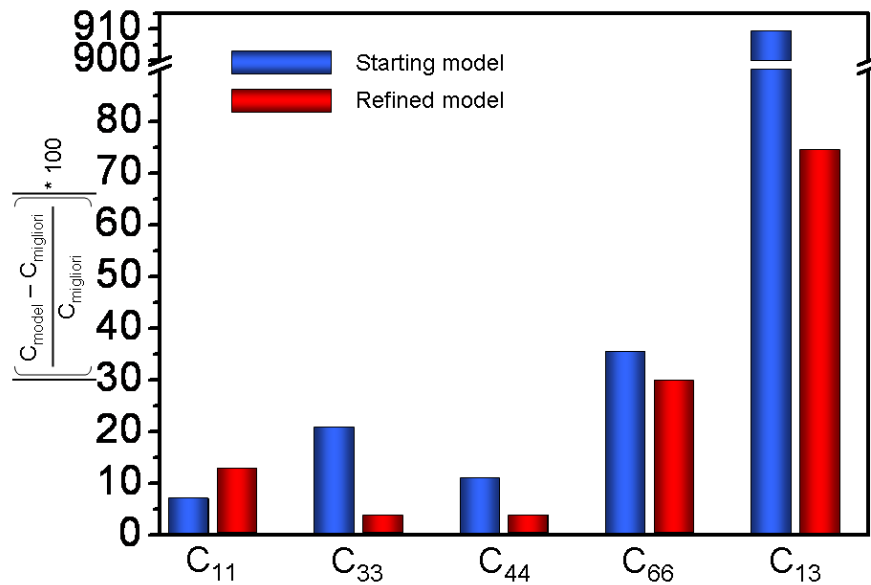


Figure 4.14: Comparison of the elastic constants extracted from the model calculation before and after the refinement to experimental resonant ultrasound spectroscopy data.

the fit of the acoustic part of the dispersion, the bulk modulus K and the elastic constant C_{44} are introduced as additional experimental values. The choice of these two parameters is motivated by the fact that they can be obtained as well from polycrystalline data via x-ray diffraction and Raman scattering, respectively. Phenomenological modeling shows that the Raman - active mode can be approximately correlated with the transverse acoustic phonon, directly linked to C_{44} [75]. Both are weighted in a way that each has the same importance as one of the ten IXS spectra. This imposes a serious constraint to the refinement procedure, which forces the result to be close to these two fixed quantities. We used $K = 116.8 \text{ GPa}$ and $C_{44} = 162.2 \text{ GPa}$ [66], which were determined by resonant - ultrasound spectroscopy on single crystal beryllium. The refined dispersion is shown in Fig. 4.13. The agreement for the linear part of the slope of the acoustic branches is improved, while the agreement of the optical part is, as expected, inferior with respect to the refinement without additional constraints. Nevertheless, the overall agreement is still very good. The resulting elastic constants (for $\rho_{Be} = 1.848 \text{ g/cm}^3$) are presented as well in table 4.5, together with the most recently published experimental values obtained by Migliori *et al.* [66] using resonant ultrasound spectroscopy. Furthermore the most recent theoretical values obtained by first principle calculations are given as well [68]. The deviation in percent of the elastic constants obtained from the starting and refined model is presented in Fig. 4.14. One can appreciate that all IXS derived elastic constants improved with respect to the starting model except C_{11} . The remaining large discrepancy for C_{13} can be explained as follows. C_{13} cannot be directly determined by a measurement along one of the high symmetry directions of the crystal. It needs to be derived by measurements at an angle α between the a - and the c - axis, and in any case involves the knowledge of the other four independent elastic moduli. It is therefore not surprising that reported experimental values differ quite substantially. For example the experimental value, published by Rowland and White [73], obtained by an ultrasonic experiment is $C_{13} = 4.7 \pm 0.5 \text{ GPa}$. Thus, our extracted C_{13} is within the experimental error bars in this specific case. In general, the obtained elastic constants are in good agreement with single crystal experiments, keeping in mind that these single crystal properties are extracted from experimental data of a polycrystalline material.

Error estimation

The used least squares fitting procedure allows to estimate the errors of fitted force constants in the case of normally distributed measurements errors and a model, which is linear in its parameters. The inverse of the second derivative matrix \mathbf{D} (Hessian matrix)

$$D_{kl} = \frac{\partial^2 \chi^2}{\partial a_k \partial a_l}$$

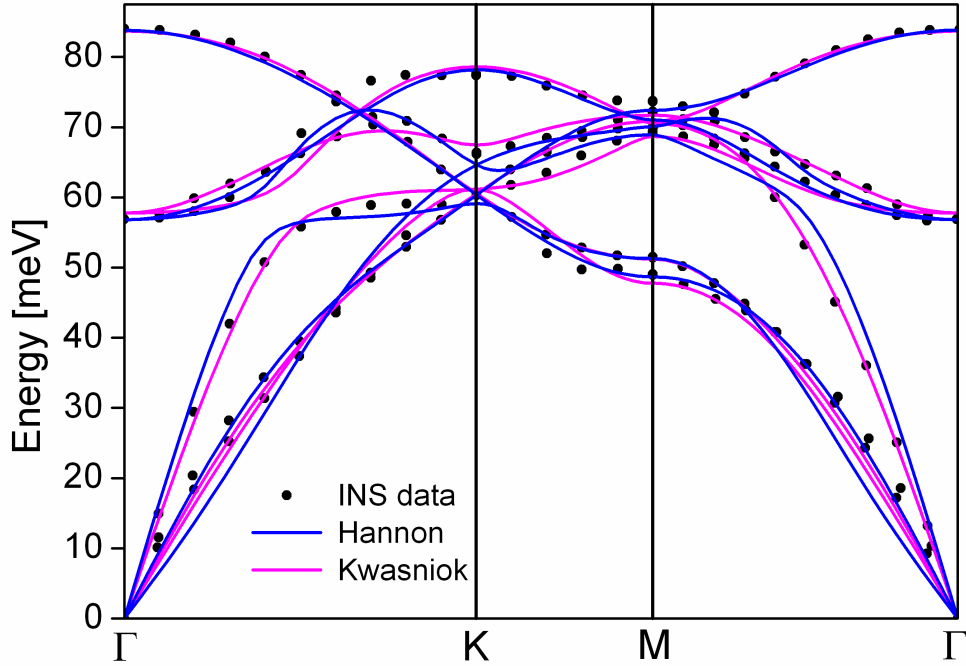


Figure 4.15: Dispersion relation for Be along the high symmetry directions: INS data (black points), calculation by Hannon *et al.* (blue line) and by Kwasniok (pink line).

in equation [?] is closely related to standard uncertainties of the estimated parameters \vec{a} . Thus, the diagonal elements of the so called covariance matrix \mathbf{C}

$$[C] = [1/2\mathbf{D}]^{-1}$$

are the variances of the fitted parameters \vec{a} , while the off-diagonal elements C_{kl} are the covariances between a_k and a_l . Since the force constants in a Born - von Kármán model are strong correlated, one cannot use the covariance matrix to give a confidence level of the fitted parameters. Therefore, one has to carry out a Monte Carlo simulation or a detailed analytic calculation to estimate the errors in the force constants. Due to the high complexity of this problem, the errors for the force constants are commonly not specified. As a consequence, the error bars for the elastic constants are not indicated either.

4.2.4 Comparison of different lattice dynamic models

The refinement of the lattice dynamics model of beryllium, as shown above, is quite computation time intensive due to the large number of force constants. Nevertheless, the fitting process is possible because of the large information content in the inelastic spectra.

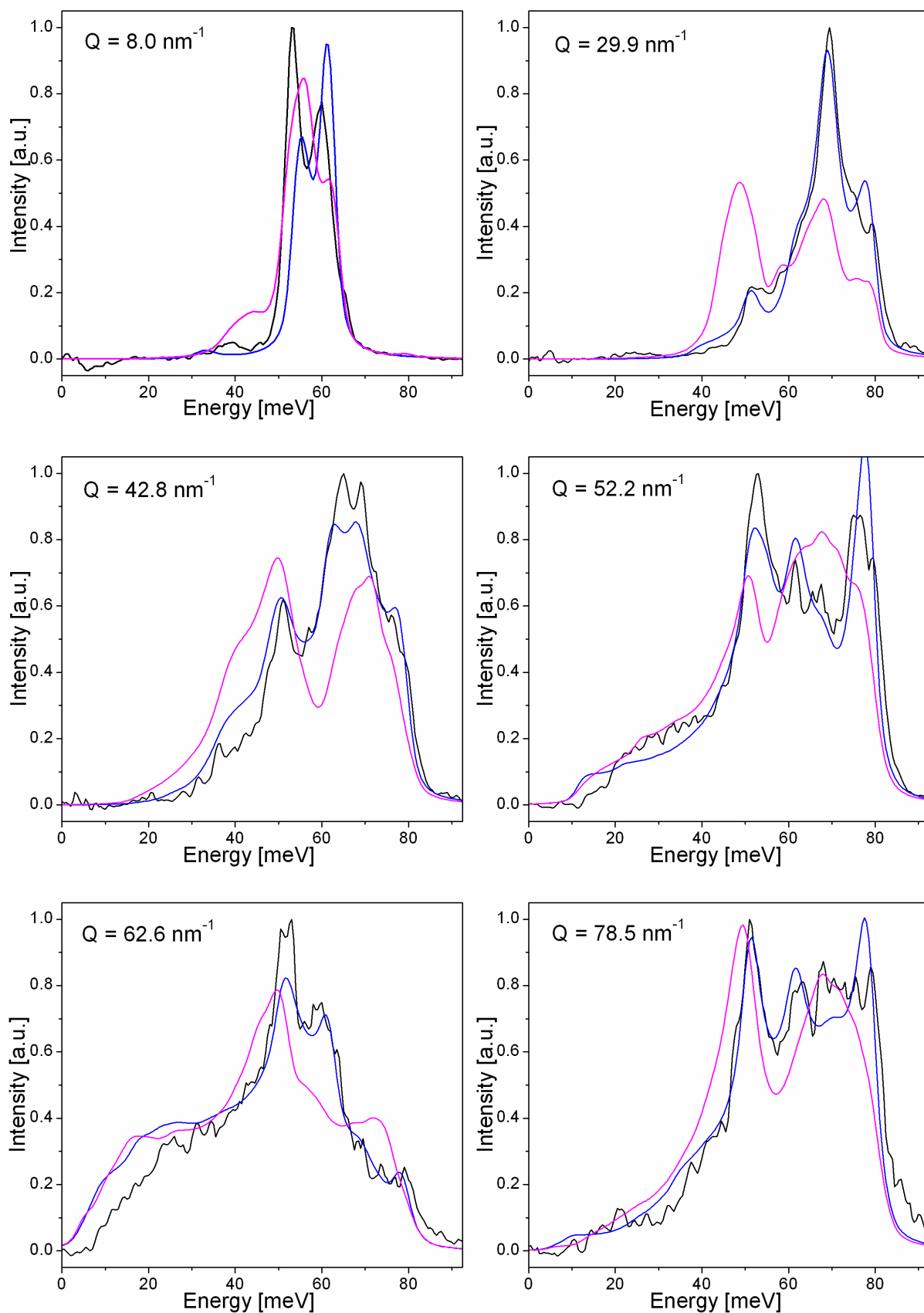


Figure 4.16: IXS spectra from polycrystalline Be (black line) compared to model calculations using force constants published by Hannon et al. (blue line) and by Kwasniok (pink line).

Experimental results

This is not always the case, and for complex systems (in terms of atoms per unit cell) the refinement procedure is expected to reach its limits. A more detailed discussion can be found in chapter 5. Another fast and elegant application, which is even possible beyond the limitations of the refinement process, is the comparison of theoretical calculations with the inelastic scattering spectra from polycrystalline materials. If a material can only be obtained in polycrystalline form, no experimental data of the dispersion relation are available. The knowledge of the dynamical properties is mostly based on theoretical calculations. Even if nowadays highly developed theoretical models are available, different calculations show variations in the results. In this case, polycrystalline IXS spectra can provide a powerful tool to distinguish between different calculations, and identify the most correct one.

In the case of beryllium two different results can be found in literature, published in 1995 by Kwasniok [76] and in 1996 by Hannon *et al.* [72]. In both publications a least squares fitting routine was performed, refining a Born - von Kármán model to the experimental dispersion relation, obtained by inelastic neutron scattering [65]. Kwasniok utilised 33 parameters including up to the 8 nearest neighbours, while Hannon *et al.* refine 29 parameters considering 7 nearest neighbours. In table 4.6 the resulting force constants, transformed into the same coordinate system, are given. It can be noted, that already the nearest neighbour interactions are significantly different. Nevertheless, the two calculations show a good agreement with the experimental data for the main symmetry directions of the dispersion relation (see Fig. 4.15). This is due to the fact, that variations of the force constants in one shell can be compensated by other force constants for different nearest neighbour shells. Figure 4.16 shows six representative polycrystalline IXS spectra, computed for both models, and confronted to the experimental results. Obvious discrepancies in peak positions and intensities occur for the model of Kwasniok in all spectra, but particularly in the intermediate momentum transfer range. On the contrary, the calculation of Hannon *et al.* reproduce the spectra quite well throughout the whole Q-region. In order to explain this striking observation, one has to consider that in the INS dispersion only main symmetry directions are taken into account. These directions are commonly measured in single crystal experiments since experiments along more (non-high symmetry directions) are time demanding. The calculation of the polycrystalline IXS spectra demands the averaging over a surface in reciprocal space thus considering also non - high symmetry directions. The additional information from non - high symmetry directions allows making the appropriate choice between different models.

4.2 Monoatomic hexagonal system

	α_1	β_1	γ_1	δ_1	α_2	β_2	γ_2	δ_2	α_3
Refinement	-11.55	-4.56	-20.16	11.75	-3.08	-19.12	-0.95	-7.44	-1.06
Constrained refinement	-13.20	-2.47	-20.62	12.85	-2.94	-19.23	-0.37	-5.48	-0.30
Hannon [72]	-11.93	-3.98	-19.59	13.33	-3.15	-19.14	-1.29	-6.92	-1.56
Kwasniok [76]	1.75	-10.04	-19.34	-2.90	-1.45	-22.42	0.86	-2.08	-7.79

	β_3	γ_3	δ_3	α_4	β_4	α_5	β_5	γ_5	δ_5	ϵ_5
Refinement	1.96	0.25	3.49	-1.41	-6.49	-1.55	-0.80	-0.28	1.59	0.41
Constrained refinement	2.64	-0.08	2.31	-2.57	-9.21	-1.52	-0.76	-0.61	1.73	0.34
Hannon [72]	2.35	0.13	4.45	-2.2	-4.67	-1.48	-0.55	-0.327	2.15	0.46
Kwasniok [76]	-1.71	1.14	10.94	1.39	-5.4	-0.36	-0.02	-0.99	-1.09	2.59

	λ_5	α_6	β_6	γ_6	α_7	β_7	γ_7	δ_7	ϵ_7	λ_7
Refinement	-0.09	-1.48	1.08	-1.53	0.47	-0.83	0.27	1.05	-1.41	0.06
Constrained refinement	0.18	-0.93	0.61	-0.85	0.27	-0.44	0.67	0.65	-1.93	0.34
Hannon [72]	-0.14	-1.76	1.34	-0.75	0.19	-0.09	0.33	1.12	-0.77	-0.5
Kwasniok [76]	0.83	-4.01	2.58	-0.77	-1.0	1.92	-0.68	-1.70	0.0	1.86

Table 4.6: Force constants for beryllium, after refinement (first row), constrained refinement with strong weight on K and C_{44} (second row), and published Born - von Karman fits to single crystal INS data (3. and 4. row).

4.3 Monoatomic hexagonal system with texture

A perfect powder sample was studied in the case of beryllium, and consequently, the next step is the investigation of a textured system. Pyrolytic graphite was chosen, since it is a strongly textured hexagonal system and significant deviations of the inelastic scattering intensity from the homogeneous polycrystalline system can be observed. Thereby, the consideration of texture in the model calculation is of importance. Otherwise the same data treatment procedure as for beryllium is applied, extracting the single crystal dispersion and the elastic tensor.

4.3.1 Pyrolytic graphite

The discovery of Novoselov *et al.* [77] of a simple method to transfer a single atomic layer of graphite to a substrate suitable for the measurement of its electrical and optical properties has revived the interest in the fundamental physical properties of graphite sheets (graphene). Moreover, an enormous amount of work has been done on the vibrational spectroscopy of carbon nanotubes, which can be regarded as one or more rolled up sheets of graphene. Since the vibrational properties of graphene and carbon nanotubes are closely related to those of graphite, the theoretical and experimental results on graphite are important to researchers working on these systems.

The forces in the hexagonal system graphite are extremely anisotropic. The strength of the sp^2 covalent interatomic bonding in the layer is comparable to the exceptionally strong forces existing in diamond, while the weak van - der - Waals bonding between adjacent basal planes is about two orders of magnitude smaller. Due to the completely different types of bonding, graphite presents a major challenge for theoretical calculations, and thus these contradict each other qualitatively and quantitatively in frequencies, slopes and crossings of particular phonon branches [78]. Due to the difficulty to grow large single crystals, INS has been applied only to pyrolytic graphite samples, consisting of very thin graphite crystallites, whose crystalline a-axis is randomly orientated around a common, well aligned c-axis. Consequently, only a part of the phonon dispersion relation - the longitudinal modes propagating along the [001] direction - could be studied unambiguously by inelastic neutron scattering [79]. Energy electron loss spectroscopy (EELS) on graphite or thin graphite films has probed the high symmetry directions $\Gamma - K$ and $\Gamma - M$ [80], [81], [82]. Recently, Maultzsch *et al.* [83] have presented very accurate measurements of the optical phonon modes along the directions $\Gamma - M$ and $\Gamma - K - M$ using IXS. This technique allows, due to very small beam size, the selection of a microcrystal in a naturally grown graphite flake and single crystal investigation along all high symmetry directions. The results were completed by Mohr *et al.* [84], providing the full in-plane

phonon dispersion of graphite, including the optical and acoustic branches, as well as the midfrequency range between the K and M points in the Brillouin zone. An overview of theoretical and experimental results is given by Wirtz and Rubio [78].

Experiment

The pyrolytic graphite sample of 8 mm diameter (corresponding roughly to one absorption length), was rotated with a frequency of about 10 Hz around an axis, perpendicular to the crystallographic c-axis and the horizontal scattering plane. This configuration was chosen to induce a simple texture, which is described in section 4.3.2.

In the IXS experiment the same instrumental setup was used as in the case for beryllium (see section 4.2.2). Altogether 70 experimental IXS spectra were recorded for the energy loss side including the elastic line, centered at zero energy transfer, in the momentum transfer range from 1.9 nm^{-1} to 77.0 nm^{-1} . The total acquisition time per point was $\sim 40 \text{ s}$. Furthermore a Raman experiment was performed, providing the frequency of the highest optical branch at the Γ point of 1584 cm^{-1} (corresponding to 196.1 meV), in good agreement with other experimental and theoretical values [78].

4.3.2 Experimental results

First, the experimental results for momentum transfers within the first Brillouin zone are presented. Then, the intermediate momentum transfer range is discussed, highlighting the importance of the consideration of texture in the modeling. Finally, the refined dispersion relation and the extracted elastic constants are presented.

Low momentum transfer

The results of the low momentum transfer region for pyrolytic graphite are already published by Bosak et al. [14]. The intensity map (see Fig. 4.17) of the low Q range shows two well distinguished dispersions (bright lines). By exploiting the simple dynamical model of Nicklow et al. [79] (solid and dashed line) and comparing it to the intensity map it can be demonstrated that the apparent Q dispersion of high and low energy features mimics the LA in-plane dispersion and LA dispersion along $\Gamma - A$, respectively. In addition, experimental data, obtained from measurements on single crystal graphite, are displayed (triangles, circles and diamonds). The intensity following the LA single crystal dispersion along the $\Gamma - A$ direction is composed of contributions from longitudinal and transverse phonons, even in the low Q and low energy region, due to the high anisotropic forces in graphite. From a momentum transfer of about 6 nm^{-1} on, weak intensity above the

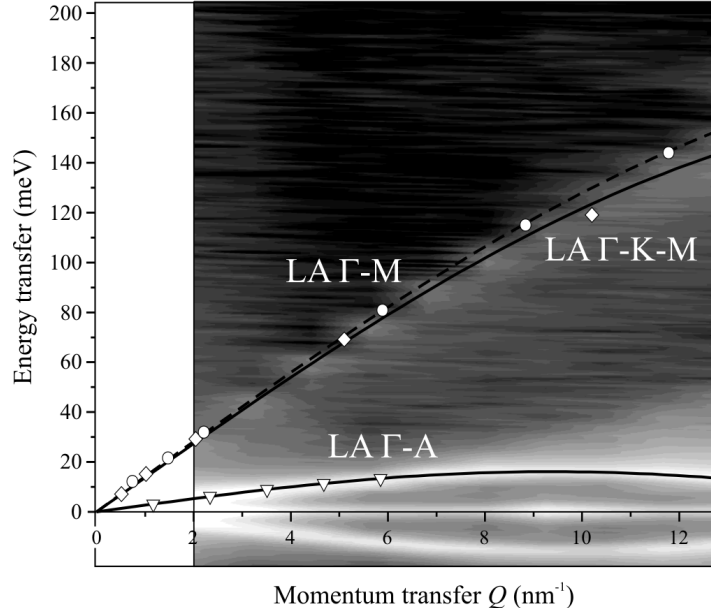


Figure 4.17: Low-Q IXS intensity map of pyrolytic graphite compared to single-crystal phonon dispersion data; longitudinal acoustic phonons along $\Gamma - A$ (triangles), $\Gamma - M$ (circles), and $\Gamma K M$ (diamonds) [84], [85]. Solid and dashed lines are the results of a lattice dynamics calculation [79]. Figure taken from Bosak *et al.* [14].

main intensity (at around 15 meV) can be observed, arising from transverse lattice vibrations in the basal plane. Moreover, the significant difference between the forces within the hexagonal plane and between the layers is also reflected in the sound velocities. The strong forces in the plane lead to a high sound velocity, as can be seen along $\Gamma - M$ where it is 22.16 km/s , while the sound velocity along $\Gamma - A$ is low (4.40 km/s) [85]. This extreme case of graphite, where even at low Q two well-separated dispersions arise, underlines well that the term "average sound velocity" and even "orientational averaged sound velocity" must be used with prudence, especially if strongly anisotropic systems are considered.

The intermediate momentum transfer range

In order to visualise features at higher energy transfer E the intensity of the experimental intensity map (Fig. 4.18) I is scaled $I_{Map} = I_{Exp} \cdot E$. Furthermore, the elastic line is subtracted and the spectra are normalised to the incoming x-ray intensity, the polarisation of the beam, the analyser efficiencies and the atomic form factor. The map shows a pronounced arc structure in the low energy part (up to 20 meV), mainly formed by the dispersion along the $\Gamma - A$ direction. The dominance of these phonons is due to the

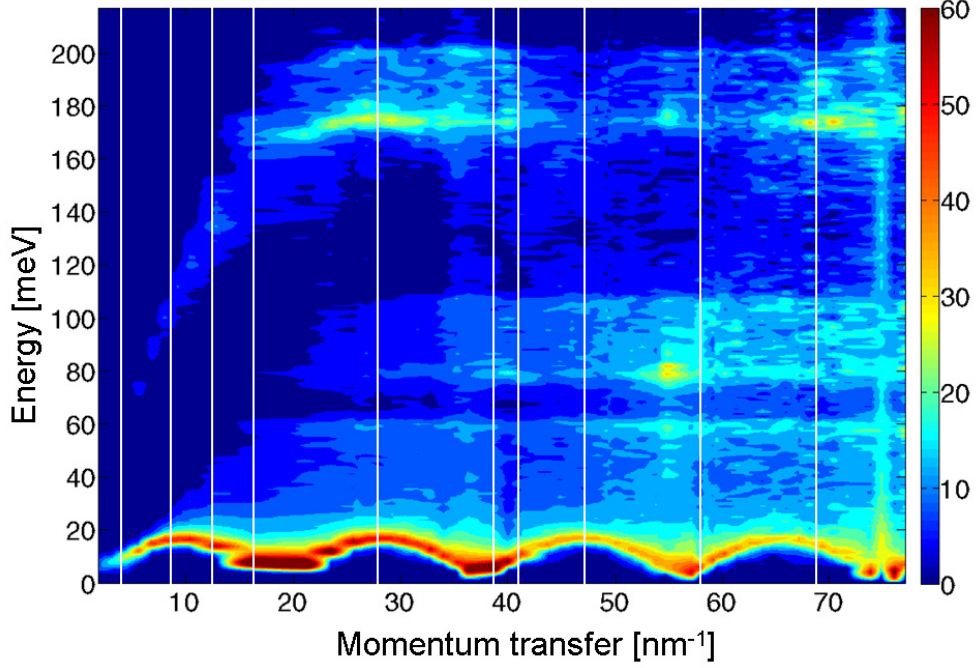
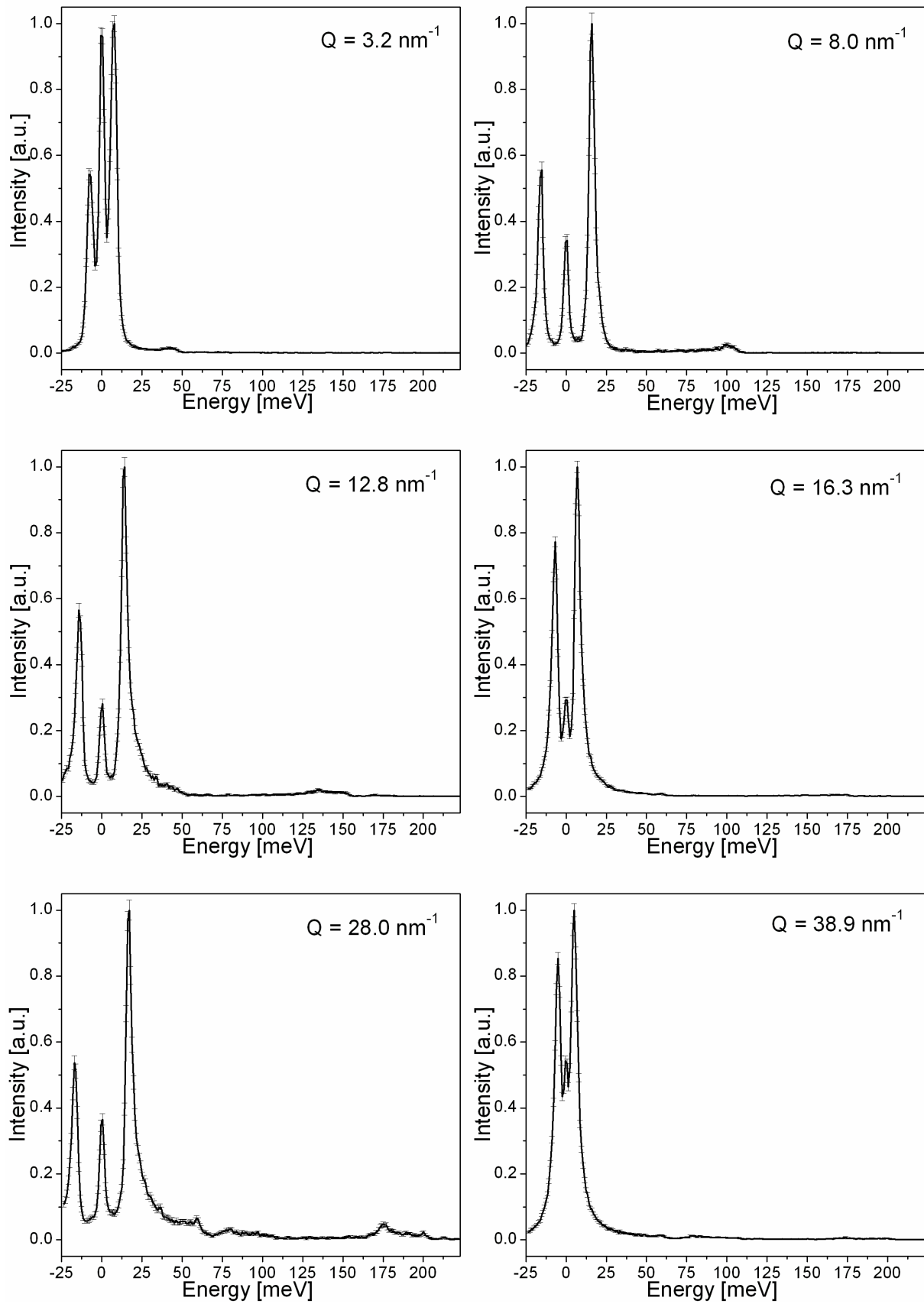


Figure 4.18: Experimental intensity map of pyrolythic graphite. The spectra are normalised and the elastic line is subtracted. The white lines mark the ten constant momentum transfer scans used for the fitting routine.

strong texture, induced by the rotation of the sample in the experiment. In contrast to beryllium, part of the optic branches (mainly along $\Gamma - A$) is superposed to acoustic vibrations in arbitrary directions, both occupying the same energy transfer range. This is due to the highly anisotropic forces in graphite. Above about 20 *meV* only in-plane vibrations contribute to the intensity. At high momentum transfer the density-of-states limit is approached, but the extraction of the VDOS is not straightforward in this highly textured sample. The white lines in Fig. 4.18 indicate the ten spectra used in the refinement procedure. They are at 3.2 nm^{-1} , 8.0 nm^{-1} , 12.8 nm^{-1} , 16.3 nm^{-1} , 28.0 nm^{-1} , 38.9 nm^{-1} , 41.3 nm^{-1} , 47.1 nm^{-1} , 57.8 nm^{-1} , 69.3 nm^{-1} momentum transfer. Like in the case of beryllium, the selected spectra are well distributed over the entire measured momentum transfer range, in order to capture the information contained in the development of the scattered intensity.

In Figure 4.19 the chosen experimental spectra including their error bars are shown. They are normalised to the maximal intensity in the corresponding scan. The dominating feature, besides the elastic line at zero energy transfer, is a peak at low energy transfer. This intensity forms the arc structure at low momentum transfer in the experimental

Experimental results



4.3 Monoatomic hexagonal system with texture

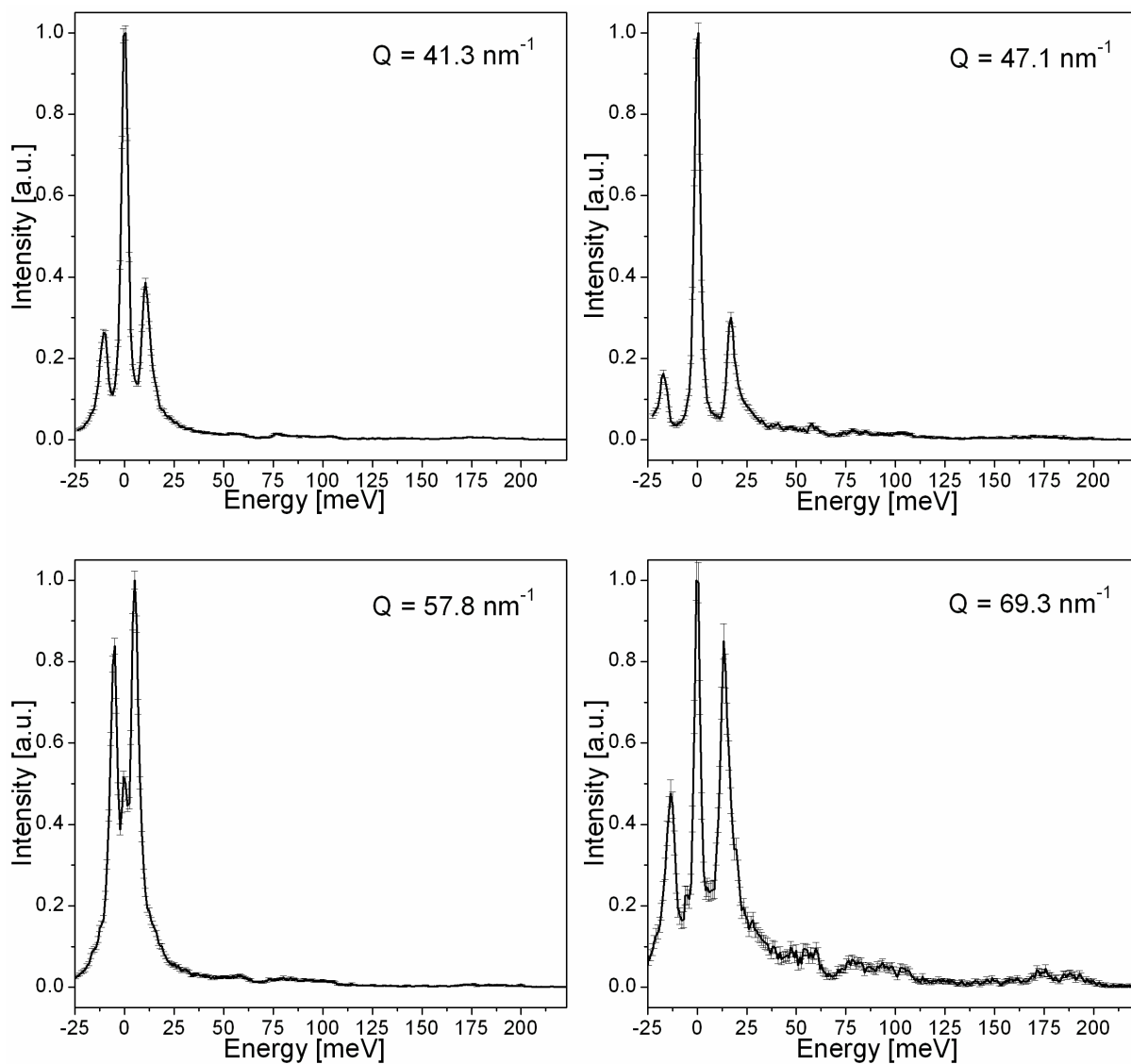


Figure 4.19: Selection of experimental IXS spectra used for the fit.

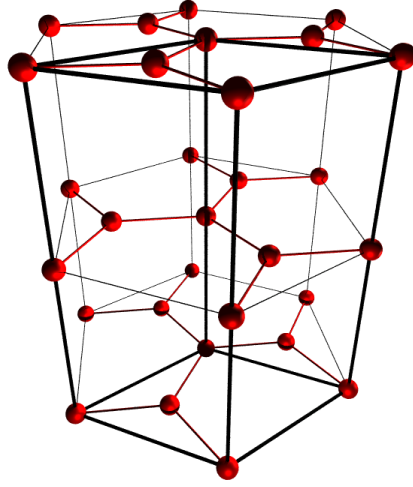


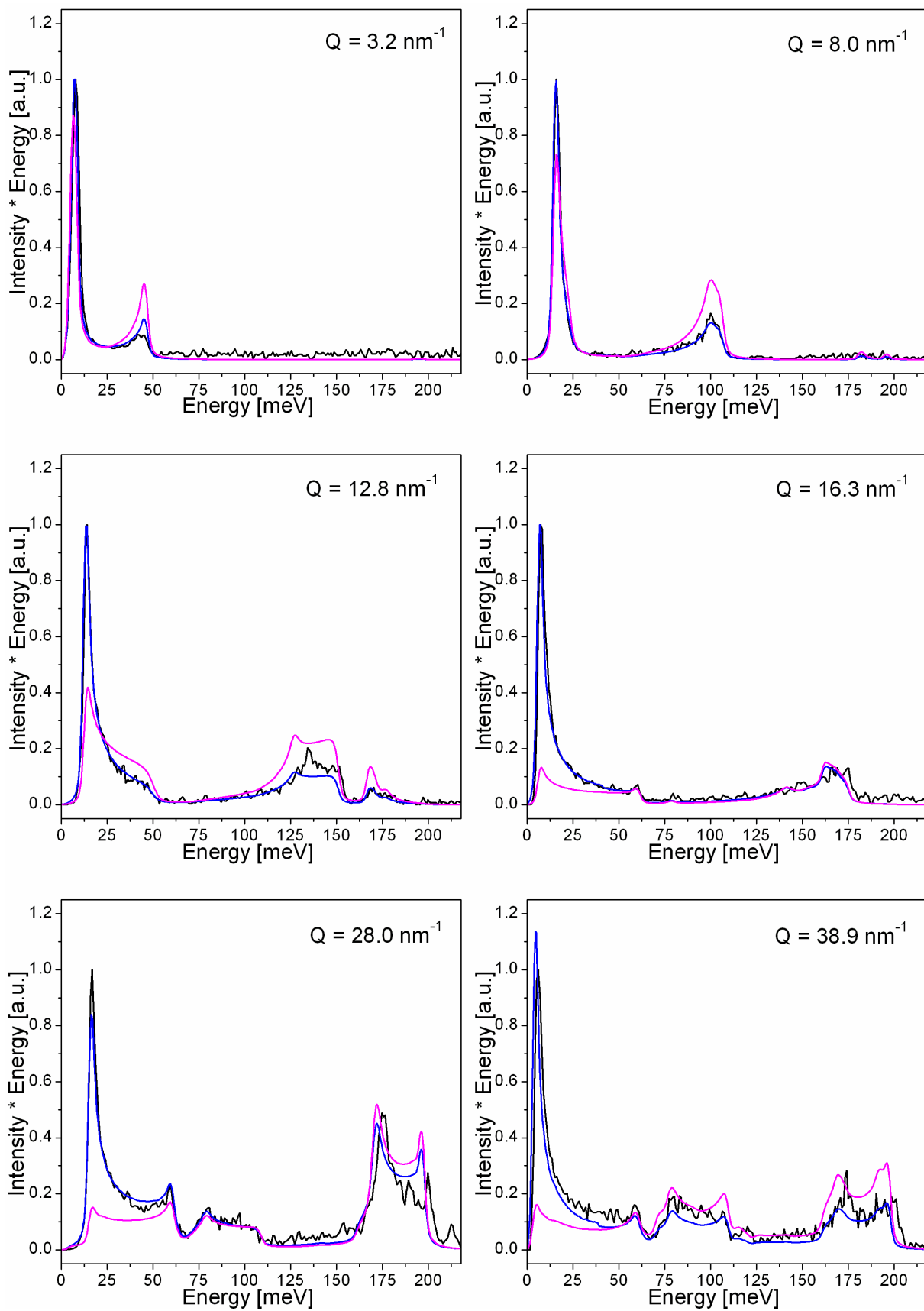
Figure 4.20: Hexagonal lattice of graphite.

intensity map. As aforementioned, the strong intensity of this inelastic peak is due to the texture in the sample which amplifies the scattering along $\Gamma - A$. The asymmetric shape of this peak (for example $Q = 28.0 \text{ nm}^{-1}$) is remarkable. The slope at lower energy is steeper than the slope on the higher energy side. A simple elasticity - based model shows also an asymmetric shape of this peak, but with opposite asymmetry [14]. The difference between experiment and model calculation arises, since contributions of transverse phonons are not taken into account in the model. These vibrations contribute significantly to the scattering intensity at the higher energy side of the peak, especially in this particular case of highly anisotropic graphite.

Despite the weakness of the inelastic intensity at higher energy transfer, it is possible to notice changes in the shape over the momentum transfer range. In order to emphasise the inelastic features, we used the following scale for the intensity I : $I = I_{Exp} \cdot E$, where E is the energy transfer. This scaling will be used in all further figures for graphite and in the fitting routine.

Graphite has a hexagonal unit cell with atoms at position $[0, 0, 0]$, $[2/3, 1/3, 0]$, $[0, 0, 1/2]$ and $[1/3, 2/3, 1/2]$. The basis vectors are: $a = 2.462 \text{ \AA}$ and $c = 6.711 \text{ \AA}$ (see Fig. 4.20). We used a Born - von Kármán model, including up to the 6th nearest neighbour. Mohr *et al.* [84] published a set of force constants for graphene, obtained from a least squares fitting routine to the experimental IXS dispersion measured on single crystal graphite. The elastic properties of the two dimensional graphene sheet are very similar to the one of graphite, since the forces between the basal planes are weak. The published force constants up to the 5th nearest neighbour were used as starting parameters for the model calculation. In addition, in order to include forces between the basal planes, the force

4.3 Monoatomic hexagonal system with texture



Experimental results

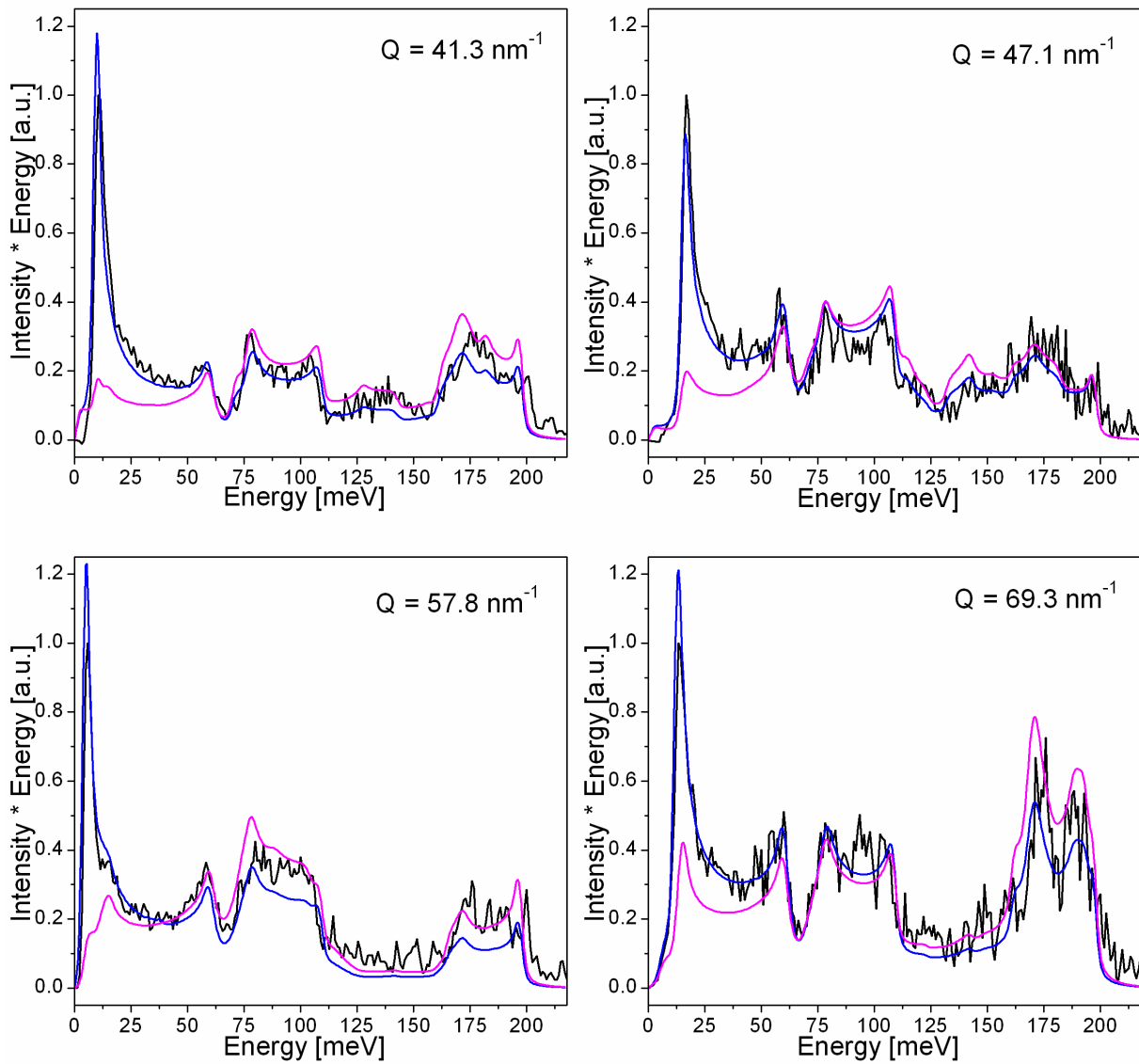


Figure 4.21: Comparison of the experimental data (black line) with the model without considering texture (pink line) and including texture (blue line).

4.3 Monoatomic hexagonal system with texture

constants for the 4th nearest neighbour published by Nicklow *et al.* [79] were incorporated. Altogether we included 17 force constants in the model calculation. For the notation and definition of direction in the hexagonal unit cell see table 4.4.

In pyrolytic graphite the c-axes of the crystallites are aligned within a few degrees, while the a-axes are randomly orientated in the plane perpendicular to the c-axes. As aforementioned the sample was rotated with a frequency of about 10 Hz around an axis, perpendicular to the crystallographic c-axis and the horizontal scattering plane. For this given texture the orientation matrix g [86] reduces to:

$$g = \begin{pmatrix} 1 & 0 & 0 \\ 0 & \cos(\theta) & \sin(\theta) \\ 0 & -\sin(\theta) & \cos(\theta) \end{pmatrix} \begin{pmatrix} \cos(\varphi) & \sin(\varphi) & 0 \\ -\sin(\varphi) & \cos(\varphi) & 0 \\ 0 & 0 & 1 \end{pmatrix} \quad (4.4)$$

The angles θ , φ and ψ correspond to the Euler angles. The orientation distribution in a polycrystalline material is mathematically represented by the orientation distribution function $f(g)$, which is in our case:

$$f(g) = \frac{4}{\sin(\theta)} \delta(\psi) \quad (4.5)$$

The orientation distribution function is normalised

$$\int f(g) dg = 1 \quad (4.6)$$

with

$$dg = dpd\theta d\psi \sin(\theta) / 8\pi^2 \quad (0 \leq \varphi; \psi \leq 2\pi; 0 \leq \theta \leq \pi) \quad (4.7)$$

Such a configuration is equivalent to the study of a textured sample with a weighting function $W(\theta) = 1/\sin(\theta)$, where θ is the angle between the incident beam and the c-axis. Considering the experimental geometry one obtains for the scattered intensity:

$$\langle I(E) \rangle = \int I(\theta, \varphi, E) f(g) dg$$

This texture is easy to implement in the modeling. In Figure 4.21 the experimental spectra (black line) are compared to two model calculations, one computed with a uniform distribution of crystallographic directions (pink line) and the other one including texture (blue line). Clear changes in the relative intensities between the model with and without texture can be observed. The peak at low energy transfer, due to vibrations along the $\Gamma - A$ direction becomes more pronounced, while the inelastic features at higher energy transfer, mainly due to vibrations within the basal plane, are weakened in the case of the textured system. The changes are not as pronounced for lower Q as for higher momentum

Experimental results

transfers. Generally, the intensity due to vibrations along $\Gamma - A$ is amplified as a result of the texture, whereas the peak positions are independent of the texture. The comparison of the two calculated inelastic spectra underlines the importance to consider texture in the model calculation.

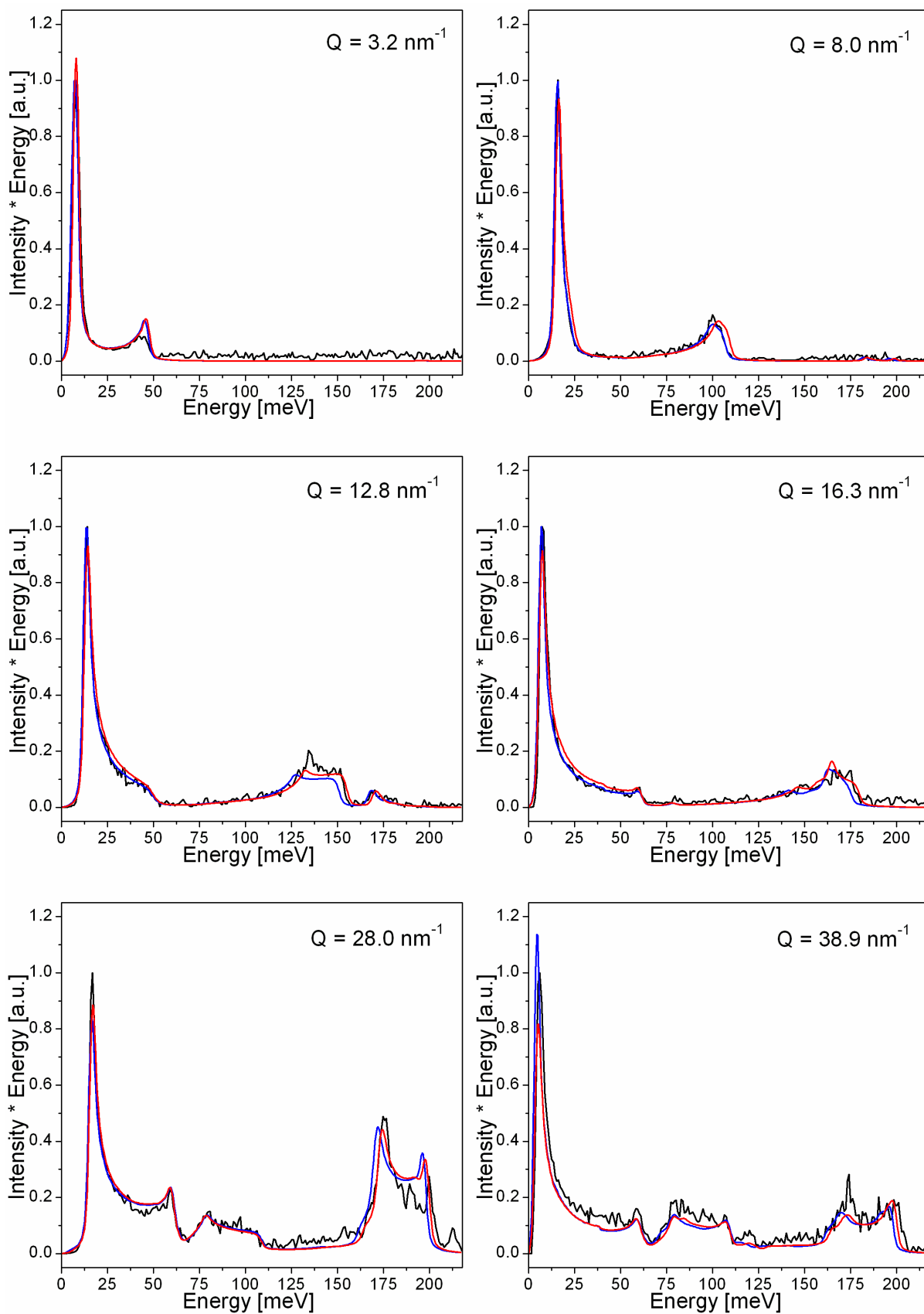
In order to refine the model calculation to the experimental data, a least squares fitting routine was performed. The Born - von Kármán model including forces up to the 6th nearest neighbours was refined to the ten selected experimental spectra. The energy of the highest optical branch at the Γ point ($E = 196.1 \text{ meV}$) was included as a further experimental constraint, with the weight of one experimental spectrum. The starting parameters for the fitting routine were the same as for the model calculation [84], [79]. Only one neighbour interaction along the $\Gamma - A$ direction was considered (α_4, β_4) and therefore the force constants for the 5th and 7th nearest neighbour interaction were neglected. Since the main contribution of the longitudinal and transverse vibrations in this direction overlap with the intense peak at low energy transfer, it is not sensible to refine both α_4 and β_4 . The parameter α_4 was therefore fixed to $\alpha_4 = 0.87$, after adjusting it by hand to the experimental data, while b_4 was refined. The starting and refined parameters are given in table 4.7. The merit function, measuring the agreement between experimental data and model calculations during the fitting routine, decreased by 41.6 % from $\chi_{start}^2 = 3.34$ to $\chi_{end}^2 = 1.95$, during 16 iterations. In Figure 4.22 the experimental spectra (black line) are confronted with the model calculation (blue line) and the refined model (red line). There is a remarkably good overall agreement of the refined spectra with the experimental data. Compared to the model calculations, some peak positions were improved (see high energy transfer region for momentum transfer $Q = 12.8 \text{ nm}^{-1}$, 28.0 nm^{-1} , 41.3 nm^{-1}). Furthermore, the relative intensities, mainly for high momentum transfers, match better.

Using the resulting force constants the momentum transfer - energy transfer intensity map was computed (Fig. 4.23). As expected, it shows an excellent agreement with the experimental intensity map (see Fig. 4.18). In addition, the difference map between the experimental and the calculated map is given in Fig. 4.24. The experimental spectra are scaled to the calculated spectra and then the calculated map is subtracted from the experimental map. No strong difference is noticed.

Dispersion relation

Finally the dispersion, derived from the refined force constants (red line) is confronted to experimental data in Fig. 4.25. The experimental dispersion along the $\Gamma - K - M - \Gamma$ direction, was determined with IXS (black dots [83] and black triangles [84]) at room temperature on single crystalline graphite flakes. The dispersion along $\Gamma - A$ direction

4.3 Monoatomic hexagonal system with texture



Experimental results

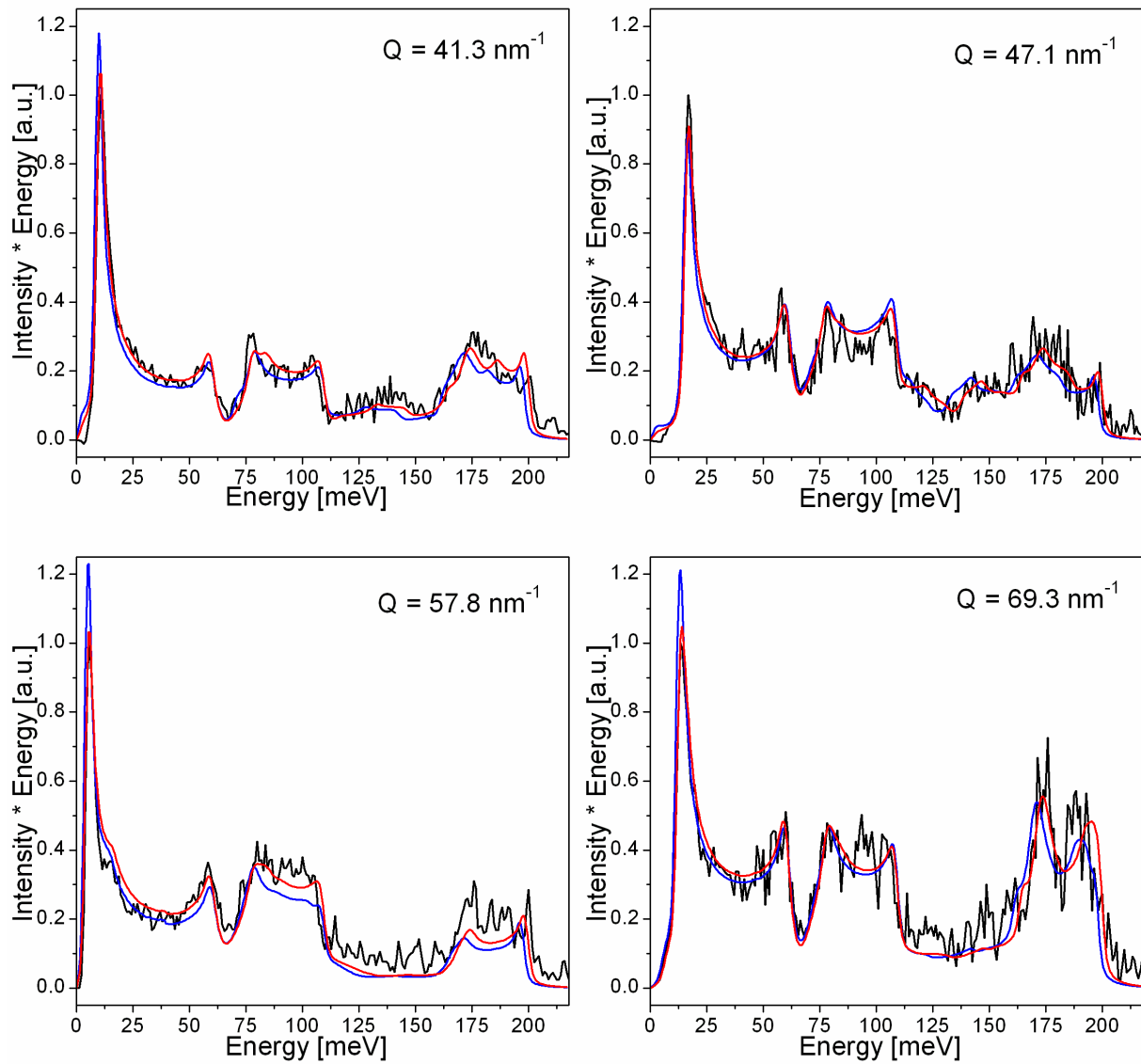


Figure 4.22: Experimental IXS spectra of textured graphite (black line) compared to model calculations (blue line) and the least squares refined data (red line).

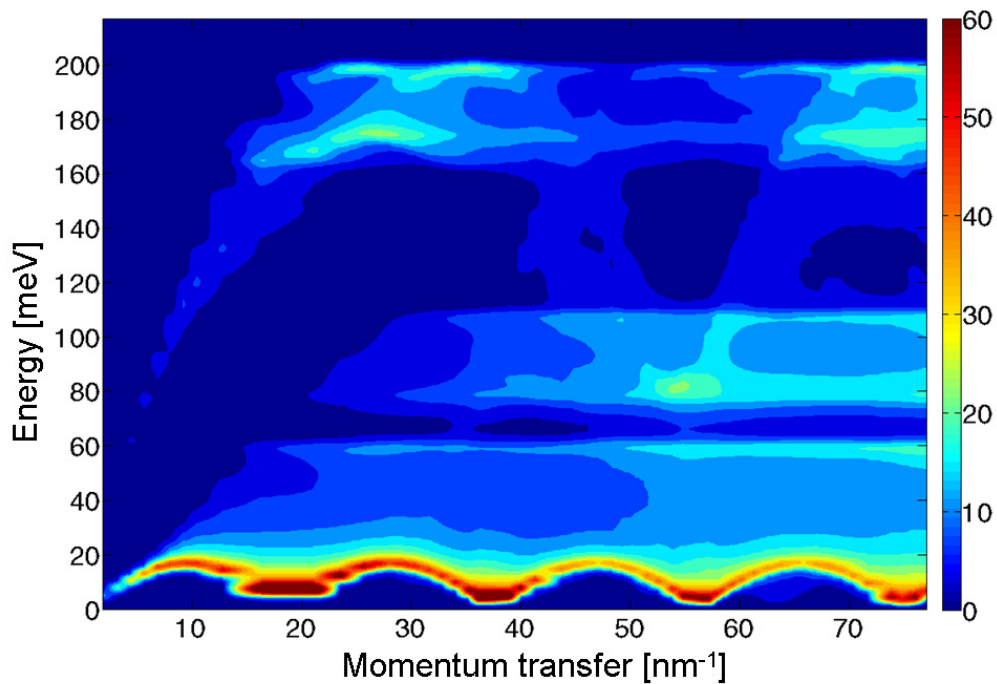


Figure 4.23: Intensity map for the refined model calculation of graphite.

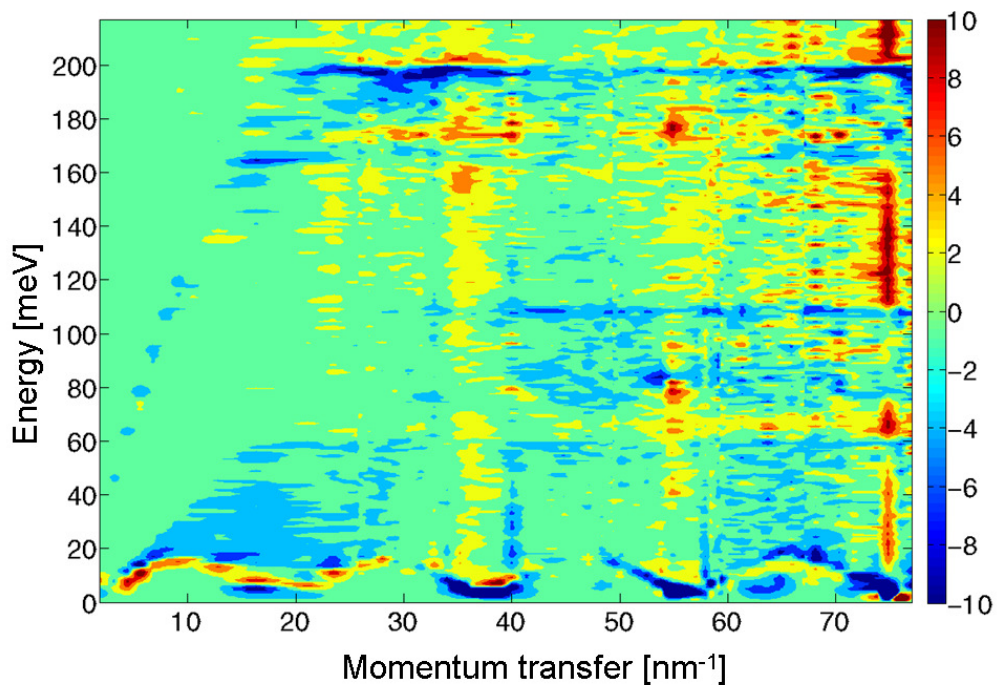


Figure 4.24: Difference between the experimental data and the refined model for graphite.

Experimental results

	α_1	β_1	γ_1	α_2	β_2	γ_2	α_3	β_3	γ_3
refined parameters	411.6	154.3	97.13	-45.02	74.50	-8.24	-53.09	56.94	8.59
Mohr <i>et al.</i> [84]	414.1	134.7	98.93	-48.70	64.59	-7.87	-48.26	63.17	8.26
Nicklów <i>et al.</i> [79]	-	-	-	-	-	-	-	-	-

	α_4	β_4	α_6	β_6	γ_6	δ_6	α_8	β_8	γ_8
refined parameters	0.87	6.19	3.49	5.94	-7.77	1.96	16.67	1.71	1.91
Mohr <i>et al.</i> [84]	-	-	6.04	5.05	-8.34	1.70	16.56	2.66	1.76
Nicklów <i>et al.</i> [79]	0.77	5.8	-	-	-	-	-	-	-

Table 4.7: Force constants for graphite.

was studied on pyrolytic graphite by INS [79] (black squares). Furthermore, the dispersion computed with the starting parameters (blue line) is shown. The most obvious difference between the refined dispersion and the experimental one is along the $\Gamma - K$ direction. Here, the energy of longitudinal acoustic and transverse acoustic branches is too high at the K point (at about 130 *meV*, while the experiment gives 125 *meV*). Nevertheless, the refined model improved the agreement for the transverse optic branch (branch just above) compared to the model published by Mohr *et al.* [84]. Furthermore, the refined dispersion in the higher optical part (above 140 *meV*) changes with respect to the starting model for the $K - M$ direction, but since the trend of the experimental data is ambiguous in this region, one cannot conclude on an improvement.

Elastic properties

The elastic constants are derived from the initial slope of the acoustic branches, using the density of graphite $\rho_G = 2.267 \text{ g/cm}^3$. The exact procedure is described in section 1.1.2. The obtained values are presented in table 4.8. For C_{11} and C_{33} we used the LA branch along ΓM and ΓA , respectively. C_{11} is significantly lower (19%) than the one obtained by INS [79]. One should be aware that the INS experiment studied a pyrolytic graphite sample. Thus, the in-plane LA branch is the least reliable in this experiment due to the nature of the sample. On the other hand, the obtained C_{11} is in good agreement with IXS results from a single crystal flake [85]. Both C_{44} and C_{66} were derived from TA branches with different polarisations along $\Gamma - K$. The elastic modulus C_{66} is significantly higher than the values obtained by IXS [85] and INS [79]. This is expected if one compares the slope of the steepest TA branch along $\Gamma - K$ direction (used for the extraction of C_{66}) in Fig. 4.25. The slope for the calculated dispersion is steeper than the experimental data. Furthermore, the value of C_{12} calculated using the relation $C_{12} = C_{11} - 2C_{66}$ shows a large difference (87%) compared to the value published by Bosak *et al.* [85]. This is not

4.3 Monoatomic hexagonal system with texture

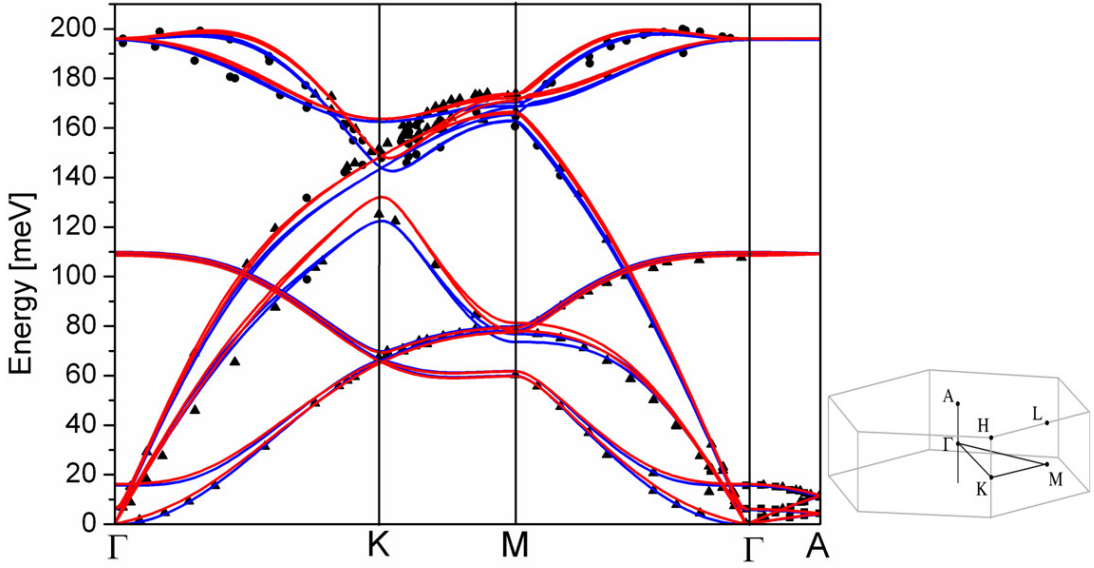


Figure 4.25: Dispersion along the main symmetry directions for graphite. The refined model calculation (red line) shows a good agreement with the experimental INS data (black dots). Furthermore, the dispersion of the starting model (blue line) is given.

surprising, since C_{12} depends on C_{11} and C_{66} . C_{13} contributes neither to the sound velocity in-plane nor along the c -direction, but only along non - symmetry directions. Thus C_{13} is poorly defined due to the large structural anisotropy. We follow the conclusion in [85] and set $C_{13} = 0$. Numerous *ab initio* calculations are published, giving a wide spread of values for the elastic constants [87], [88], [89]. In table 4.8 we show *ab initio* calculations, performed within the local density approximation using an all-electron full-potential linear combination of Gaussian-type orbitals fitting-function technique [90]. This calculation is in good agreement with our experiment.

	C_{11}	C_{12}	C_{13}	C_{33}	C_{44}	C_{66}
present work	1161	17.8	-	39.7	5.58	571.6
Bosak <i>et al.</i> [85]	1109 (16)	139 (36)	0 (3)	38.7 (7)	5.0 (3)	485 (10)
Nicklow <i>et al.</i> [79]	1440 (220)	-	-	37.1 (5)	4.6 (2)	460
Boettger [90]	$C_{11} + C_{12} = 1280$		-0.5	40.8	4.5	-

Table 4.8: Comparison of the elastic constants for graphite from polycrystalline IXS data with previous experimental and theoretical values. All values are in GPa. Errors are given as far as available.

4.4 Diatomic tetragonal system

For the tetragonal system stishovite, an *ab initio* calculation performed with the program CASTEP is compared to the polycrystalline IXS spectra. This allows the evaluation of the theoretical approach. Furthermore, single crystal measurements are presented, confirming the result obtained for the polycrystalline system. It is worth noting that the data collection for the polycrystalline experiment was faster than the measurement of the single crystal dispersion.

4.4.1 Stishovite

Stishovite is a polymorph, high pressure and high temperature phase, of SiO_2 , and was first synthesised by Stishov *et al.* [91] in the laboratory in 1961. It raises interest in various domains:

- Stishovite sparked interest in planetary sciences, since its discovery in the impact crater at Meteor Crater, Arizona [92] in 1962.
- The interest in geophysics arises from the fact that stishovite is a component of the natural mid-oceanic ridge basalt in the lower Earth's mantle [93], produced either by transformation of alpha-quartz or as a disproportionation product of common silicate minerals [94].
- In material sciences it is known because of its extraordinary hardness; as a matter of fact it is often referred to as the hardest known oxide and representative of one of the hardest known polycrystalline materials in general [95].

In most silica polymorphs the silicon atoms are fourfold coordinated and the oxygen atoms are twofold coordinated, whereas in stishovite the silicon atoms are sixfold coordinated, and oxygen atoms are threefold coordinated. It is the simplest example of a compound with silicon atoms in sixfold coordination. The oxygen and silicon atoms form polar covalent bonds, with the bond maxima closer to the more electronegative O atom. The density of stishovite (4.28 g/cm^3) is about 46% greater than that of the densest of the fourfold coordinated polymorphs (coesite). This can be explained by the distance of the closest non-bonded oxygen atom (2.29 \AA), which is considerably shorter than twice the Pauling ionic radius of oxygen ($2.8 \text{ \AA} - 3.52 \text{ \AA}$) [96]. At ambient conditions stishovite is metastable and micro-grain sized polycrystalline stishovite synthesised in high-pressure presses and from natural impacts may remain structurally ordered over geological timescales.

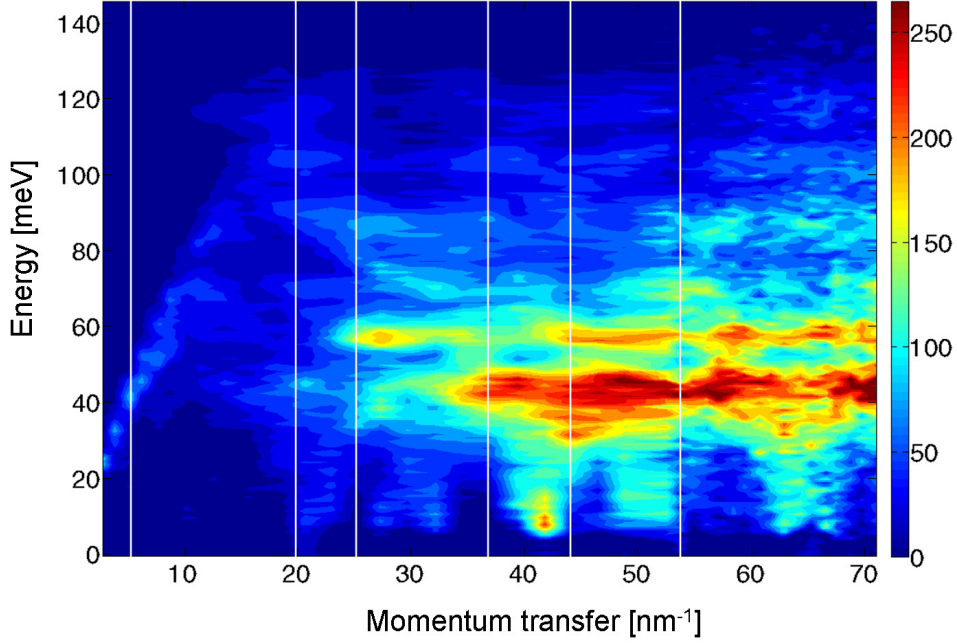


Figure 4.26: Experimental momentum - energy transfer intensity map of stishovite. The white lines indicate the spectra selected for the comparison with theoretical calculations.

The lattice dynamics of stishovite is still not completely characterised. Several *ab initio* calculations [97], [98], [99] were performed, contradicting each other mainly in the optical part of the dispersion. Experimental phonon frequencies were available only for zone - center modes [100], [101], and only recently, Bosak et al. [?] measured parts of the dispersion on a small single crystalline grain of stishovite by IXS.

4.4.2 Experimental results

The absence of texture in the polycrystalline stishovite sample (thickness ~ 1 mm) was confirmed by the uniform intensity distribution around the Debye - Scherrer rings. IXS spectra were recorded from 3.9 nm^{-1} to 71.0 nm^{-1} , using the Si(9 9 9) configuration, as in the case of beryllium (see section 4.2.2) and graphite. The total acquisition time per point was ~ 120 s.

The experimental IXS intensity map is shown in Fig. 4.26. The intensity is normalised to the incoming x-ray intensity, the polarisation of the X-rays and the analyser efficiencies. With respect to beryllium and graphite less structure is observed. The scattering of longitudinal phonons at low momentum transfer is only weakly visible. Regions of high scattering intensity are observable around 40 meV and 60 meV, indicating flat branches in the dispersion at these energies. The six selected IXS spectra, indicated by a white line

Experimental results

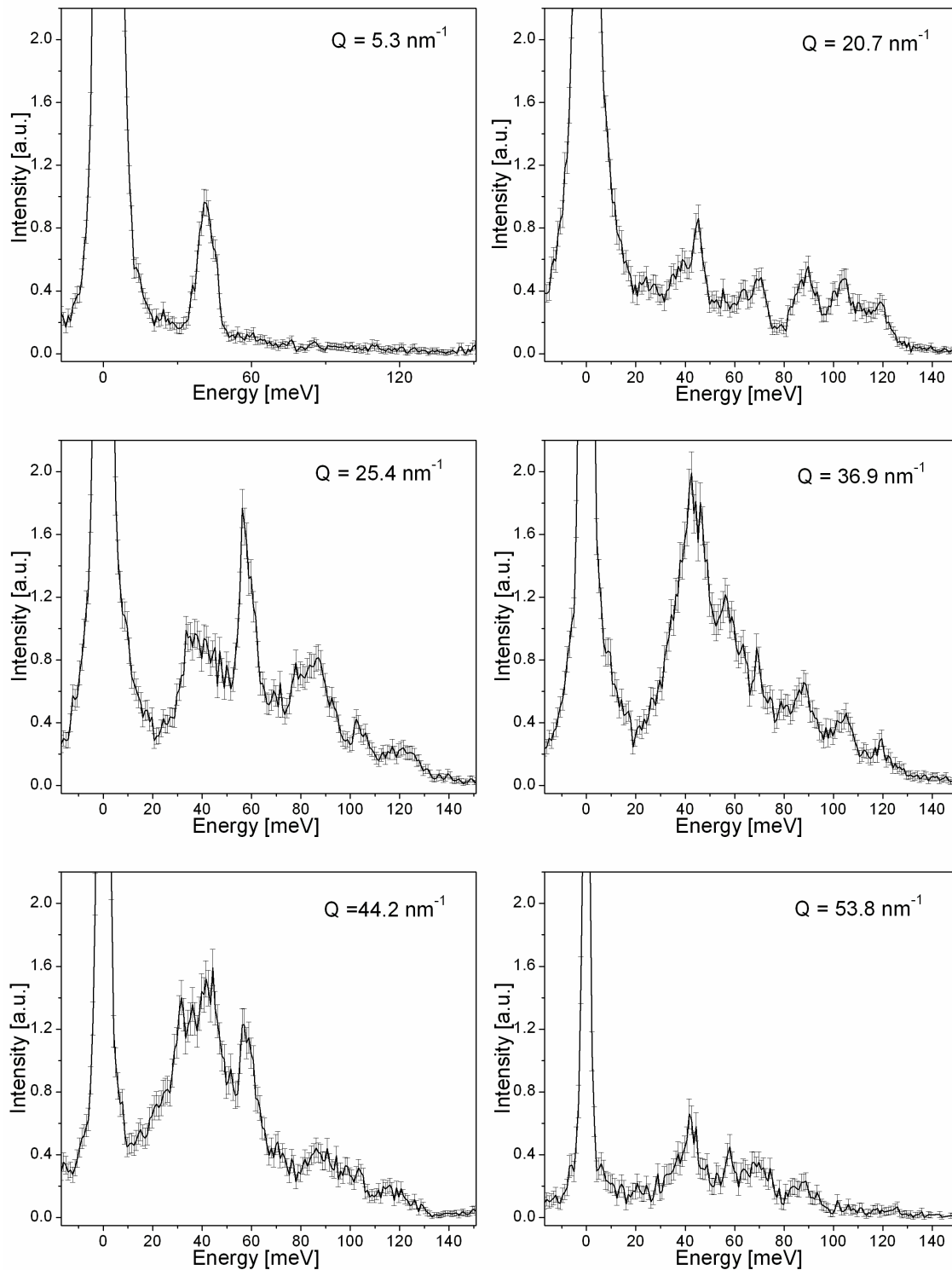


Figure 4.27: Experimental IXS spectra for stishovite. The intensity is normalised and the error bars are shown.

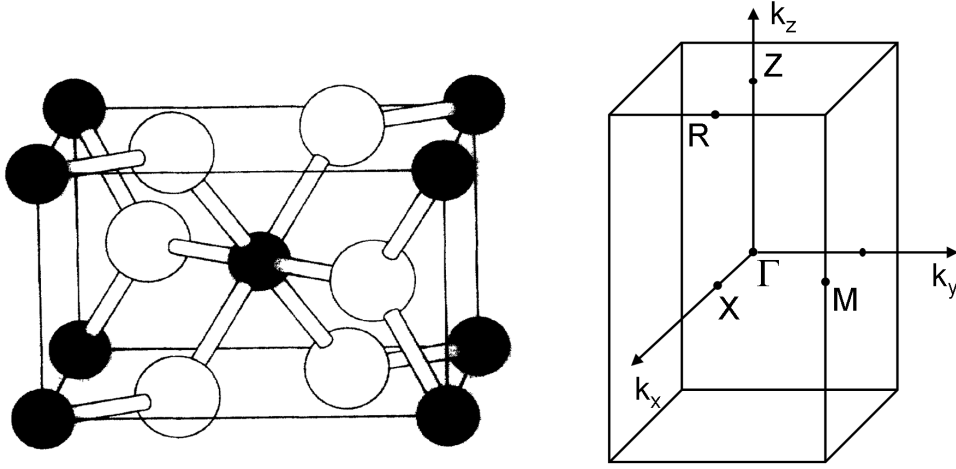


Figure 4.28: Left side: unit cell of stishovite. White circles denote O atoms, and black circles Si atoms. Figure taken from Lee *et al.* [99]. Right side: Brillouin zone of stishovite with its high symmetry directions.

in the intensity map, are shown in Fig. 4.27. These were selected, since they cover a large part of the momentum transfer range and show distinct features and variations in their shapes. The intensity is normalised to the incoming intensity and the error bars represent the statistical error. The intensity of the elastic line is about 15 times higher than the intensity of the inelastic features due to the lower crystal quality of the crystalline grains. This is in contrast to the others experiments on beryllium and graphite, where the elastic intensity is about the same as the inelastic one. Thus, the subtraction of the elastic line is more difficult for stishovite. Although the spectra show a distinct inelastic structure the complexity of the system (number of atoms in the unit cell) allows only the comparison of the IXS spectra to a theoretical model, without refining the model parameters.

4.4.3 Comparison with theoretical model

Stishovite has the rutile structure with space group D_{4h}^{14} , having silicon atoms at $(0, 0, 0)$ and $(1/2, 1/2, 1/2)$ and oxygen atoms at $(u, u, 0)$ $(1-u, 1-u, 0)$, $(1/2-u, 1/2+u, 1/2)$ and $(1/2+u, 1/2-u, 1/2)$. The lattice constants a and c and the internal atomic coordinate u are 4.18 \AA , 2.67 \AA and 0.305 , respectively. The unit cell of stishovite is illustrated in Fig. 4.28 (left side). In order to calculate the polycrystalline average, a mesh of Q - points on a spherical surface is computed. In a first step, all momentum transfers Q are reduced to the first Brillouin zone. Furthermore, a theoretical model provides the lattice dynamics of the single crystal. Energies and polarisation vectors are computed in the framework of the model for a uniform mesh of Q - points within the first Brillouin zone ($-0.5 < q_x < 0.5$,

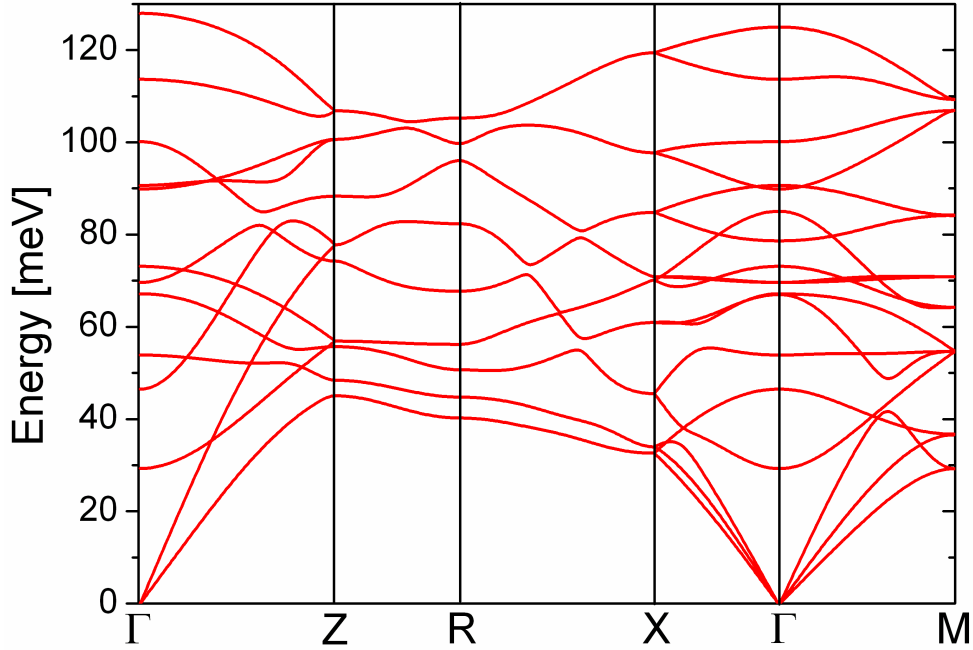


Figure 4.29: Phonon dispersion of stishovite, obtained by the *ab initio* program CASTEP.

$-0.5 < q_y < 0.5$, $0 < q_z < 0.5$). For the z -direction only positive mesh points are used, since scattering from $(-q_x, -q_y, -q_z)$ can be deduced from the scattering intensity at (q_x, q_y, q_z) considering the relation for the polarisation $\vec{\sigma}(q) = \overline{\vec{\sigma}(-q)}^1$. In addition, the mesh is displaced with respect to high symmetry directions (see Chapter 2.2.3). The polarisation vector of the mesh point closest to the reduced momentum transfer is then multiplied by a phase factor, taking the Brillouin zone in which the original momentum transfer was situated into account. Finally, the average was computed, summing up the IXS intensity of the corresponding mesh points.

Calculations with CASTEP

Ab initio calculations of the lattice dynamics were performed by B. Winkler [?]. The density functional perturbation theory calculations were computed with the commercial and academic versions of the CASTEP [?] code. An energy cut-off of 750 eV was applied to the norm-conserving pseudopotentials. A test at 1000 eV showed that the calculations were fully converged. In Figure 4.29 the single crystal dispersion is shown. In order to compute the polycrystalline average, polarisation vectors and energies were calculated at mesh points with a spacing of 0.03 nm^{-1} along the a and c direction. The energy scale of the computed polycrystalline IXS spectra (see Fig. 4.30) had to be scaled by a factor

¹ $\overline{\vec{\sigma}(q)}$ is the complex conjugate of $\vec{\sigma}(q)$.

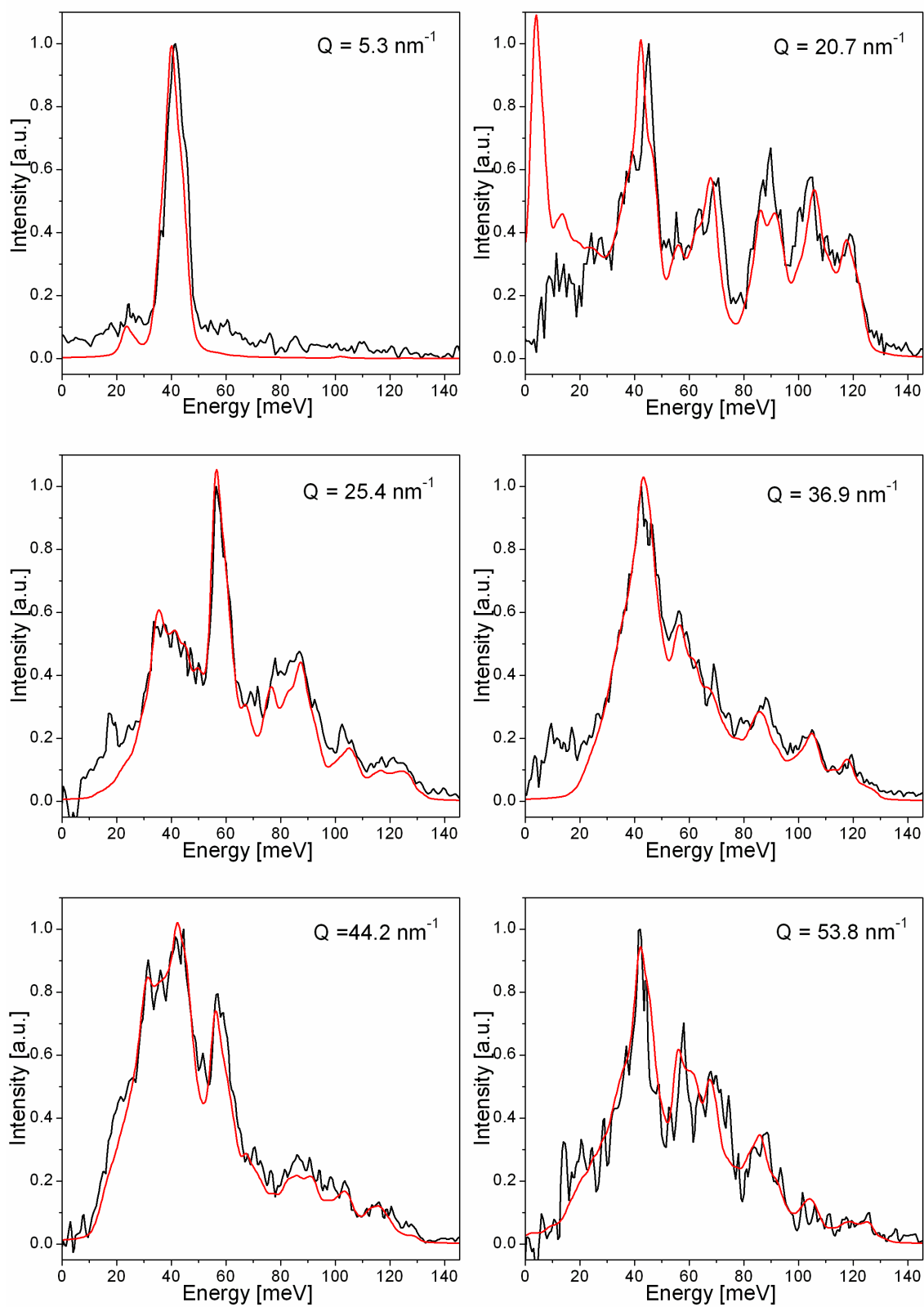


Figure 4.30: Comparison of the experimental polycrystalline spectra (black line) and the theoretical model for stishovite obtained by the program CASTEP (red line).

Experimental results

of 1.05 in order to improve the agreement with the experimental spectra. Such an error is typical for density - functional theory (DFT) calculations.

One can appreciate that not only the overall shape of the spectra throughout the whole momentum transfer range is well reproduced, but also all peak positions and the intensity distribution over the entire energy range. The agreement between experiment and theory is excellent. Discrepancies occur only for an energy transfer below 20 meV (25.4 nm^{-1} , 36.9 nm^{-1} momentum transfer). Here one has to note that the experimental intensity in this low energy region occurs only on the energy loss side and can therefore be identified as parasitic scattering, probably due to a poorly aligned beam stop. Hence, no conclusions can be drawn in this energy range. The inelastic peak in the theoretical spectra at 5 meV energy transfer for 20.7 nm^{-1} momentum transfer is masked by the elastic line. It cannot be separated from it and is subtracted with the elastic line. Due to the very good agreement between theory and polycrystalline spectra one can draw the conclusion that the *ab initio* calculation reproduce very well the lattice dynamics of stishovite.

4.4.4 Single crystal stishovite

A large part of the phonon dispersion was very recently determined by Bosak et al. [?] from a small single crystal (size 150 $\mu m \times 250 \mu m \times 700 \mu m$). The rocking curve of the crystal with 0.003° *FWHM* indicated a very good crystal quality. The dispersion was recorded along $\Gamma - X$, $\Gamma - M$ and $\Gamma - Z$ directions with an energy resolution of 3 meV .

Figure 4.31 shows the calculated dispersion obtained by the CASTEP program compared to the experimental results. In accord with the result obtained for the polycrystalline spectra, the energy scale had to be multiplied by a factor 1.05. One can appreciate an excellent agreement between theory and experiment for all the branches as could be anticipated from the very good match of the individual polycrystalline IXS spectra.

It is important to note that the data for the polycrystalline material were recorded in about two days, while the data collection for the single crystal experiment took four days. Thus, IXS measurements on polycrystalline materials is a fast and valuable tool to evaluate theoretical predictions, even when single crystals are available.

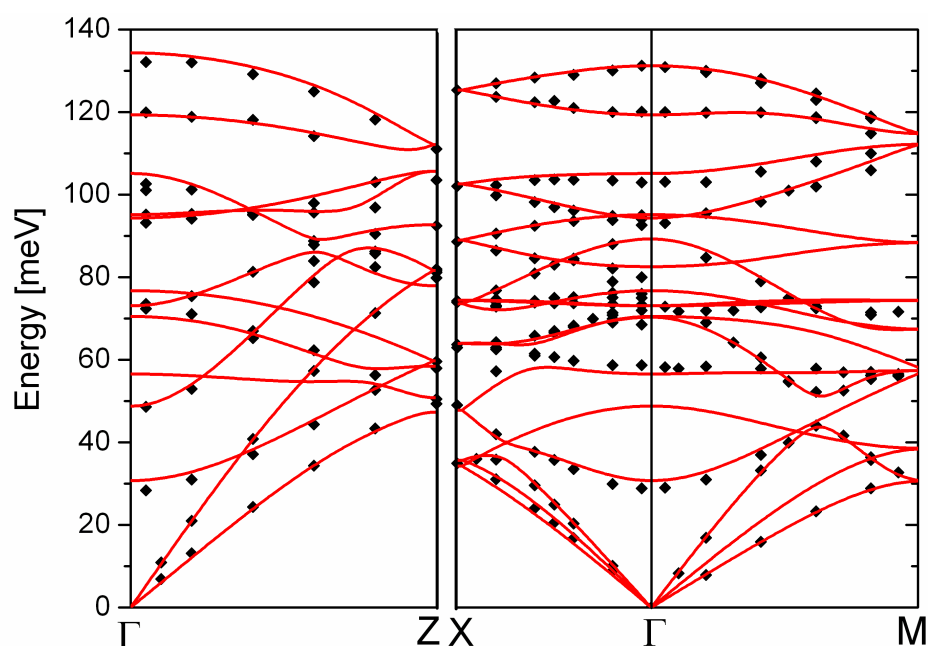


Figure 4.31: Experimental phonon dispersion of stishovite (black diamonds) compared to theoretical results obtained with the program CASTEP (red line). The theoretical energy scale was multiplied by an factor 1.05.

Résumé du chapitre 4

Le chapitre 4 est dédié à la présentation des résultats expérimentaux, en commençant par le cas de l'oxyde de magnésium (cubique), dans lequel les trois modules élastiques sont obtenus à partir de mesures indépendantes du module de compressibilité, de la vitesse de Debye et de la vitesse du son longitudinale moyenne. Nous avons ensuite choisi le béryllium comme premier test pour mettre au point la méthode d'extraction des dispersions de phonon dans les monocristaux à partir de données expérimentales sur mesurées pour une large gamme de moments transférés. Nous démontrons de plus que cette méthode sur poly-cristaux permet de discriminer deux modèles Born - von Kármán différents mais a priori équivalents. Nous étudions ensuite les effets de texture dans le cas du graphite pyrolytique. L'inclusion de ces textures dans l'analyse des données permet un excellent ajustement du modèle aux données expérimentales. Dans les deux cas du béryllium et du graphite, la dispersion des phonons est calculée et les constantes élastiques sont dérivées. Le travail sur la stishovite illustre enfin les possibilités de la méthode pour les investigations menées sur des systèmes plus complexes. Cela montre en particulier comment cette technique peut être utilisée très efficacement pour valider un modèle de dynamique de réseaux, a posteriori confirmé par les mesures sur monocristaux.

Chapter 5

Further developments

This chapter discusses the current limitations of the methodology, due to the analysis procedure and/or experimental difficulties, and proposes routes for further developments. In particular, extensions to high pressure applications are discussed.

5.1 Complexity of the studied materials

Two aspects determine the complexity of a system: the number of atoms in the unit cell and the nature of the bonding between neighbouring atoms.

The $3N$ (N number of atoms in unit cell) phonon branches of a system occupy a given energy range, which is more and more dense as N increases. This smoothens the polycrystalline IXS spectra, and distinct features can no longer be observed. As a consequence, a refinement of the model is not possible. A rough rule of thumb could be that in cases where theoretical calculations show such a high density of optical branches in an energy region that the experimental energy resolution is not sufficient to resolve contributions from different branches, one cannot expect distinct features in the IXS spectra. Furthermore, the quality of the inelastic signal depends not only on the number of the atoms in the unit cell, but also on the type of elements. In a system composed of heavy and light elements the vibrations of the light elements are masked by the strong signal arising from the heavy atom species (cross section approximately proportional to Z^2). In order to judge the feasibility for a system, it is recommendable to compute the IXS intensity followed by a test experiment, recording only a sub-set of inelastic spectra in the intermediate momentum transfer range.

Another constraint arises from the number of force constants (equivalent to fitting parameters) needed to describe the system. The more force constants have to be considered, the more distinctively different IXS spectra are necessary for the refinement routine to converge. For example, Kohn anomalies [102] in metals, which can occur in the dispersion

due to electron - phonon interactions and cause kinks in the phonon dispersion, raise a problem. Such anomalies cannot be described within the framework of the Born - von Kármán model [103], since a finite set of force constants can only describe a smooth slope. In order to approximate the dispersions around a Kohn anomaly, many next neighbour interactions have to be considered.

One possibility to reduce the number of force constants is the inclusion of pair potentials. Generally, insulators are easier to treat, since less force constants are needed to describe the system. Finally, even if the large number of fitting parameters does not allow a refinement procedure, one has still the possibility to compare the IXS spectra directly to a theoretical calculation, as has been done in the case of stishovite, thus providing a critical test for the validity of the theoretical approach.

5.2 Stability of the fitting routine

The number of parameters n determines the dimension of the parameter space. Thus, for a large number of force constants, it becomes more difficult to reach the global minimum, and not only a local minimum. Furthermore, the Levenberg - Marquardt algorithm does not always converge for large n to the global minimum, but gets easily trapped in a local minimum. This is a common problem for most minimising strategies. In order to avoid this, the choice of good starting parameters is crucial. It is recommended to compute the inelastic spectra with the starting parameters and to compare the model calculation with the experimental spectra before starting the fitting routine. A good agreement indicates good starting parameters and increases the possibility to find the global minimum. If the initial values are poorly chosen, non-convergence or the convergence into a local minimum is almost unavoidable. We decided to choose the commonly used Levenberg - Marquardt fitting procedure, since it is rapidly converging, thus allowing several initial tests within a reasonable amount of time. Variations in the resulting force constants are mainly due to the fact that the algorithm has the tendency to oscillate close to the minimum [42]. Therefore, a convergence criterion has to be defined, which stops the refinement procedure for small changes $\Delta\chi^2$ in the merit function χ^2 , and thus close to the minimum, whereby the choice $\Delta\chi^2$ depends on the shape of the minimum. In order to circumvent these problems one could use an alternative fitting procedure, such as simulated annealing. These procedure is converging much slower than the Levenberg - Marquardt method and more iterations are needed to reach the minimum.

5.3 High pressure applications

An extension of the proposed refinement method to the study of materials at very high pressures could open new opportunities in various disciplines of material science. As an example we discuss the case of hcp iron, which is of particular interest in the geophysical context.

5.3.1 Experiment: Iron under high pressure

Present theories consider Earth's inner core to be predominantly composed of solid iron in the hcp structure [104], [105], [106]. Since the most powerful tool for the investigation of this part of the Earth are seismic data, the experimental determination of the elastic properties of hcp iron are of great importance. Up to date only polycrystalline hcp - iron could be studied since the 1st order bcc \rightarrow hcp transition at about 13 *GPa* prevents the preservation of the single crystalline state. This complicates the determination of the full elastic tensor. Thus, inconsistencies occur amongst experimental results [27], [107], [108], [109] and calculations using first-principles methods [110], [111]. These discrepancies motivate further experimental efforts, and first tests using the developed IXS refinement procedure are presented below.

For the experiments, an iron foil ($45 \mu\text{m} \times 45 \mu\text{m} \times 25 \mu\text{m}$) was loaded in a $150 \mu\text{m}$ diameter hole drilled into a rhenium gasket, pre-indented to a thickness of $51 \mu\text{m}$ (initially $200 \mu\text{m}$), and pressurised in a diamond anvil cell equipped with diamonds (culet diameter $350 \mu\text{m}$). Helium was used as pressure transmitting medium. Pressure was determined in situ by the ruby fluorescence technique. The sample was kept at 22.5 *GPa*, well above the transition pressure (13 *GPa*), where the phase transition to the hexagonal phase is completed.

Test experiments were performed, utilising the Si (9 9 9) configuration, yielding a total instrumental energy resolution of 3.0 *meV*. The dimensions of the focused x-ray beam were $30 \times 60 \mu\text{m}^2$ (horizontal \times vertical FWHM). Both diamonds of the DAC were oriented with the $\langle 001 \rangle$ direction along the cell axis and the $\langle 110 \rangle$ axis in the scattering plane. In this way the interference of the diamond transverse acoustic phonons with the signal from hcp iron is minimised.

5.3.2 Texture

As shown in the case of graphite, the consideration of texture in the model calculation is relevant, since the intensity distribution in the IXS spectra changes significantly. It is recommended to determine the texture of the sample before the experiment. We therefore investigated the texture of the bcc iron foil, utilising a conventional laboratory x-ray

Further developments

tube. The pole figures for the $\{200\}$, $\{110\}$ and $\{211\}$ reflection and the corresponding stereographic projections are given in Appendix A. The resulting texture consists of two fiber axis components centered around $(\bar{1}12)$ $[110]$ and (001) $[110]$, respectively with an angle of rotation around $[110]$ of about $10^\circ - 15^\circ$ [112]. Thus, the common direction (110) lies in the plane of the foil, and the $(\bar{1}12)$ or (001) directions are roughly perpendicular to the sample surface, slightly tilted with respect to the $[110]$ axis.

Such a textured sample was loaded into the DAC. An angular scan over the (100) , (101) and (002) Bragg peaks was performed. The relative intensities of these three peaks differ from the relative intensities of a perfect powder sample without texture. This reveals texture in the hexagonal phase, though hydrostatic pressure was provided in the cell thanks to the use of He as pressure transmitting medium. Consequently, one can conclude, that the texture of the sample in the hexagonal phase is induced and/or influenced by the texture of the bcc foil. A quantitative analysis of the texture in the ε - phase as was done at ambient conditions could, however, not be performed due to the geometrical constraints of the diamond anvil cell. The above considerations underline the importance to characterise the texture and to include it into the model calculations, whenever texture cannot be avoided.

5.3.3 Scattering Intensity

Figure 5.1 shows four representative IXS spectra of polycrystalline ε -iron at a pressure of 22 GPa . The counting time per point was 9 min ($13 \text{ h } 15 \text{ min}$ for one set of spectra). The statistical error is about 10 %, thus masking the IXS structure in the data for the higher momentum transfer. In order to achieve a reasonable statistical error of about 3 %, one would have to count 10 times longer. In addition, a better resolution is preferable. Utilising the Si $(11\ 11\ 11)$ configuration, with an energy resolution of 1.8 meV , leads to a further reduction of the intensity by a factor 5. At present, one possibility to make the experiment feasible is to increase the number of analysers so that all required IXS spectra are recorded for one setting of the spectrometer. Considering an energy resolution of 3 meV , the counting time would amount to 5.5 days. In the future a higher incident photon flux, provided by a new generation of undulators and an increased storage ring current, will allow a further reduction of the data collection time.

A general consideration of samples in a DAC is related to the sample thickness. This ranges, depending on the pressure, typically between $10 \text{ }\mu\text{m}$ and $40 \text{ }\mu\text{m}$, while the optimal thickness for low Z materials can be as much as 1 mm , or more. Figure 5.2 shows the IXS signal I as a function of the atomic number Z . The sample thickness is $20 \text{ }\mu\text{m}$ and it is reduced for heavier materials ($Z > 65$) to the optimum sample thickness ($L = 1/\mu$). The representation is analogous to Fig 1.4 in chapter 1.1.1. It is apparent that the IXS

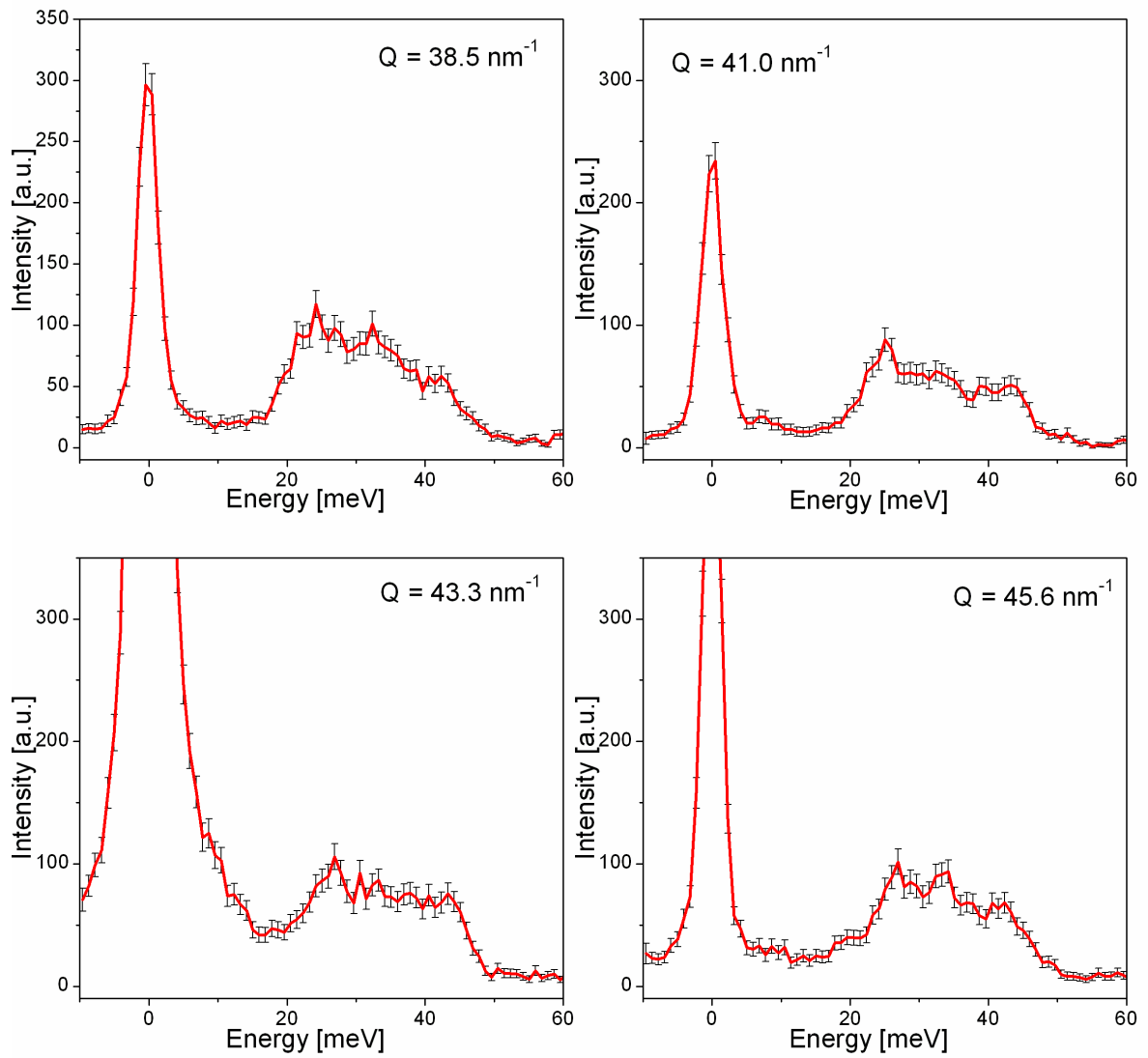


Figure 5.1: IXS spectra of polycrystalline ε - iron at 22 *GPa* for four different momentum transfers. The counting time per point is 540 s.

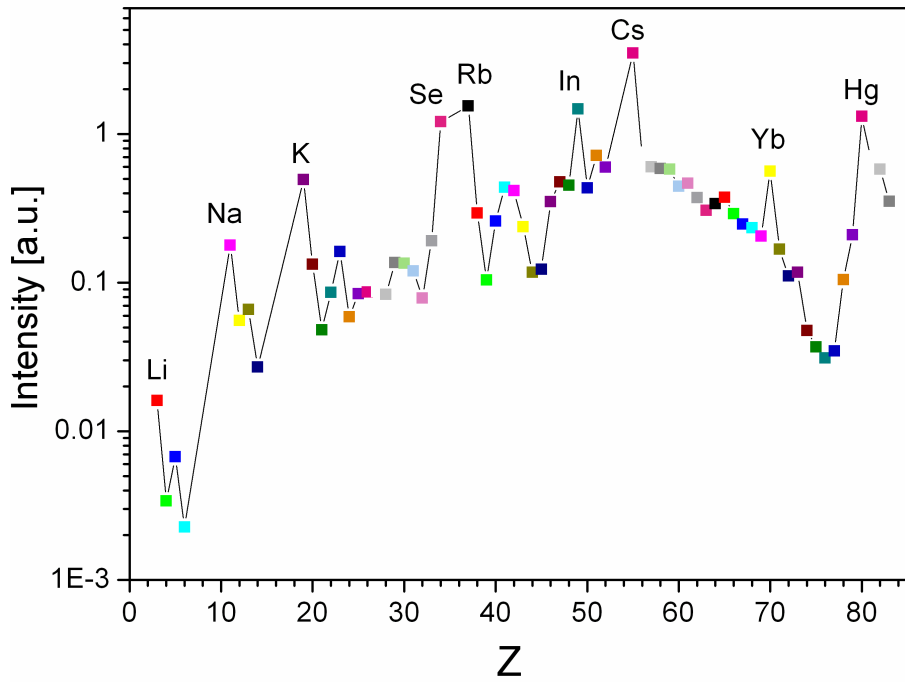


Figure 5.2: IXS signal at 17.794 keV within the small Q - limit ($f(Q) = Z$) for a maximal sample thickness of 20 μm (or optimum thickness for $Z > 65$) as a function of Z .

signal for low - Z materials is low and increases with Z up to $Z = 59$, with a gain of a factor 100 in the scattering intensity in this range. For low Z materials, a compromise between the optimum sample thickness and the thickness, imposed by the high pressure application, has to be made.

Résumé du chapitre 5

Nous résumons dans le chapitre 5 les possibilités ainsi que les limitations actuelles de la méthode de diffusion inélastique des rayons X sur poly-cristaux développée au cours de ce travail, en termes de procédure d'analyse de données aussi bien que de limitations techniques. La complexité du système étudié, qui se traduit en termes de nombres d'atomes dans la maille élémentaire et de nature de l'interaction entre atomes voisins, représente une forte contrainte. De surcroît, la stabilité de la procédure d'ajustement dépend du nombre de constantes de forces à raffiner. Il est important de noter que même si ces limitations ne permettent pas un ajustement parfait, il reste possible de comparer directement les spectres IXS aux calculs théoriques ce qui fournit toujours un critère de validité du modèle utilisé. Dans le cas des mesures à hautes pressions, les difficultés inhérentes aux textures induites par ces pressions et les faibles statistiques sont discutées.

Conclusion

In this thesis work the lattice dynamics of polycrystalline materials were investigated by inelastic x - ray scattering. Methodologies were elaborated with the goal to extract information on the single crystal properties. Three different procedures were presented by means of exemplary cases, namely magnesium oxide, beryllium, graphite and stishovite. First, a method was provided in order to determine the single crystal elastic constants in a polycrystalline cubic system. Furthermore, it was shown that the refinement of a model to the experimental spectra allows the extraction of the single crystal dispersion in simple systems. The consideration of texture is possible, as was demonstrated for the case of pyrolytic graphite. Finally, the possibility to compare theoretical calculations to polycrystalline IXS spectra was presented. This provides on one side a valuable tool for the discrimination of different model calculations. On the other side, it allows one to experimentally evaluate a theoretical model in a time efficient manner compared to measurements on the single crystal system. Concluding, current limitations and further developments are discussed.

The obtained main results can be summarised as follows:

- The elastic constants of the diatomic cubic system MgO were deduced from the bulk modulus, the Debye velocity and the average longitudinal sound velocity. The results agree with literature values within a few percent.
- The experimental phonon density-of-states for beryllium was obtained, for the first time to the best of the author's knowledge. It confirms theoretical predictions. Furthermore the average longitudinal sound velocity was determined.
- The possibility to extract the single crystal dispersion was shown for the cases of beryllium and graphite. The refinement of a model to IXS spectra, spanning a large momentum transfer range resulted in a dispersion relation which is in good agreement with single crystal experimental data. The obtained result was improved by the inclusion of further experimental available quantities, such as bulk modulus and Γ - point frequencies, as additional constraints in the fitting routine. Finally,

Conclusion

the elastic constants were deduced and they are in good agreement with literature values for both cases.

- The effect of texture was successfully included in the refinement procedure for graphite. Moreover, the importance to consider texture effects was demonstrated.
- Different theoretical calculations were confronted to the polycrystalline IXS spectra. For beryllium, two different sets of force constants were published, both obtained from a fit of a Born - von Kármán model to the experimental dispersion. Even though the two calculations match the experimental single crystal dispersion equally well, the computed IXS spectra showed significant differences, thus allowing to identify the better of the two set of force constants. For stishovite a first principle calculation was confronted with the polycrystalline spectra in order to validate the theoretical model.
- Limitations, due to the complexity of the system, texture, scattering intensity and the chosen Born - von Kármán model were explored and further developments were proposed.

It should be emphasised that the interest in single crystal dynamical properties, deduced from the polycrystalline material goes beyond the particular presented cases. This is due to the fact that novel materials and crystals under extreme conditions are often only available in form of polycrystalline samples. Possible further applications are:

- Earth and planetary science: The experimental lattice dynamics study of the Earth's crust and mantle minerals is often limited by the availability of single crystals. Examples are the post - perovskite and perovskite phase of MgSiO_3 or high pressure polymorphs of olivine ($(\text{Mg}, \text{Fe})_2\text{SiO}_4$), Ringwoodite and Wadsleyite. The comparison of the polycrystalline IXS intensity with theoretical calculations opens the possibility to confirm theoretical predictions.
- Superconductors: An example is the temperature dependence of the phonon dispersion for the superconductor MgB_2 , which is an electron - phonon mediated superconductor. Furthermore, the very recently discovered superconductivity in iron based oxypnictides of the type $\text{La}(\text{O}_{1-x}\text{F}_x)\text{FeAs}$, $\text{Nd}(\text{O}_{1-x}\text{F}_x)\text{FeAs}$ etc, should spark interest to study the lattice dynamics. The study of cuprates with the present methodology is limited, due the large number of atoms in the unit cell.
- The study of new materials in the BCNO composition pyramid, which are of potential industrial interest because of their hardness. These materials are synthesised

at high pressure and high temperature and thus often only small crystallites are obtained.

The presented methods and in particular the extraction of the single crystal dispersion, will considerably benefit from the new generation of IXS spectrometers. In a first step, the increase of the number of crystal analysers is of direct advantage. This is in analogy to the trend in inelastic neutron scattering. An N analyser system allows one to collect N IXS spectra simultaneously. This will speed up the collection of the data set over a large momentum transfer range without compromising the Q - resolution. In the ideal case, the experimental data, necessary for the extraction of single crystal information can be collected with only one setting of the spectrometer. Furthermore, future upgrades of the storage ring will provide higher flux, thanks to an increasing current in the storage ring, longer straight sections and cryogenically cooled undulators. The thus higher inelastic signal will as well shorten the experimental time and enable the determination of single crystal properties in cases, which are to date limited by low counting statistics.

Conclusion

Conclusion (française)

Dans ce travail de thèse, nous avons étudié la dynamique de réseau dans les matériaux poly-cristallins par diffusion inélastique des rayons X. Une méthodologie ayant pour but d'extraire des informations sur les propriétés des matériaux monocristallins a été élaborée. Trois procédures distinctes ont été présentées, chacune illustrées par des exemples, à savoir l'oxyde de magnésium, le béryllium le graphite et la stishovite. En premier lieu, nous avons présenté une méthode permettant de déterminer les constantes élastiques d'un monocristal cubique à partir du poly-cristal. Puis, nous avons montré que l'ajustement d'un modèle théorique aux spectres expérimentaux du poly-cristal permettait d'obtenir la dispersion complète des phonons du système monocristallin, dans des cas simples. Nous avons de plus démontré dans le cas du graphite pyrolytique que la prise en considération des effets de texture était possible. Enfin, nous avons vu que la possibilité de confronter des calculs théoriques aux spectres IXS des polycristaux fournissait d'une part un outil performant pour la discrimination de divers modèles, et d'autre part qu'elle permettait d'évaluer expérimentalement un modèle théorique de manière rapide et efficace en comparaison avec les études sur monocristaux. En conclusion, nous avons discuté les limitations actuelles de la méthode ainsi que les développements envisageables.

Nous résumons ci-dessous les principaux résultats que nous avons obtenu au cours de ce travail :

- Les constantes élastiques du système cubique diatomique MgO ont été déduites des mesures du module de compressibilité, de vitesse de Debye et de vitesse du son longitudinale moyenne. Ces résultats sont en accord, à quelques pourcents près, avec les valeurs relevées dans la littérature.
- La densité d'états vibrationnelle du béryllium a été mesurée pour la première fois à notre connaissance, et confirme les prédictions théoriques. Nous avons par ailleurs pu déterminer la valeur de la vitesse du son longitudinale moyenne.
- Nous avons montré qu'il était possible d'extraire la dispersion du monocristal dans les cas du béryllium et du graphite. L'ajustement d'un modèle à nos spectres IXS, couvrant une large gamme de moments transférés nous a permis d'arriver à une

Conclusion (française)

relation de dispersion en bon accord avec celle obtenues sur monocristal. Ces résultats ont encore été améliorés par la prise en compte d'autres quantités telles que le module de compressibilité ou les fréquences des phonons au centre de zone (Γ), et l'inclusion de contraintes supplémentaires dans les routines d'ajustement. Finalement, les constantes élastiques ont été obtenues, en bon accord avec les valeurs de la littérature dans les deux cas.

- Les effets de texture ont été inclus avec succès dans la procédure d'ajustement pour le cas du graphite. Cela nous a par ailleurs démontré l'importance de la prise en compte de ces effets.
- Nous avons confronté divers calculs théoriques aux spectres IXS des poly-cristaux. Dans le cas du béryllium, deux jeux de constantes de forces obtenus par l'ajustement d'un modèle Born - von Kármán à la dispersion expérimentale, sont publiés. Bien que ces deux calculs reproduisent aussi bien la dispersion expérimentale, leur confrontation aux spectres IXS a permis de révéler des différences significatives, grâce auxquelles nous avons pu identifier le jeu de constantes de forces le plus adapté à la description du béryllium. Dans le cas de stishovite, nous avons confronté un calcul *ab initio* aux spectres obtenus sur poly-cristaux afin de valider le modèle.
- Les limitations, dues à la complexité du système étudié, à sa texture, ainsi que l'intensité diffusée et le choix du modèle Born - von Kármán le plus adapté ont été discutés. Des développements ultérieurs de la méthode ont été proposés.

Il est important de souligner que l'intérêt de pouvoir extraire les propriétés dynamiques d'un monocristal à partir de mesures réalisées sur un poly-cristal, ne se limite pas aux quelques cas présentés dans ce manuscrit, et pour cause, les nouveaux matériaux ou les cristaux soumis à des conditions extrêmes ne sont bien souvent disponibles que sous cette forme. Voici à titre d'exemple quelques possibles applications futures de cette méthode :

- Science de la terre et planétologie : l'étude expérimentale de la dynamique de réseau dans les minéraux composant la croûte terrestre ou le manteau est souvent limitée par les faibles quantités de monocristaux disponibles. Par exemple, les phases perovskite et post-perovskite de MgSiO_3 ou les polymorphes à haute pression de l'olivine ($(\text{Mg,Fe})_2\text{SiO}_4$), la Ringwoodite et la Wadsleyite. La confrontation des spectres IXS expérimentaux aux calculs permettrait de confirmer ou d'infirmer un certain nombre de prédictions théoriques.
- Supraconducteurs : par exemple, pour mesurer simplement la dépendance en température de la relation de dispersion des phonons dans MgB_2 , dont la supraconductivité est médiée par l'interaction électron-phonon. De plus, la très récente mise

en évidence de la supraconductivité dans les oxypnictides à base de fer du type $\text{La}(\text{O}_{1-x}\text{F}_x)\text{FeAs}$, $\text{Nd}(\text{O}_{1-x}\text{F}_x)\text{FeAs}$, etc..., devrait susciter un certain intérêt pour les études de dynamique de réseau. En revanche, du fait de leur nombreux atomes par maille élémentaire, l'application de la présente méthode aux cuprates est plutôt limitée.

- L'étude de nouveaux matériaux dans la "pyramide BCNO", qui possèdent un grand potentiel au niveau industriel du fait de leur dureté. Ces matériaux sont synthétisés à hautes température et pression, et seules de très petites cristallites sont en général obtenues.

La méthode présentée et en particulier l'extraction de la dispersion du monocristal va tirer un grand profit de la nouvelle génération de spectromètres IXS. Dans un premier temps, l'augmentation du nombre de cristaux analyseurs est très avantageuse, par analogie avec les tendances observées dans le cas de la diffusion inélastique des neutrons. Un système à N analyseurs permet d'enregistrer N spectres IXS simultanément. Cela augmente la vitesse d'acquisition des données dans une large gamme de moments transférés, sans compromettre la résolution en Q . Idéalement, les données expérimentales nécessaires à l'extraction des informations concernant le monocristal pourraient être collectées à l'aide d'une seule configuration du spectromètre. De plus, les futures améliorations de l'anneau de stockage permettront d'obtenir un plus grand flux de photons incidents, du fait de l'augmentation du courant dans l'anneau, de plus longues sections droites ou d'onduleurs cryo-réfrigérés. L'augmentation du signal inélastique qui en résultera raccourcira significativement les temps de mesures et permettra d'accéder aux propriétés monocristallines de systèmes qu'il n'est actuellement pas possible d'étudier du fait de trop faibles statistiques.

Appendix

Texture measurements for bcc iron

The experimental pole figures for the $\{200\}$, $\{110\}$ and $\{211\}$ reflections, measured on a bcc iron foil, are presented. Furthermore, model pole figures, obtained from the superposition of several stereographic projections are shown. Two stereographic projections for one reflection with two different poles at (001) and $(\bar{1}12)$, were tilted stepwise around the $[110]$ axes. The thus obtained projections, for different poles and different tilt angles, are then superposed and compared to the experimental pole figures. The qualitative agreement demonstrates the validity of the proposed model. It can be suggested, that the direction $[110]$ lies in the plane of the foil, while the either (001) or $(\bar{1}12)$ is perpendicular to the foil surface. Furthermore, the grains are slightly tilted (up to 15°) around the $[110]$ axes. This texture is comparable to the rolling texture in iron, as discussed by Schläfer and Bunge [112]

Appendix: Texture measurements on bcc - iron

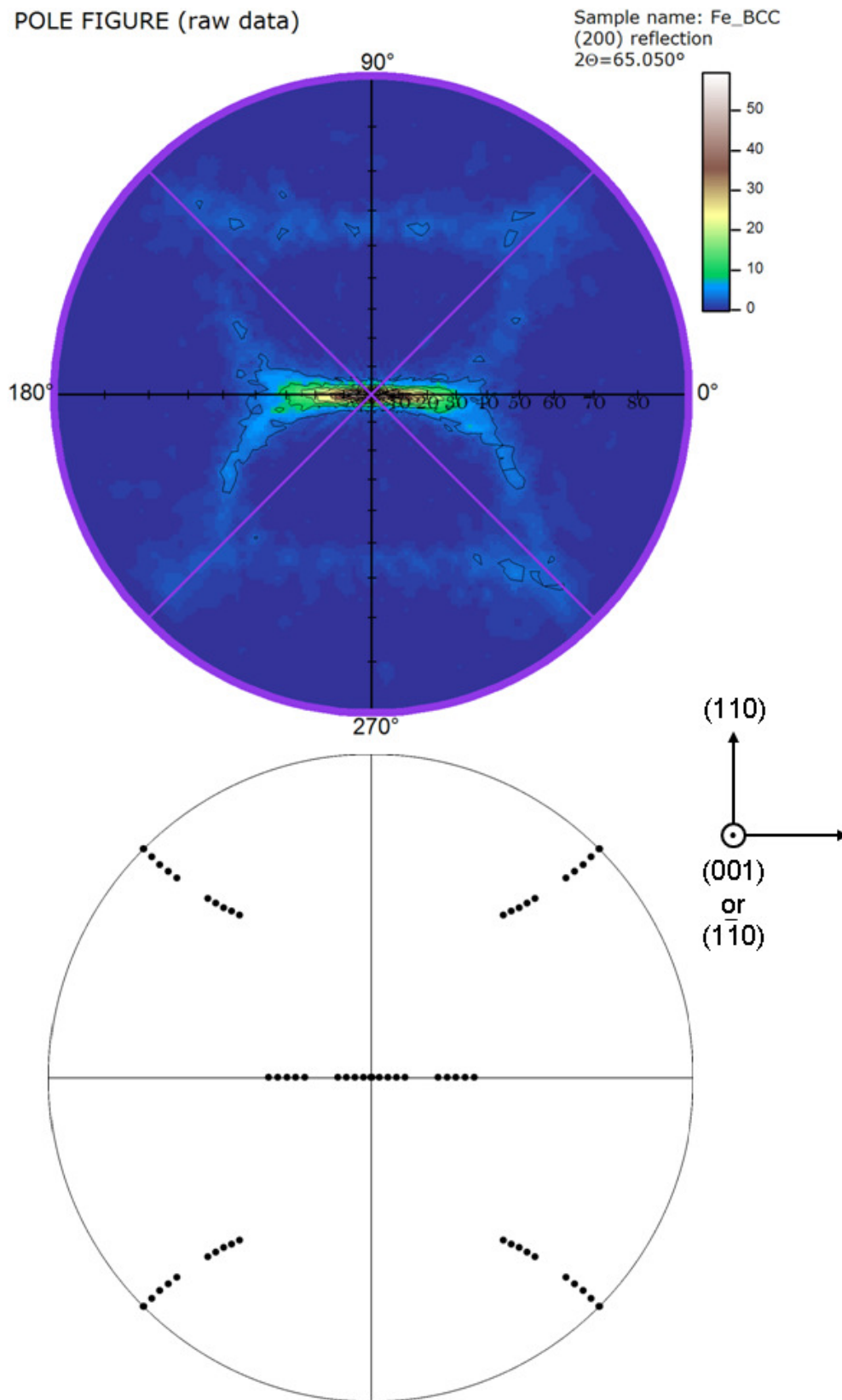


Figure 5.3: Experimental and modeled pole figure for the $\{200\}$ reflection of a bcc iron foil.

POLE FIGURE (raw data)

Sample name: Fe_BCC
(220) reflection
 $2\theta=99.000^\circ$

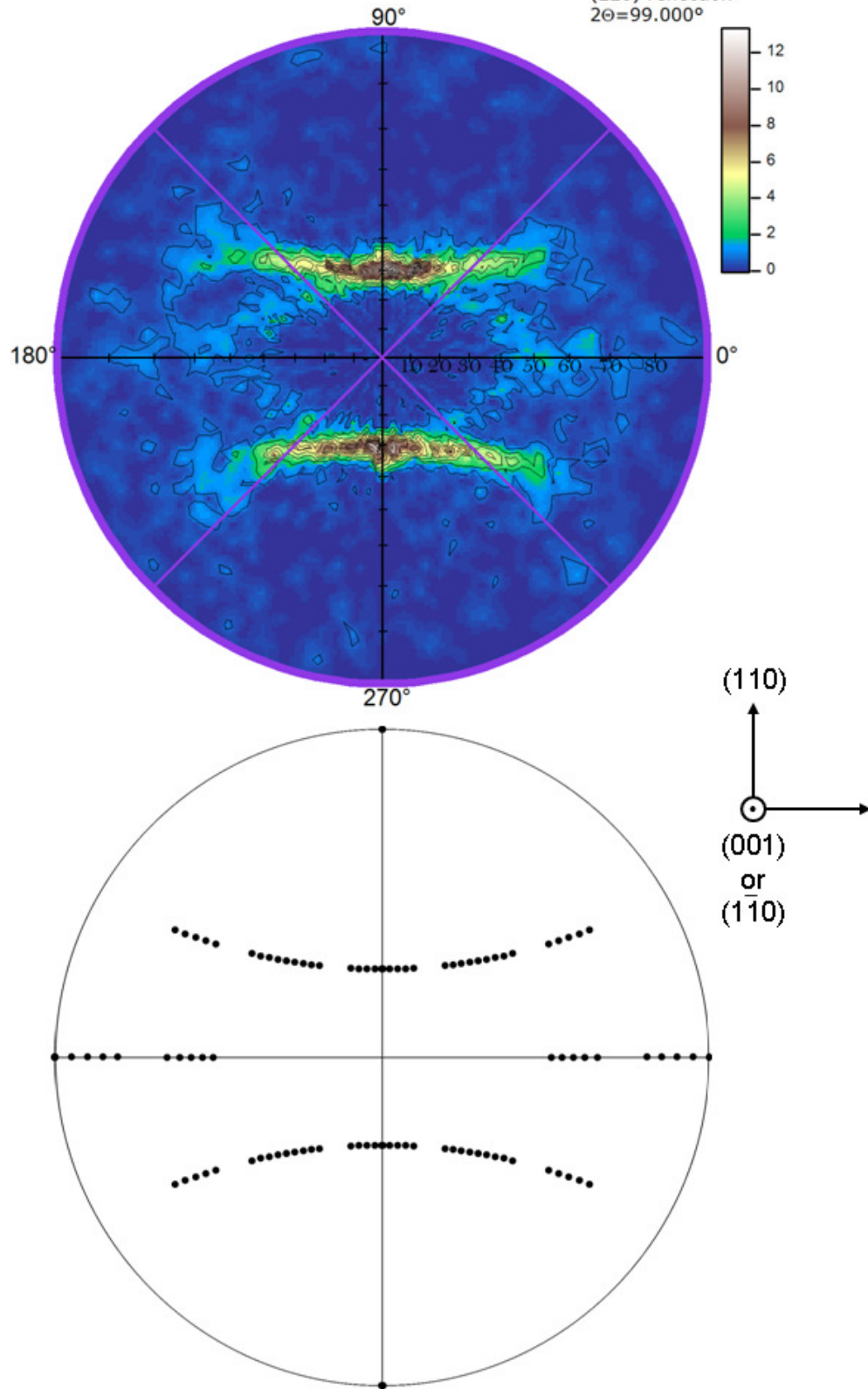


Figure 5.4: Experimental and modeled pole figure for the {110} reflection of a bcc iron foil.

Appendix: Texture measurements on bcc - iron

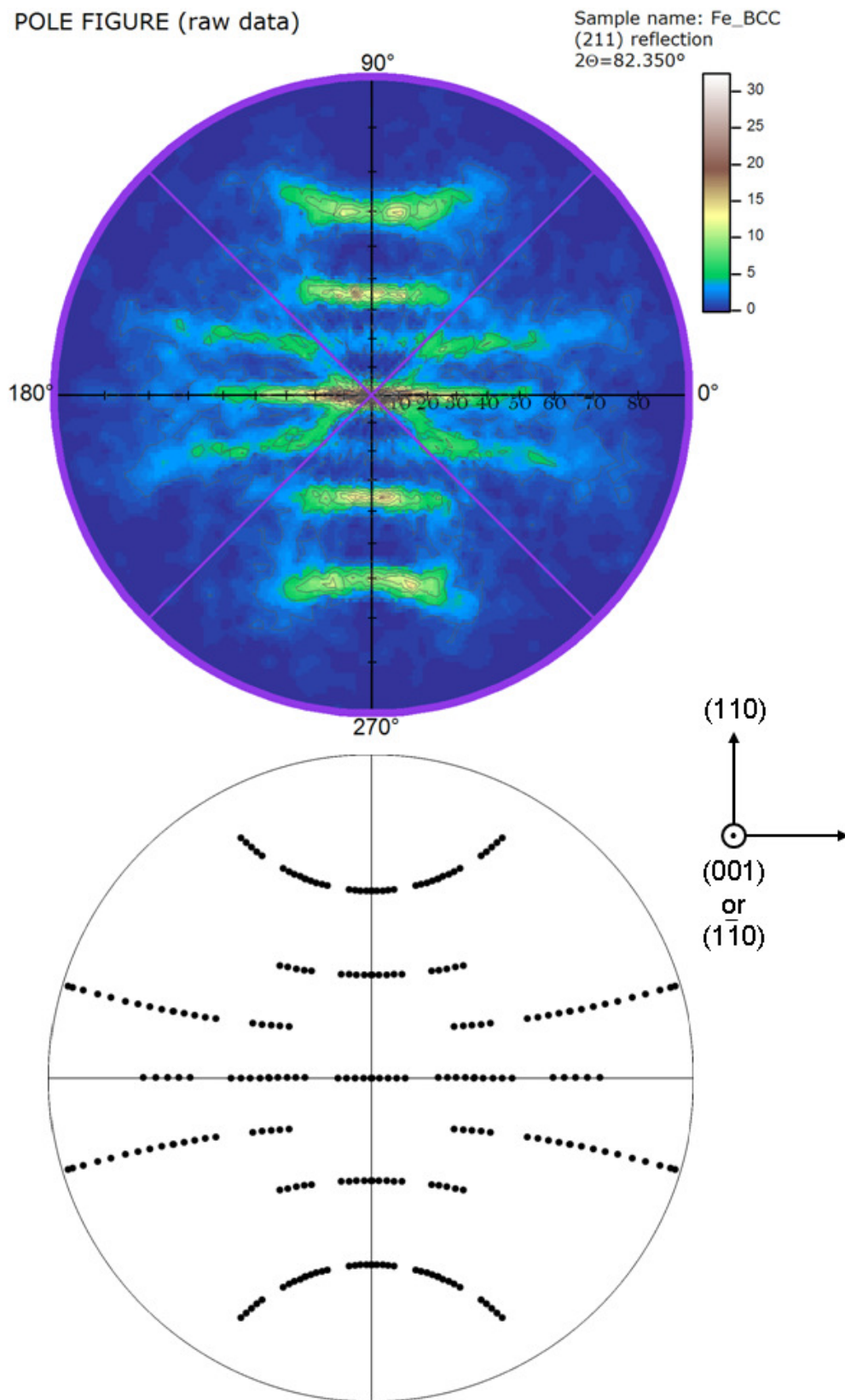


Figure 5.5: Experimental and modeled pole figure for the {211} reflection of a bcc iron foil.

Bibliography

- [1] N. W. Ashcroft and N. D. Mermin,
Solid State Physics,
Brooks/Cole, 1976.
- [2] J. Laval,
Bull. Soc. franc. Minér. **62**, 137 (1939).
- [3] P. Olmer,
Acta Crystallogr. **1**, 57 (1948).
- [4] C. B. Walker,
Phys. Rev. **103**, 547 (1956).
- [5] H. Curien,
Acta. Crystallogr. **5**, 393 (1952).
- [6] E. H. Jacobsen,
Phys. Rev. **97**, 654 (1955).
- [7] H. Egger, W. Hofmann, and J. Kalus,
Appl. Phys. A **35**, 41 (1984).
- [8] B. Dorner, E. Burkel, and J. Peisl,
Nucl. Instrum. & Methods in Phys. Res., Sect. A **246**, 450 (1986).
- [9] B. Dorner, E. Burkel, T. Illini, and J. Peisl,
Z. Phys. B. **69**, 179 (1987).
- [10] E. Burkel,
Inelastic Scattering of X-Rays with Very High Energy Resolution,
Springer-Verlag, Berlin, 1991.
- [11] G. Ruocco and F. Sette,
J. Phys. - Condensed Matter **11**, R259 (1999).
- [12] G. L. Squires,
Introduction to the Theory of Thermal Neutron Scattering,
Cambridge University Press, Cambridge, 1978.

BIBLIOGRAPHY

- [13] A. Bosak and M. Krisch,
Phys. Rev. B **72**, 224305 (2005).
- [14] A. Bosak, M. Krisch, I. Fischer, S. Huotari, and G. Monaco,
Phys. Rev. B **75**, 064106 (2007).
- [15] D. A. Dimitrov, D. Louca, and H. Roder,
Phys. Rev. B **60**, 6204 (1999).
- [16] W. Reichardt and L. Pintschovius,
Phys. Rev. B **63**17, 174302 (2001).
- [17] M. J. Graf, I. K. Jeong, D. L. Starr, and R. H. Heffner,
Phys. Rev. B **68**, 064305 (2003).
- [18] I. K. Jeong, R. H. Heffner, M. J. Graf, and S. J. L. Billinge,
Phys. Rev. B **67**, 104301 (2003).
- [19] A. L. Goodwin, M. G. Tucker, M. T. Dove, and D. A. Keen,
Phys. Rev. Lett. **93**, 075502 (2004).
- [20] S. W. Lovesey,
Theory of Neutron Scattering from Condensed Matter,
Oxford University Press, 1987.
- [21] E. Burkel,
Rep. Prog. Phys. **63**, 171 (2000).
- [22] C. E. Ascheron, M. Cardona, and R. Merlin, editors,
Light scatterin in Solids IX: Novel materials and Techniques,
Springer Verlag, Berlin, 2007.
- [23] M. Blume,
J. Appl. Phys. **57**, 3615 (1985).
- [24] P. Dirac,
The principles of quantum mechanics,
Oxford University Press, Oxford, 1958.
- [25] L. Van Hove,
Phys. Rev. **95**, 249 (1954).
- [26] A. I. Bletzer,
Acoustics of Solids,
Springer-Verlag, Berlin, 1988.
- [27] D. Antonangeli, F. Occelli, H. Requardt, J. Badro, G. Fiquet, and M. Krisch,
Earth Planet.Sci. Lett. **225**, 243 (2004).

- [28] F. W. De Wette and A. Rahman,
Phys. Rev. **176**, 784 (1968).
- [29] V. G. Kohn and A. I. Chumakov,
Hyperfine Interactions **125**, 205 (2000).
- [30] P. Pavone, K. Karch, O. Schutt, W. Windl, D. Strauch, P. Giannozzi, and S. Baroni,
Phys. Rev. B **48**, 3156 (1993).
- [31] W. Voigt,
Lehrbuch der Kristallphysik,
Teubner, Leipzig, 1928.
- [32] A. Reuss,
Z. Angew. Math. Mech. **9**, 49 (1929).
- [33] R. Kaplow, B. L. Averbach, and S. L. Strong,
J. Phys. Chem. Solids **25**, 1195 (1964).
- [34] A. L. Goodwin, M. G. Tucker, E. R. Cope, M. T. Dove, and D. A. Keen,
Physica B **385**, 285 (2006).
- [35] A. L. Goodwin, M. G. Tucker, E. R. Cope, M. T. Dove, and D. A. Keen,
Phys. Rev. B **72**, 214304 (2005).
- [36] G. P. Srivastava,
The Physics of Phonons,
Adam Hilger, 1990.
- [37] M. Born and K. Huang,
Dynamical Theory of Crystal Lattices,
Oxford University Press, Oxford, 1954.
- [38] A. Mirone,
Code source: <http://www.esrf.fr/UsersAndScience/Experiments/TBS/SciSoft>,
2001.
- [39] L. Van Hove,
Phys. Rev. **89**, 1189 (1953).
- [40] K. Levenberg,
The Quarterly of Applied Mathematics **2**, 164 (1944).
- [41] D. W. Marquardt,
Journal of the Society for Industrial and Applied Mathematics **11**, 431 (1963).
- [42] W. H. Press, S. A. Teukolsky, W. T. Vetterling, and B. P. Flannery,

BIBLIOGRAPHY

NUMERICAL RECIPES IN C: THE ART OF SCIENTIFIC COMPUTING Numerical Recipes in C: The art of scientific computing,
Cambridge University Press, 1992.

- [43] R. Verbeni, F. Sette, M. H. Krisch, U. Bergmann, B. Gorges, C. Halcoussis, K. Martel, C. Masciovecchio, J. F. Ribois, G. Ruocco, and H. Sinn,
Journal of Synchrotron Radiation **3**, 62 (1996).
- [44] C. Masciovecchio, U. Bergmann, M. Krisch, G. Ruocco, F. Sette, and R. Verbeni,
Nucl. Instrum. & Methods in Phys. Res. Sec. B **117**, 339 (1996).
- [45] C. Masciovecchio, U. Bergmann, M. Krisch, G. Ruocco, F. Sette, and R. Verbeni,
Nucl. Instrum. & Methods in Phys. Res. Sec. B **111**, 181 (1996).
- [46] A. Bergamin, G. Cavagnero, G. Mana, and G. Zosi,
J. Appl. Phys. **82**, 5396 (1997).
- [47] J. C. Jamieson, A. W. Lawson, and N. D. Nachtrieb,
Rev. Sci. Instrum. **30**, 1016 (1959).
- [48] R. Le Toullec, J. Pinceaux, and P. Loubeyre,
High Press. Res. **1**, 77 (1988).
- [49] G. J. Piermarini, S. Block, J. D. Barnett, and R. A. Forman,
J. Appl. Phys. **46**, 2774 (1975).
- [50] H. K. Mao, J. Xu, and P. M. Bell,
J. Geophys. Res. - Solid Earth and Planets **91**, 4673 (1986).
- [51] F. Datchi, R. LeToullec, and P. Loubeyre,
J. Appl. Phys. **81**, 3333 (1997).
- [52] C. S. Zha, H. K. Mao, and R. J. Hemley,
Proceedings of the National Academy of Sciences of the United States of America
97, 13494 (2000).
- [53] H. K. Mao, P. M. Bell, J. W. Shaner, and D. J. Steinberg,
J. Appl. Phys. **49**, 3276 (1978).
- [54] R. J. Hemley, C. S. Zha, A. P. Jephcoat, H. K. Mao, L. W. Finger, and D. E. Cox,
Phys. Rev. B **39**, 11820 (1989).
- [55] S. Merkel, H. R. Wenk, J. F. Shu, G. Y. Shen, P. Gillet, H. K. Mao, and R. J. Hemley,
J. Geophys. Res. - Solid Earth **107**, 2271 (2002).
- [56] N. D. Drummond and G. J. Ackland,
Phys. Rev. B **65**, 184104 (2002).

-
- [57] T. S. Duffy, R. J. Hemley, and H. K. Mao,
Phys. Rev. Lett. **74**, 1371 (1995).
- [58] S. Ghose, M. Krisch, A. R. Oganov, A. Beraud, A. Bosak, R. Gulve, R. Seelaboyina,
H. Yang, and S. K. Saxena,
Phys. Rev. Lett. **96**, 035507 (2006).
- [59] A. R. Oganov and P. I. Dorogokupets,
Phys. Rev. B **67**, 224110 (2003).
- [60] O. Schutt, P. Pavone, W. Windl, K. Karch, and D. Strauch,
Phys. Rev. B **50**, 3746 (1994).
- [61] S. V. Sinogeikin and J. D. Bass,
Phys. Rev. B **59**, R14141 (1999).
- [62] I. Jackson and H. Niesler,
High Pressure Research in Geophysics,
Center for Academic Publications Japan, Tokio, Japan, 1982.
- [63] M. Y. Chou, P. K. Lam, and M. L. Cohen,
Phys. Rev. B **28**, 4179 (1983).
- [64] Y. W. Yang and P. Coppens,
Acta Crystallogr. Sec. A **34**, 61 (1978).
- [65] R. Stedman, Z. Amilius, R. Pauli, and O. Sundin,
J. Phys. F **6**, 157 (1976).
- [66] A. Migliori, H. Ledbetter, D. J. Thoma, and T. W. Darling,
J. Appl. Phys. **95**, 2436 (2004).
- [67] M. Lazzeri and S. de Gironcoli,
Surf. Sci. **404**, 715 (1998).
- [68] G. Robert and A. Sollier,
Journal de Physique IV **134**, 257 (2006).
- [69] D. F. Mc Morrow, R. A. Cowley, R. M. Nicklow, P. W. Mitchell, A. D. Taylor, and
M. Mostoller,
J. Phys. - Condensd Matter **2**, 1045 (1990).
- [70] G. V. Sin'ko and N. A. Smirnov,
Phys. Rev. B **71**, 214108 (2005).
- [71] C. A. Swenson,
J. Appl. Phys. **70**, 3046 (1991).

BIBLIOGRAPHY

- [72] J. B. Hannon, E. J. Mele, and E. W. Plummer,
Phys. Rev. B **53**, 2090 (1996).
- [73] W. D. Rowland and J. S. White,
J. Phys. F **2**, 231 (1972).
- [74] J. F. Smith and C. L. Arbogast,
J. Appl. Phys. **31**, 99 (1960).
- [75] S. Merkel, A. F. Goncharov, H. K. Mao, P. Gillet, and R. J. Hemley,
Science **288**, 1626 (2000).
- [76] F. Kwasniok,
Surf. Sci. **329**, 90 (1995).
- [77] K. S. Novoselov, A. K. Geim, S. V. Morozov, D. Jiang, Y. Zhang, S. V. Dubonos,
I. V. Grigorieva, and A. A. Firsov,
Science **306**, 666 (2004).
- [78] L. Wirtz and A. Rubio,
Solid State Commun. **131**, 141 (2004).
- [79] R. Nicklow, H. G. Smith, and N. Wakabayashi,
Phys. Rev. B **5**, 4951 (1972).
- [80] C. Oshima, T. Aizawa, R. Souda, Y. Ishizawa, and Y. Sumiyoshi,
Solid State Commun. **65**, 1601 (1988).
- [81] S. Siebentritt, R. Pues, K. H. Rieder, and A. M. Shikin,
Phys. Rev. B **55**, 7927 (1997).
- [82] H. Yanagisawa, T. Tanaka, Y. Ishida, M. Matsue, E. Rokuta, S. Otani, and C. Oshima,
Surface and Interface Analysis **37**, 133 (2005).
- [83] J. Maultzsch, S. Reich, C. Thomsen, H. Requardt, and P. Ordejón,
Phys. Rev. Lett. **92**, 075501 (2004).
- [84] M. Mohr, J. Maultzsch, E. Dobardžić, S. Reich, I. Milošević, M. Damnjanović,
A. Bosak, M. Krisch, and C. Thomsen,
Phys. Rev. B **76**, 035439 (2007).
- [85] A. Bosak, M. Krisch, M. Mohr, J. Maultzsch, and C. Thomsen,
Phys. Rev. B **75**, 153408 (2007).
- [86] S. Matthies and M. Humbert,
J. Appl. Crystallogr. **28**, 254 (1995).

- [87] T. Tohei, A. Kuwabara, F. Oba, and I. Tanaka,
Phys. Rev. B **73**, 064304 (2006).
- [88] N. Mounet and N. Marzari,
Phys. Ref. B **71**, 205214 (2005).
- [89] M. Hasegawa and K. Nishidate,
Phys. Rev. B **70**, 205431 (2004).
- [90] J. C. Boettger,
Phys. Rev. B **55**, 11202 (1997).
- [91] S. M. Stishov and S. V. Popova,
Geokhimiya **10**, 837 (1961).
- [92] E. C. T. Chao, J. J. Fahey, J. Littler, and D. J. Milton,
J. Geophys. Res. **67**, 419 (1962).
- [93] K. Hirose, N. Takafuji, N. Sata, and Y. Ohishi,
Earth Planet. Sci. Lett. **237**, 239 (2005).
- [94] A. E. Ringwood,
Composition and Petrology of the Earth's Mantle,
McGraw-Hill, 1975.
- [95] N. A. Dubrovinskaia and L. S. Dubrovinsky,
Materials Chemistry and Physics **68**, 77 (2001).
- [96] R. J. Hill, M. D. Newton, and G. V. Gibbs,
J. Solid State Chem. **47**, 185 (1983).
- [97] N. R. Keskar and J. R. Chelikowsky,
Phys. Chem Minerals **22**, 233 (1995).
- [98] T. Tsuchiya, R. Caracas, and J. Tsuchiya,
Geophys. Res. Lett. **31**, L11610 (2004).
- [99] C. Y. LEE and X. GONZE,
PHYSICAL REVIEW LETTERS **72**, 1686 (1994).
- [100] M. F. Vidasina, E. V. Guseva, and R. Y. Orlov,
Fizika Tverdogo Tela **31**, 47 (1989).
- [101] A. M. HOFMEISTER, J. XU, and S. AKIMOTO,
AMERICAN MINERALOGIST **75**, 951 (1990).
- [102] W. Kohn,
Phys. Rev. Lett. **2**, 393 (1959).

BIBLIOGRAPHY

- [103] S. Piscanec, M. Lazzeri, F. Mauri, A. C. Ferrari, and J. Robertson,
Phys. Rev. Lett. **93**, 185503 (2004).
- [104] F. Birch,
J. Geophys. Res. **57**, 227 (1952).
- [105] A. Jephcoat and P. Olson,
Nature **325**, 332 (1987).
- [106] H. K. Mao, Y. Wu, L. C. Chen, J. F. Shu, and A. P. Jephcoat,
J. Geophys. Res. - Solid Earth and Planets **95**, 21737 (1990).
- [107] H. K. Mao, J. F. Shu, G. Y. Shen, R. J. Hemley, B. S. Li, and A. K. Singh,
Nature **396**, 741 (1998).
- [108] H. K. Mao, J. F. Shu, G. Y. Shen, R. J. Hemley, B. S. Li, and A. K. Singh,
Nature **399**, 280 (1999).
- [109] H. K. Mao, J. Xu, V. V. Struzhkin, J. Shu, R. J. Hemley, W. Sturhahn, M. Y. Hu,
E. E. Alp, L. Vocadlo, D. Alfe, G. D. Price, M. J. Gillan, M. Schwoerer-Bohning,
D. Hausermann, P. Eng, G. Shen, H. Giefers, R. Lubbers, and G. Wortmann,
Science **292**, 914 (2001).
- [110] G. Steinle-Neumann, L. Stixrude, R. E. Cohen, and O. Gulseren,
Nature **413**, 57 (2001).
- [111] A. Laio, S. Bernard, G. L. Chiarotti, S. Scandolo, and E. Tosatti,
Science **287**, 1027 (2000).
- [112] D. Schläfer and H. J. Bunge,
Texture **1**, 157 (1974).

Acknowledgements

It's a pleasure to thank the many people who made this thesis possible.

This thesis could not have been written without the help of Michael Krisch who not only guided this work as my supervisor but also supported and encouraged me with his enthusiasm and inspiration. Thank you for always having an open door and open ear for me.

Furthermore, I am grateful to Alexei Bosak, my second supervisor, whose wide knowledge and logical way of thinking have been of great value for me. His understanding and detailed and constructive comments have provided a good basis for the present thesis.

During this work I was surrounded by the ID28 team (Alexandre, Filippo, Jorge, Mathieu, Moritz) which are not only fantastic colleagues but also good friends. I enjoyed a lot working with you and appreciated our social events. My thanks as well to Denis Gambetti, who supported me by all technical questions.

This thesis would not have been possible unless the support by Alessandro Mirone. Thank you for teaching and discussing with me Python and OPENPHONON and all problems I had with these two programs. The parallelisation of the program code was possible through the help of Rainer Wilcke.

A big thank you to Ulrich Ponkratz, who shared with me his knowledge about high pressure physics. Furthermore, I am very grateful to staff of the high pressure lab, especially to Jeroen Jacobs, for their help by the preparation of the high pressure cells. A sincere thanks as well to Michael Hanfland for the gas loading of the samples.

I am very grateful to the members of my PhD jury, Mr. Regnard, Mr. Benedek, Mr. Currat, Mr. Loa, Mr. Keen, for the time they spent to read my thesis and their helpful critical comments.

During all the three years I shared my office with Andrea, Filippo, Roberto, Thomas and Bea, which are (or were) as well PhD students. Thank you for your help and discussions in various subjects like health insurance, holidays, inscription to the university, which is the best English word, which colour should I use for my poster and so on...

My warm thanks go to all my friends here in Grenoble. I will miss all the hiking, climbing, biking tours, the coffee breaks, the beers and wines, the cooking evenings ...

Acknowledgements

A big thank you as well to my friends in Germany, which from childhood on joined my live and shared with me good and hard times. My special thanks goes to Alex for his presents and his invaluable support

I cannot finish without saying how grateful I am with my family for their love and unflagging support throughout my life. Specially I wish to thanks my parents. They have always encouraged me to do my best in all matters of life. This thesis is simply impossible without them.